
Enhancement cavities for the generation of extreme ultraviolet and hard x-ray radiation

Henning Carstens



München 2016

Enhancement cavities for the generation of extreme ultraviolet and hard x-ray radiation

Henning Carstens

Dissertation
an der Fakultät für Physik
der Ludwig–Maximilians–Universität
München

vorgelegt von
Henning Carstens
aus Buxtehude

München, den 30.05.2016

Erstgutachter: Prof. Dr. Ferenc Krausz

Zweitgutachter: Prof. Dr. Harald Weinfurter

Tag der mündlichen Prüfung: 15.12.2016

Zusammenfassung

Es gibt keine gut funktionierenden Laser, welche im extrem ultravioletten oder im Röntgenbereich arbeiten. Hier ist die einzige Möglichkeit zur Erzeugung kohärenter Strahlung im Labormaßstab daher die Frequenzkonversion von Lasern aus anderen Spektralbereichen. Diese ist allerdings im Allgemeinen sehr ineffizient, sodass es sich anbietet, die nicht konvertierte Laserleistung in einem *Überhöhungsresonator* wiederzuverwerten.

In dieser Arbeit geht es um die Skalierung der verfügbaren Durchschnittsleistung und Intensität in Überhöhungsresonatoren mit ultrakurzen Laserpulsen. Hierbei werden Pulse eines modengekoppelten Lasers in einen externen optischen Resonator eingekoppelt, was die Überhöhung der Pulsenergie um einige Größenordnungen erlaubt. Die Hauptanwendungen sind zum einen die Erzeugung hoher Harmonischer von Laserlicht aus dem nahen Infrarot in den extrem ultravioletten Spektralbereich, und zum anderen die Erzeugung harter Röntgenstrahlung durch inverse Comptonstreuung (auch bekannt als Thomsonstreuung).

Für beide Anwendungen werden Intensitäten im Bereich $10^{13} - 10^{15} \text{ W/cm}^2$ bei vielen Kilowatt Durchschnittsleistung benötigt. Die Schwierigkeit bei der Umsetzung besteht darin, eine Zerstörung der Spiegel aus denen der Resonator besteht zu vermeiden. Dazu muss der zirkulierende Strahl eine möglichst große Fläche auf allen Optiken aufweisen. In der Arbeit werden hierfür Designkriterien entwickelt und deren Umsetzung, insbesondere in Bezug auf die Justageempfindlichkeit, untersucht und demonstriert.

Weiterhin ist eine Optimierung der thermischen Eigenschaften des Resonators zur Erreichung der Ziele unabdingbar. Diese wird hier sowohl durch die Wahl der Resonatorgeometrie, als auch durch eine Verbesserung der Spiegel in Bezug auf Absorption und thermischer Verformung, erreicht. Das erlaubte eine zirkulierende Leistung von mehreren hundert Kilowatt mit ultrakurzen Pulsen. Diese Leistungsparameter sind insbesondere für inverse Comptonstreuung interessant.

Diese Erkenntnisse wurden dann verwendet, um 30 fs Pulse auf mehr als 10 kW Durchschnittsleistung zu überhöhen. Hiermit wurden hohe Harmonische mit über 100 eV Photonenergie bei einer Repetitionsrate von 250 MHz erzeugt, wobei der Photonenfluss erstmals ausreichend ist für Experimente zur Untersuchung von Dynamiken auf Oberflächen mittels Photoelektronenemissionsmikroskopie.

Abstract

There are no lasers operating in the extreme ultraviolet or x-ray spectral region. Here, the only possibility to obtain coherent radiation in a laboratory scale is frequency conversion from lasers operating at other wavelengths. These processes are in general very inefficient. Thus, it is advantageous to recycle the non-converted light in an *enhancement cavity*.

This thesis is about the scaling of average power and intensity in ultrashort pulse enhancement cavities. Here, pulses from a modelocked laser are continuously coupled into an external optical resonator, allowing for a pulse energy enhancement of orders of magnitude. The main applications are on the one hand the generation of high harmonics of the near infrared light into the extreme ultraviolet spectral region, and on the other hand the generation of hard x-ray radiation via inverse Compton scattering (also known as Thomson scattering).

For both applications intensities ranging from $10^{13} - 10^{15} \text{ W/cm}^2$ with several kilowatt of average power are required. In this regime, avoiding damage of the cavity mirrors is difficult. To this end, the circulating beam must have a large cross section on all cavity optics. In this work, design criteria aiming at this are developed and its implementation, in particular regarding the misalignment sensitivity, is investigated and demonstrated.

Furthermore, the optimization of the resonator's thermal properties is necessary for fulfilling the target parameters. Here, this is achieved both by proper choice of the cavity geometry, and by custom mirrors with reduced absorption and improved thermal deformation. This allowed for average powers of several 100s of kilowatts with ultrashort pulses. This power regime is in particular interesting for inverse Compton scattering.

These findings were used for the enhancement of 30-fs pulses to 10 kW of average power. This allowed for the generation of high harmonics with photon energies exceeding 100 eV at 250 MHz repetition rate. In this experiment, for the first time the photon flux was sufficient for experiments aiming at the study of dynamics on surfaces using photo electron emission microscopy (PEEM).

Danksagung

Diese Arbeit war nur durch die Unterstützung vieler Menschen möglich, denen ich hiermit danken möchte.

Zuallererst möchte ich Ferenc danken, dass er die Arbeit betreut hat und ich in der Gruppe arbeiten konnte. Ich habe durch das tolle Umfeld viel gelernt! Außerdem möchte ich meinem direkten Betreuer Ioachim herzlich danken. Im Rahmen der Doktorarbeit ist ein tolles Team rund um die Cavities entstanden, was wesentlich Dir zuzuschreiben ist. Danke für die Unterstützung, von der Laborarbeit bis zum Verbessern meiner Schreibkunst!

Als ich angefangen habe, bestand das Team neben Ioachim nur aus Simon und Herrn Fill, der inzwischen ins Mid-IR Team gewechselt ist. Kurz darauf stieß Niko zu uns, zunächst als HiWi, dann als Masterand und inzwischen als Doktorand. Vielen Dank für die tolle Zeit! Inzwischen ist das Team um Tobi, Maxi, Christina und Stephan gewachsen. Auch euch danke ich! Hoffentlich bringt ihr die Arbeit weiterhin erfolgreich voran.

Weiterhin danke Jens Limpert und seinen Leuten, insbesondere Tino und Christoph, für den Laser und den Premium-Service hierfür!

Auch im Cavity-Meeting habe ich viele gelernt. Dafür möchte ich insbesondere den Thomas, Andi, Dylan, Tobi, Johannes und Akira danken!

Ich habe daneben durch tolle Kooperationen profitiert. Dafür danke ich Vova und Alex Guggenmos für Spiegel, Dominik Esser für das Durchbohren der Spiegel.

Außerdem möchte ich mich bei allen aktuellen Kollegen an der LMU und denen, die den Coulombwall bereits durchtunnelt haben, bedanken: Oleg, Markus, Jonathan, Michael, Elena, Florian, Olga, Kellie, Dominik, Peter, Daniel, Stefan, Friedrich, Catherine, Nora, Ivan, Waldemar und allen, die ich vergessen habe.

Zu guter Letzt möchte ich mich bei meinen Eltern für die Unterstützung danken, ohne die ich natürlich nie hierher gekommen würde. Danke!

List of publications

Main publications on the topics of this thesis

H. Carstens, M. Högner, T. Saule, S. Holzberger, N. Lilienfein, A. Guggenmos, C. Jocher, T. Eidam, D. Esser, V. Tosa, V. Pervak, J. Limpert, A. Tünnermann, U. Kleineberg, F. Krausz, and I. Pupeza "High-harmonic generation at 250 MHz with photon energies exceeding 100 eV" *Optica* **3**, 366-369 (2016)

H. Carstens, N. Lilienfein, S. Holzberger, C. Jocher, T. Eidam, J. Limpert, A. Tünnermann, J. Weitenberg, D. C. Yost, A. Alghamdi, Z. Alahmed, A. Azzeer, A. Apolonski, E. Fill, F. Krausz, and I. Pupeza, "Megawatt-scale average-power ultrashort pulses in an enhancement cavity," *Opt. Lett.* **39**, 2595-2598 (2014)

H. Carstens, S. Holzberger, J. Kaster, J. Weitenberg, V. Pervak, A. Apolonski, E. Fill, F. Krausz, and I. Pupeza, "Large-mode enhancement cavities," *Opt. Express* **21**, 11606-11617 (2013)

Other publications

S. Holzberger, N. Lilienfein, **H. Carstens**, T. Saule, M. Högner, F. Lücking, M. Trubetskov, V. Pervak, T. Eidam, J. Limpert, A. Tünnermann, E. Fill, F. Krausz, and I. Pupeza, "Femtosecond enhancement cavities in the nonlinear regime." *Phys. Rev. Lett.* **115.2** (2015)

S. Holzberger, N. Lilienfein, M. Trubetskov, **H. Carstens**, F. Lücking, V. Pervak, F. Krausz, and I. Pupeza, "Enhancement cavities for zero-offset-frequency pulse trains," *Opt. Lett.* **40**, 2165-2168 (2015)

N. Lilienfein, **H. Carstens**, S. Holzberger, C. Jocher, T. Eidam, J. Limpert, A. Tünnermann, A. Apolonski, F. Krausz, and I. Pupeza, "Balancing of thermal lenses in enhancement cavities with transmissive elements," *Opt. Lett.* **40**, 843-846 (2015)

S. Breitkopf, T. Eidam, A. Klenke, L. von Grafenstein, **H. Carstens**, S. Holzberger, E. Fill, T. Schreiber, F. Krausz, A. Tünnermann, I. Pupeza, and J. Limpert, "A concept for multiterawatt fibre lasers based on coherent pulse stacking in passive cavities." *Nature: Light Sci. Appl.* **3.10** (2014)

I. Pupeza, S. Holzberger, T. Eidam, **H. Carstens**, D. Esser, J. Weitenberg, P. Rußbüldt, J. Rauschenberger, J. Limpert, Th. Udem, A. Tünnermann, T. W. Hänsch, A. Apolonski, F. Krausz, and E. Fill, „Compact high-repetition-rate source of coherent 100 eV radiation,“ *Nature Photon.* **7**, 608–612 (2013)

S. Hädrich, **H. Carstens**, J. Rothhardt, J. Limpert, and A. Tünnermann, "Multi-gigawatt ultrashort pulses at high repetition rate and average power from two-stage nonlinear compression," *Opt. Express* **19**, 7546-7552 (2011)

S. Hädrich, M. Krebs, J. Rothhardt, **H. Carstens**, S. Demmler, J. Limpert, and A. Tünnermann, "Generation of μW level plateau harmonics at high repetition rate," *Opt. Express* **19**, 19374-19383 (2011)

J. Rothhardt, S. Hädrich, **H. Carstens**, N. Herrick, S. Demmler, J. Limpert, and A. Tünnermann, "1 MHz repetition rate hollow fiber pulse compression to sub-100-fs duration at 100 W average power," *Opt. Lett.* **36**, 4605-4607 (2011)

T. Eidam, J. Rothhardt, F. Stutzki, F. Jansen, S. Hädrich, **H. Carstens**, C. Jauregui, J. Limpert, and A. Tünnermann, "Fiber chirped-pulse amplification system emitting 3.8 GW peak power," *Opt. Express* **19**, 255-260 (2011)

T. Eidam, S. Hädrich, F. Jansen, F. Stutzki, J. Rothhardt, **H. Carstens**, C. Jauregui, J. Limpert, and A. Tünnermann, "Preferential gain photonic-crystal fiber for mode stabilization at high average powers," *Opt. Express* **19**, 8656-8661 (2011)

Contents

1	Introduction	1
1.1	The impact of the laser	1
1.2	Sources of coherent extreme-ultraviolet and hard x-ray radiation	2
1.2.1	High-harmonic generation	2
1.2.2	Inverse-Compton scattering	3
1.3	Research Objectives	4
2	Theoretical background	5
2.1	Laser beams in the paraxial approximation	5
2.1.1	Fundamental Gaussian beam	5
2.1.2	Orthonormal Gauss-Hermite basis	6
2.1.3	Orthonormal Gauss-Laguerre basis	7
2.1.4	Propagation of Gaussian beams: The ABCD law	7
2.2	Stable optical resonators	8
2.2.1	Stability criteria	8
2.2.2	Resonators with misaligned elements	9
2.2.3	Imaging resonators	10
2.2.4	Transverse mode spectrum	10
2.3	Enhancement cavities	11
2.3.1	Energy relations in enhancement cavities	11
2.3.2	Perturbations	12
2.3.3	Impedance-matched and input-coupler-limited enhancement . .	13
2.3.4	Frequency combs and ultrashort pulse enhancement cavities . .	14
2.4	Thermal effects in laser optics	15
2.4.1	Heat equation and elastic deformation	15
2.4.2	Thermal lenses: Focusing and aberrations	16
2.4.3	Winkler's formula	17
2.5	High-order harmonic generation	18
2.5.1	Microscopic picture	18
2.5.2	Phase matching	19
2.5.3	High-harmonic generation in absorbing media	20
3	Design of high-power enhancement cavities	23
3.1	Design considerations	23

3.2	Cavity designs	25
3.2.1	Standard bow-tie cavity	25
3.2.2	All-curved-mirror cavity	26
3.2.3	Further designs	27
3.3	Application-specific requirements	27
3.3.1	High-harmonic generation	27
3.3.2	Thomson scattering	29
3.3.3	Stack-and-dump	30
3.4	Misalignment sensitivity	31
3.4.1	Introduction	31
3.4.2	Comparison of cavity designs	34
3.4.3	Experimental verification	35
3.5	Astigmatic compensation	38
3.5.1	In-plane compensation	38
3.5.2	Non-planar cavities	39
3.6	Conclusions	40
4	Megawatt-level average power enhancement cavities for ultrashort pulses	43
4.1	Introduction	43
4.2	Quantitative model for the thermal sensitivity	44
4.2.1	Calculation of the steady state	44
4.2.2	Thermal sensitivity	45
4.3	Power scaling with custom optics	47
4.3.1	Substrate materials	47
4.3.2	Coating absorption	49
4.4	Experimental apparatus	50
4.5	Experimental results	52
4.6	Limitations for the achievable intensity and average power	54
4.6.1	Spherical aberrations	54
4.6.2	Thermal aberrations	55
4.6.3	Transient thermal lensing	57
4.7	Conclusions	60
5	High-harmonic generation at 250 MHz repetition rate	61
5.1	High-harmonic generation in enhancement cavities	61
5.1.1	Motivation	61
5.1.2	Intensity clamping	63
5.1.3	Cumulative plasma	63
5.1.4	Conversion efficiency	64
5.1.5	Limitations of the on-axis model	66

5.2	Experimental apparatus	67
5.2.1	Laser system and enhancement cavity	67
5.2.2	XUV output coupling	69
5.2.3	XUV diagnostics	72
5.3	Experimental results	73
5.4	Conclusions	77
6	Summary & Outlook	79
6.1	Power scaling of enhancement cavities for inverse-Compton scattering .	79
6.2	Cavity-enhanced high-harmonic generation	80
	Bibliography	83
	Appendix: Data archiving	97

CHAPTER 1

Introduction

1.1 The impact of the laser

Theodore Maiman allegedly said about his invention, the laser, that it is a "solution looking for a problem" [1]. Since its first demonstration in 1960, countless applications for lasers have been found in diverse fields of science and technology. Due to its outstanding properties, namely coherence, diffraction limited focusability, high brightness, and either high spectral purity or broadband pulsed operation, the laser has become an indispensable tool for imaging and spectroscopy. For example, with coherent illumination, transparent objects can be observed using phase contrast microscopy [2], and using laser scanning confocal microscopy (LSCM) the image quality of biological objects can be greatly enhanced [3]. While the foundations of confocal microscopy have been laid already in the 1950s, it became a standard technique only after the availability of high brightness laser sources [4]. In spectroscopy, the relative accuracy of atomic hydrogen measurements was improved using laser spectroscopy from 10^{-7} to 10^{-10} [5]. Later, using the so-called laser frequency comb spectroscopy, it was further improved to 10^{-14} [5]. Here, the optical spectrum of the laser consists of many equidistant comb modes and can be described with two microwave frequencies f_0 and f_{rep} , $f_n = f_0 + n \cdot f_{\text{rep}}$ [6]. Thus, optical frequencies can be mapped to the frequency standard defined by cesium atomic clocks in one step, instead of complicated chains of frequency dividers, greatly

reducing noise. Nowadays, optical frequency combs covering the visible, near infrared and mid-infrared range based on rare-earth doped lasers are commercially available.

1.2 Sources of coherent extreme-ultraviolet and hard x-ray radiation

Both spectroscopy and imaging would tremendously benefit from coherent, high brightness sources in the ultraviolet and x-ray spectral region. This would allow for the extension of the above mentioned methodology to smaller objects in imaging [7–9], for spectroscopy of transitions with higher photon energies [10], and even for the generation and use of attosecond pulses [11]. However, the widespread use of coherent light from lasers in this spectral region is hindered by the lack of active media and because it becomes more and more difficult to obtain a population inversion in an active medium at high photon energies. This is because the ratio of the rate of stimulated emission to that of spontaneous emission is proportional to λ^3 [12], i.e. for short wavelength spontaneous emission dominates and laser amplification becomes impossible. Alternatively, one can build lasers in the visible or near-infrared and transfer their radiation to the desired spectral range with nonlinear or scattering processes. In recent years, ytterbium-doped lasers have undergone a dramatic increase in available power with ultrashort pulses enabled by high-power pump diodes. Laser geometries optimized for an efficient heat transfer (fibres [13], thin-disk [14], and innoslab [15]) yielded powers on the kilowatt level with (sub-) picosecond pulses at about 1 μm wavelength rendering ytterbium-based lasers a suitable technology for driving these frequency conversion processes.

1.2.1 High-harmonic generation

One possibility to convert these lasers to the extreme ultraviolet (XUV) or even soft x-ray region is high-harmonic generation (HHG) in noble gases [16]. In contrast to low harmonic orders (up to 10), the conversion efficiency for higher orders does not drop [17, 18], but stays constant over a broad range of harmonic orders, called plateau. Photon energies up to the keV-level [19, 20] and pulse durations of less than 100 as [11, 21, 22] have been demonstrated with this technique. Nowadays HHG is routinely used at kHz repetition rates [23], but both time-domain and frequency-comb spectroscopy demand for higher repetition. In the case of frequency combs, the power per comb line is proportional to the repetition rate, implying that repetition rates as high as possible (e.g. > 100 MHz) are desired [24]. Transitions of hydrogen-like ions such as He^+ or Li^{2+} are of special interest [10]. They allow for tests of quantum electrodynamics, because these corrections to the 1s-2s transition scale with the atomic number Z^4 and they can be calculated due to their simple structure [25]. Reaching the extreme ultraviolet spectral region with frequency combs also offers the prospective of high-precision spectroscopy

of nuclei [26, 27], allowing for quantitative verification of nuclear models, as well as serving as a reference for next-generation optical clocks [24]. Considering time-domain applications on the other hand, pump-probe experiments with kHz repetition rate suffer from long integration times, especially those aiming at the detection of photoelectrons, as the number of electrons per pulse is limited by space charge effects [28]: If too many electrons are liberated per shot, the Coulomb repulsion results in a poor spatial and temporal resolution. For example, the observation of ultrafast dynamics on nanostructured surfaces requires photon energies around 100 eV [29], so that the photoelectrons leave the specimen within the desired temporal resolution. Here, ideally only one electron should be liberated per shot, resulting in typical acquisition times of more than one hour at 1 kHz repetition rate [30], which is significantly too long when many pictures for a time-resolved measurement are required. Thus, such an experiment demands for a source emitting short XUV pulses with high photon energies at MHz-level repetition rate. The same applies for other techniques such as time-resolved angular resolved photoemission spectroscopy (trARPES) [31] or cold-target recoil-ion momentum spectroscopy (COLTRIMS) [32].

The generation of high harmonics at photon energies around 100 eV requires intensities of about 10^{14} W/cm² [17, 18]. Even in a tight focusing geometry with a spot size of 15 μ m and 30 fs pulses, at more than 100 MHz repetition rate this implies an average power of several kilowatt, which is unattainable with state-of-the-art laser systems. Instead, one can couple the pulses from a high-power laser into an external resonator, a so called *enhancement cavity* [33, 34]. Here, a certain fraction of an incident pulse is transmitted through the input coupler. This part traverses the cavity and if the round-trip time is exactly the same as the time between two pulses from the seeding laser, then these two pulses can interfere such that energy is continuously coupled into the cavity. After a short build-up time a steady state is reached, in which the power coupled to the cavity is equal to the power lost during one cavity round-trip [35]. With low-loss optics, the power can be enhanced by orders of magnitude [36], allowing for the necessary intensities at repetition rates exceeding 100 MHz. Still, there are several challenges: The unique combination of ultrashort pulses, high average power, and high intensity is very demanding in terms of dispersion, thermal management, and the mirror's damage threshold.

1.2.2 Inverse-Compton scattering

With lasers operating at a wavelength around 1 μ m and 30-fs pulses, the photon energies from high-harmonic generation are limited to about 100 eV. In the future, this might be improved using shorter pulses and longer driving wavelength (e.g. thulium doped lasers operating at 2 μ m wavelength). However, many imaging applications require coherent hard x-ray radiation with photon energies of several keV, for which high-harmonic

generation is extremely inefficient or even impossible.

As an alternative to HHG, inverse-Compton scattering (also known as Thomson scattering) [37] can be used for the generation of photon energies of several keV. The near-infrared photons are backscattered from relativistic electrons. Even with compact electron accelerators, spatially coherent hard x-ray radiation with photon energies in the keV range can be obtained [38–40]. Several groups proposed this scheme in conjunction with enhancement cavities, for which average powers on the order of 1 MW with picosecond pulses are targeted [40, 41]. Coherent hard x-ray radiation is otherwise only available from large-scale facilities, such as synchrotrons or free-electron lasers. Inverse-Compton based sources would bring techniques requiring large-scale facilities to small-scale laboratories.

1.3 Research Objectives

This thesis treats the design, implementation, and application of ultrashort-pulse enhancement cavities at unprecedented pulse duration and average power levels. Based on a review of the theoretical background in Chapter 2, design goals and their fulfilment for high-power enhancement cavities are developed in Chapter 3. Here, large spot sizes on all optics in a cavity design robust against maladjustment is of utmost importance [42]. Such a cavity was implemented and used for power scaling experiments with ultrashort pulses, as described in Chapter 4. Custom optics with superior thermal properties in conjunction with a state-of-the-art fibre laser system allowed for average powers of 400 kW and 670 kW with 250 fs pulses and 10 ps pulses, respectively [43]. This constitutes an improvement of more than one order of magnitude over previous results [44]. In Chapter 5, the same methodology is applied for even shorter pulses of 30 fs and high-harmonic generation was pursued with these pulses at average powers of about 10 kW. This allowed for photon energies exceeding 100 eV at 250 MHz repetition rate with nW-level average power [45]. Compared to other experiments with multi-MHz repetition rates, the power was improved by more than two orders of magnitude, paving the way for frequency comb spectroscopy at these photon energy levels.

CHAPTER 2

Theoretical background

This chapter reviews the theoretical background necessary to understand the thesis, both its theoretical and experimental parts. In Section 2.1, Gaussian beams as a solution of the paraxial wave equation are introduced. Based on this, stable optical resonators and their eigenmodes are discussed in Section 2.2. The energy relations of passive optical resonators, so called enhancement cavities, in the steady-state follow in Section 2.3. As high powers play a central role in this thesis, thermal effects in laser optics are discussed in Section 2.4.1. The chapter closes with a summary of high-order harmonic generation in Section 2.5.

2.1 Laser beams in the paraxial approximation

Good introductions into this topic can be found in [46–48].

2.1.1 Fundamental Gaussian beam

The propagation of electromagnetic waves is described by Maxwell's equations. From them, a scalar wave equation for linearly polarised fields $u(x, y, z)$ can be derived,

$$[\Delta + k^2] u(x, y, z) = 0. \quad (2.1)$$

Here, $\Delta = \partial_x^2 + \partial_y^2 + \partial_z^2$ is the Laplacian and $k = 2\pi/\lambda$ is the wavenumber for the wavelength λ . Provided that the wavefront normals have a small angle with the propagation axis (z -axis), this equation can be simplified into the paraxial wave equation for fields $\Psi(x, y, z) = u(x, y, z) \cdot \exp(ikz)$:

$$\Delta_{\perp} \Psi(x, y, z) - 2ik \frac{\partial \Psi}{\partial z}(x, y, z) = 0. \quad (2.2)$$

The most important solution of this equation is the fundamental Gaussian beam (TEM₀₀), which can be introduced as the following ansatz with a phase function $P(z)$,

$$\Psi(x, y, z) = \exp \left[-i \left(P(z) + \frac{k}{2q(z)}(x^2 + y^2) \right) \right], \quad \text{with} \quad (2.3)$$

$$\frac{1}{q(z)} = \frac{1}{R(z)} - i \frac{\lambda}{\pi w(z)^2}. \quad (2.4)$$

The *complex beam parameter* $q(z)$ is determined by the wavefront radius of curvature $R(z)$ and the *beam radius* $w(z)$. For $x^2 + y^2 = w^2$, the beam intensity $I(x, y, z) \propto |E(x, y, z)|^2$ drops to $1/e^2$ of its maximum value. By substituting Eq. (2.3) into Eq. (2.2), one can find a differential equation for $P(z)$, which solution is given by

$$iP(z) = \log \sqrt{1 + \left(\frac{\lambda z}{\pi w_0^2} \right)^2} - i \arctan \left(\frac{\lambda z}{\pi w_0^2} \right), \quad (2.5)$$

where w_0 denotes the *beam waist*. While the first term describes a reduction of the on axis amplitude due to lateral spreading (energy conservation), the second term describes the so-called *Guoy-phase*, $\phi_{\text{Guoy}} = -\arctan(z/z_R)$ with the *Rayleigh-length* $z_R = \pi w_0^2/\lambda$. The phase front of a Gaussian beam upon propagation through a focus is shifted by half a wavelength in comparison to a plane wave.

2.1.2 Orthonormal Gauss-Hermite basis

In the following, a rectangular coordinate system with well-defined x - and y -directions is assumed. In this case, the solution of Eq. (2.2) can be split into

$$\Psi_{nm}(x, y, z) = \Psi_n(x, z) \cdot \Psi_m(y, z). \quad (2.6)$$

With this ansatz the one-dimensional Gauss-Hermite modes of order n can be found,

$$\Psi_n(x, z) = \left(\frac{2}{\pi} \right)^{1/4} \sqrt{\frac{\exp [i(2n+1)\phi_{\text{Guoy}}]}{2^n n! w(z)}} H_n \left(\frac{\sqrt{2}x}{w(z)} \right) \exp \left[-i \frac{kx^2}{2q(z)} \right]. \quad (2.7)$$

Here, H_n are the Hermite-polynomials of order n . These modes form a complete orthonormal basis, i.e. they fulfil the relation

$$\langle \Psi_n, \Psi_m \rangle = \int_{-\infty}^{\infty} \Psi_n(x) \cdot \Psi_m(x)^* dx = \delta_{nm}, \quad (2.8)$$

where $*$ refers to the complex conjugate and δ_{nm} to the Kronecker-delta. Thus, any beam $U(x, z)$ can be expanded into

$$U(x, z) = \sum_{n=0}^{\infty} c_n \cdot \Psi_n(x, z), \quad (2.9)$$

with complex coefficients given by the overlap integral

$$c_n = \int_{-\infty}^{\infty} U(x, z) \cdot \overline{\Psi_n(x, z)} dx. \quad (2.10)$$

Note that according to Eq. (2.7) the phase-shift of a mode Ψ_n is given by $(n + 1/2)\phi_{\text{Guoy}}$. Therefore, the higher-order modes acquire a stronger phase shift than the fundamental mode. This results in different round-trip times for Gaussian-Hermite modes in resonators as discussed in Section 2.2.

2.1.3 Orthonormal Gauss-Laguerre basis

Analogously, in cylindrical coordinates, a set of solutions for the paraxial wave equation can be found, namely the Gaussian-Laguerre modes $\Psi_{pl}(r, \theta, z)$. For radial symmetry ($l = 0$) they read

$$\Psi_p(r, z) = \frac{2}{w} L_p \left(\frac{2r^2}{w^2} \right) \exp \left[-i \frac{kr^2}{2q(z)} \right]. \quad (2.11)$$

L_p are the Laguerre polynomials of order p . These modes are orthonormal with respect to the scalar product

$$\langle \Psi_n, \Psi_m \rangle = \int_{-\infty}^{\infty} \Psi_n(r) \cdot \overline{\Psi_m(r)} \cdot r dr = \delta_{nm}. \quad (2.12)$$

In the following, these modes will be used for simplified 1D model calculations. However, in most cases the Gaussian-Hermite modes provide a better model for real laser beams, as astigmatism is ubiquitous in many laser setups.

2.1.4 Propagation of Gaussian beams: The ABCD law

In ray-optics, the propagation of optical rays defined by a vector $\mathbf{r} = (x, \alpha)^T$, where x denotes the distance and α the angle to the optical axis, can be described using the

so-called ABCD matrices, where A, B, C, and D refer to the matrix elements (row-wise from left to right). For example, the free-space propagation over a distance d is described by \mathbf{P}_d and the focusing of a thin lens with focal length f by \mathbf{L}_f :

$$\mathbf{P}_d = \begin{pmatrix} 1 & d \\ 0 & 1 \end{pmatrix} \quad \text{and} \quad \mathbf{L}_f = \begin{pmatrix} 1 & 0 \\ -1/f & 1 \end{pmatrix}. \quad (2.13)$$

A comprehensive list of ABCD matrices can be found in textbooks such as [46]. The effect of these optical elements is given by multiplication, for instance, $\mathbf{r}(z+d) = \mathbf{P}_d \cdot \mathbf{r}(z)$. Optical systems are constructed by multiplication of the element's matrices in reverse order, i.e. the first element of the system is on the very right of the matrix product.

Apart from optical rays, also Gaussian beams can be transformed using ABCD matrices via the so-called ABCD law. The derivation of this formula can be found in [46]. The remarkably simple outcome is that the q-parameter is transformed according to

$$q' = \frac{Aq + B}{Cq + D} \quad \text{or} \quad \frac{1}{q'} = \frac{C + D/q}{A + B/q}. \quad (2.14)$$

Using this formalism, a generalized Guoy-shift of a Gaussian beam, characterised by q , upon propagation through a optical system, described by an ABCD matrix, can be extracted [46, 49]:

$$\phi_{\text{Guoy}} = \arg \left[(A + B/q)^{-1} \right]. \quad (2.15)$$

2.2 Stable optical resonators

This section is based on [46].

2.2.1 Stability criteria

Optical resonators are mirror arrangements for either standing light waves (linear resonator) or travelling waves (ring resonator). In order to be stable, optical resonators must fulfil three criteria: (i) A eigenmode, i.e. a beam that reproduces itself after one round-trip, must exist, (ii) this eigenmode must be confined to a finite dimension, and (iii) it must be perturbation stable, i.e. small perturbation of the transverse beam profile must not grow upon multiple round-trips.

An eigenmode exists, if the q-parameter is recovered after one round-trip, i.e. $q' = q$ in Eq. (2.14). The solution of this quadratic equation in $1/q$ is given by (using the fact that $AD - BC = 1$)

$$\left(\frac{1}{q} \right)_{1/2} = \frac{D - A}{2B} \mp \frac{1}{B} \sqrt{\left(\frac{A + D}{2} \right)^2 - 1}. \quad (2.16)$$

For the mode to be confined to a finite dimension, this q-parameter must be complex. According to Eq. (2.4) this is the case for

$$-2 < A + D < 2. \quad (2.17)$$

Comparison of Eq. (2.16) with Eq. (2.4) yields a unique eigenmode, as w and λ must be positive:

$$R = \frac{2B}{D - A} \quad \text{and} \quad w = \left[\frac{\pi}{\lambda|B|} \sqrt{1 - \left(\frac{A + D}{2}\right)^2} \right]^{-1/2} \quad (2.18)$$

This eigenmode is also perturbation stable, see [46]. For resonators, the generalized round-trip Guoy-phase from Eq. (2.15) can be written as [49]

$$\phi_{\text{Guoy}} = \text{sign}(B) \arccos\left(\frac{A + D}{2}\right). \quad (2.19)$$

2.2.2 Resonators with misaligned elements

In the ABCD-matrix formalism, the effect of misaligned elements can be considered by adding a misalignment vector [50] with parameters Δx and $\Delta \alpha$,

$$\begin{pmatrix} x' \\ \alpha' \end{pmatrix} = \begin{pmatrix} A & B \\ C & D \end{pmatrix} \cdot \begin{pmatrix} x \\ \alpha \end{pmatrix} + \begin{pmatrix} \Delta x \\ \Delta \alpha \end{pmatrix}, \quad (2.20)$$

which is equivalent to

$$\begin{pmatrix} x' \\ \alpha' \\ 1 \end{pmatrix} = \begin{pmatrix} A & B & \Delta x \\ C & D & \Delta \alpha \\ 0 & 0 & 1 \end{pmatrix} \cdot \begin{pmatrix} x \\ \alpha \\ 1 \end{pmatrix}. \quad (2.21)$$

These 3×3 matrices can also be multiplied to model an optical system such as an optical resonator [50]. For an unperturbed resonator, the optical axis is given by the ray vector $(0, 0, 1)^T$. However, in the presence of misaligned elements ($\Delta x, \Delta \alpha \neq 0$), this ray is not recovered after one round-trip. Instead, the optical axis of a misaligned resonator is therefore given by the eigenvector with eigenvalue 1 of the 3×3 resonator round-trip matrix. It is given by [50]

$$x_0 = \frac{(1 - D)\Delta x + B\Delta \alpha}{2 - A - D} \quad \text{and} \quad \alpha_0 = \frac{(1 - A)\Delta \alpha + C\Delta x}{2 - A - D}. \quad (2.22)$$

These formulas will be used in Section 3.4 to analyse the misalignment sensitivity of enhancement cavities.

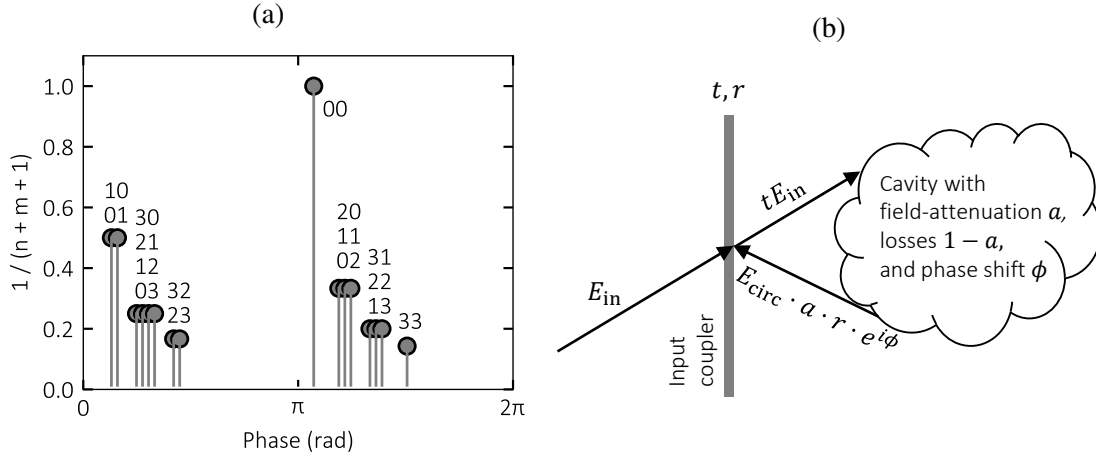


Figure 2.1 – (a) The round-trip phase for different Gaussian-Hermite modes in an astigmatic cavity. The height of the stems indicate the mode-order $n + m$. (b) The interference condition of the circulating field in an enhancement cavity.

2.2.3 Imaging resonators

An imaging resonator is a resonator in which *any* beam or ray reproduces itself after one round-trip, i.e. it is described by a unity matrix ($A = D = 1$ and $B = C = 0$) [51]. From Eq. (2.22), one can see that there is no optical axis in that definition, because the denominator vanishes. This results in a high misalignment sensitivity of such resonators [52]. However, arbitrary beam profiles may be obtained in such resonators, so that they might have applications for certain enhancement cavity experiments.

2.2.4 Transverse mode spectrum

The fact that according to Eq. (2.7) higher-order modes acquire a stronger phase shift upon propagation results in a mode-dependent resonance condition. The overall round-trip phase of a mode must be a multiple of 2π ,

$$kL + \left(m + \frac{1}{2}\right) \phi_{\text{Guoy}}^{\text{sagittal}} + \left(n + \frac{1}{2}\right) \phi_{\text{Guoy}}^{\text{tangential}} = 2\pi n, \quad n \in \mathbb{N}, \quad (2.23)$$

where L denotes to the resonator length. In the presence of astigmatic elements, the Guoy phase will in general be different for the sagittal and tangential planes of the resonator. Typically the astigmatism will be small, so that modes with equal mode sum $m + n$ are only slightly degenerated, see the example in Fig. 2.1(a). Thus, a resonator constitutes a spatial mode filter.

2.3 Enhancement cavities

Enhancement cavities are passive optical resonators to which light from a laser can be coherently coupled. If the resonance condition Eq. (2.23) is fulfilled, the incoming power can be enhanced by orders of magnitude provided that the intracavity losses are small and the input coupler is chosen properly. This section outlines how these factors affect the enhancement. This section closely follows [47].

2.3.1 Energy relations in enhancement cavities

An enhancement cavity consists of an input coupler with field transmission $t(\omega)$ and field reflectivity $r(\omega)$ and other optical elements, arranged to form a stable optical resonator. The other elements introduce losses to the circulating field, so that after one round-trip the circulating field $E_{\text{circ}}(\omega)$ is attenuated to $a(\omega)E_{\text{circ}}(\omega)$. Including the phase shift $\phi(\omega)$ upon propagation through the resonator, the steady-state condition as depicted in Fig. 2.1b, for the intracavity field reads

$$E_{\text{circ}}(\omega) = t(\omega)E_{\text{in}}(\omega) + a(\omega)r(\omega)e^{i\phi(\omega)}E_{\text{circ}}(\omega), \quad (2.24)$$

i.e. in the steady state the power coupled to the cavity compensates for the total losses $r(\omega)a(\omega)$ during one round-trip. The fact that all parameters are functions of the laser frequency ω has important consequences for ultrashort pulse enhancement cavities (see Section 2.3.4). For now, this dependence will be dropped. Then, the intracavity power P_{circ} is given by

$$P_{\text{circ}} = |E_{\text{circ}}|^2 = \left| \frac{tE_{\text{in}}}{1 - ar e^{i\phi}} \right|^2 = \frac{t^2 P_{\text{in}}}{(1 - ar)^2 + 4ar \sin^2(\phi/2)}, \quad (2.25)$$

with the incoming power P_{in} . The on-resonance ($\phi = 0$) power enhancement \mathcal{E}_0 reads

$$\mathcal{E}_0 = \left. \frac{P_{\text{circ}}}{P_{\text{in}}} \right|_{\phi=0} = \frac{1 - r^2}{(1 - ar)^2}. \quad (2.26)$$

Here, an idealised input coupler with $r^2 + t^2 = 1$ was assumed. Any losses of the input coupler (scattering, absorption) can be included into the round-trip attenuation a . From Eq. (2.25) the full-width at half maximum (FWHM) of the cavity resonance linewidth $\Delta\phi$ can be calculated:

$$\Delta\phi = 4 \arcsin \left(\frac{1 - ar}{2\sqrt{ar}} \right) \approx 2 \frac{1 - ar}{\sqrt{ar}}. \quad (2.27)$$

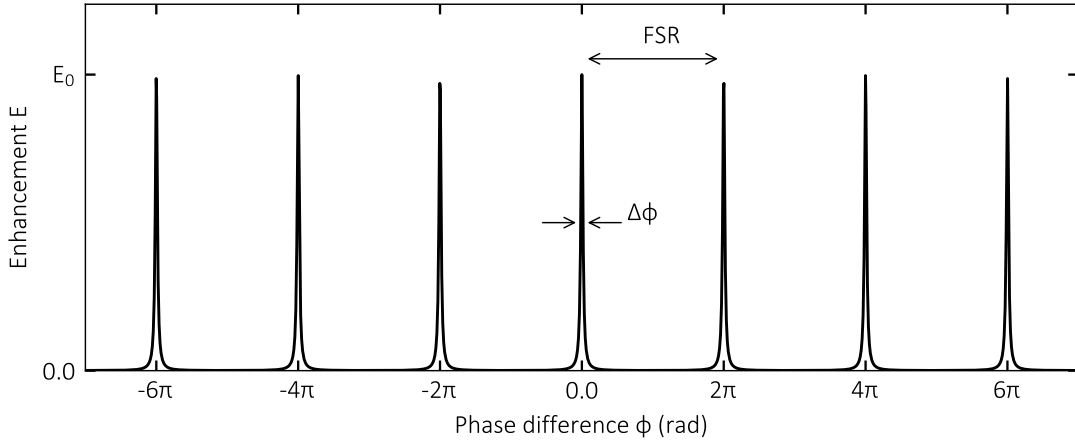


Figure 2.2 – The enhancement as a function of the phase ϕ between the circulating and incident field. A phase shift of 2π is given by one wavelength λ in terms of a cavity length change, or by c/L in terms of a change of the incident laser frequency.

The finesse \mathcal{F} is defined as the ratio between distance of two resonances (also called free spectral range, FSR) and their linewidth,

$$\mathcal{F} = \frac{FSR}{\Delta\phi} = \frac{\pi\sqrt{ar}}{1-ar}, \quad \text{with } FSR = 2\pi. \quad (2.28)$$

In phase space, the free spectral range is 2π . Physically, such a phase difference can be obtained either by cavity length change of one wavelength λ , or by changing the incident frequency ν by c/L .

2.3.2 Perturbations

In the presence of a phase mismatch ϕ , the enhancement drops according to Eq. (2.25). Together with Eq. (2.26) and Eq. (2.28) it can be written as [35]

$$\mathcal{E}(\phi) = \frac{\mathcal{E}_0}{1 + (2\mathcal{F}/\pi)^2 \sin^2(\phi/2)}, \quad (2.29)$$

i.e. the influence of a phase mismatch on the power enhancement scales with \mathcal{F}^2 . Therefore, a high finesse cavity is much more susceptible to perturbations such as laser phase noise or mechanical vibrations. In practice, this often sets an upper limit for the finesse.

The phase ϕ is the relative phase between the incident laser field and the circulating one. Thus, there are two distinct types of perturbations: Fluctuations of the incident laser frequency ν or wavelength λ (phase noise) and changes of the cavity length L (e.g.

by mechanical vibrations, thermal mirror deformation, intracavity non-linearities). In terms of the incident frequency ν , the *FSR* is given by c/L (speed of light c) and the resonance linewidth by

$$\Delta\nu = \frac{c}{\mathcal{F}L}, \text{ or} \quad (2.30)$$

$$\Delta\lambda = \frac{\lambda^2}{c}\Delta\nu = \frac{\lambda^2}{\mathcal{F}L}. \quad (2.31)$$

It depends on both the finesse and the cavity length, i.e. increasing either of the two makes the experiment more susceptible to phase noise. In terms of the cavity length L , the *FSR* is given by the wavelength λ . The resonance linewidth with respect to cavity length changes in then

$$\Delta L = \frac{\lambda}{\mathcal{F}}. \quad (2.32)$$

In contrast changes of the laser's wavelength, it does not depend on the absolute cavity length, but only on the finesse. Cavity length changes due to, for example, vibrations or thermal effects, do not result in stronger fluctuations of the enhancement in a very long cavity compared to a short one. The linewidths from Eq. (2.32) and Eq. (2.31) differ by a factor $N = L/\lambda$. This is exactly the number of optical waves in the resonator, as a change of all N waves in the cavity by $\Delta\lambda$ has the same effect as a change of the cavity length by $N\Delta\lambda$.

2.3.3 Impedance-matched and input-coupler-limited enhancement

It is instructive to consider the two important cases $r = a$ called *impedance-matched* and $a \cdot r \approx r$ called *input coupler limited*. In the first case, the enhancement is given by

$$\mathcal{E}_0^{\text{IM}} = \frac{1}{1 - r^2} = \frac{1}{t^2} \quad (2.33)$$

and the finesse by

$$\mathcal{F}^{\text{IM}} = \frac{\pi r}{1 - r^2} \approx \frac{\pi}{1 - r^2} = \pi \mathcal{E}_0^{\text{IM}}. \quad (2.34)$$

The approximation is valid for high-finesse cavities, i.e. $r \approx 1$. In the impedance matched case, the highest possible enhancement for a given cavity attenuation a is achieved. With state-of-the-art mirrors with losses on the level of a few ppm, the enhancement can in principle exceed 10^6 . However, the linewidth of such a cavity is so narrow, that stabilising a laser to it is very challenging and therefore impractical. Additionally, in many cases the achievable power and intensity in the cavity is limited by thermal effects and mirror damage. Then, one instead *sets* the enhancement depending on the available laser power by proper choice of the input coupler transmission. With low losses in the cavity, one can then use the approximation $a \approx 1$. In this case, the

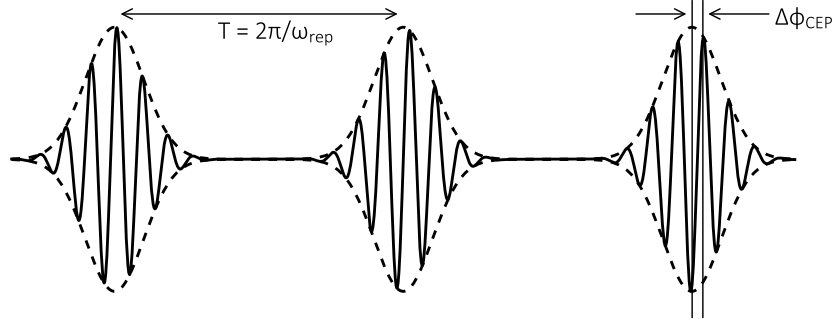


Figure 2.3 – Depiction of an pulse train with repetition rate ω_{rep} . The frequency with that the carrier-to-envelope phase $\Delta\phi_{\text{CEP}}$ changes determines the offset of the frequency comb, ω_0 .

enhancement and finesse are given by

$$\mathcal{E}_0^{\text{ICL}} = \frac{1 - r^2}{(1 - r)^2} = \frac{1 + r}{1 - r} \approx \frac{2}{1 - r} \quad (2.35)$$

$$\mathcal{F}^{\text{ICL}} = \frac{\pi\sqrt{r}}{1 - r} \approx \frac{\pi}{1 - r} = \frac{\pi}{2} \mathcal{E}_0^{\text{ICL}}. \quad (2.36)$$

For a given enhancement factor, the finesse in the input coupler limited case (Eq. (2.36)) is half of that in the impedance matched case (Eq. (2.34)). Thus, the cavity losses should always be kept low and the enhancement should ideally be set by the input coupler transmission.

2.3.4 Frequency combs and ultrashort pulse enhancement cavities

For ultrashort pulse enhancement cavities, laser pulses from a so-called frequency comb are coupled into the cavity. The spectrum of a comb can be written as

$$A(\omega) = G(\omega) \cdot \left(n \cdot \omega_{\text{rep}} + \omega_0 \right), \quad \text{with } n \in \mathbb{N}. \quad (2.37)$$

Here, ω_{rep} is the repetition rate of the comb, $G(\omega)$ is the envelope function of the spectrum and ω_0 is the offset-frequency. One important point is that the spectrum consists of equidistant comb modes with a spectral separation of ω_{rep} . In contrast, the resonances according to Eq. (2.29) of an enhancement cavity are in general not equidistant, as the round-trip phase $\phi(\omega)$ is a function of the frequency due to dispersion of the cavity optics. In order to couple the whole spectrum of a frequency comb into an enhancement cavity, the cavity round-trip phase must be close to zero for the whole incident spectrum as given by $G(\omega)$.

The frequencies ω_0 and ω_{rep} are also called *comb parameters*. In the time domain, a comb describes a pulse train with periodicity $T = 2\pi/\omega_{\text{rep}}$. The offset frequency can be interpreted as the frequency with that the carrier to envelope phase (CEP) changes, i.e. the phase describing the offset of the pulse's electric field under the envelope. It is often also called carrier-to-envelope offset frequency, ω_{CEO} . This is shown in Fig. 2.3.

2.4 Thermal effects in laser optics

Thermal lensing in crystals is a common problem for the power scaling of lasers [53]. Absorption of the pump energy in the laser crystal results in a temperature gradient. As the refractive index is in general temperature-dependent, the crystal will act as a thermal lens in transmission, typically with a positive focal length. The enhancement cavities considered here are free of any transmissive elements. Therefore, the achievable intracavity powers are much higher than that of state-of-the-art high-power lasers [43, 44]. However, at very high power levels the absorption of light in the cavity mirror's coating can lead to significant thermal deformation of the substrate, resulting in a defocusing thermal lens upon reflection. In this section, the deformation, focusing effect, and aberrations of laser mirrors is discussed.

2.4.1 Heat equation and elastic deformation

The substrate's temperature profile $T(t, \mathbf{r})$ can be calculated from the heat equation (without internal heat generation),

$$[\rho C \partial_t - \kappa \Delta] T(\mathbf{r}) = 0, \quad (2.38)$$

where ρ, C, κ denote the substrate's density, specific heat, and thermal conductivity, respectively [54, 55]. If not noticed otherwise, the time-dependence is dropped in the following. In this equation, heat sources are considered by boundary conditions. As the coating is much thinner ($< 10 \mu\text{m}$) compared to the substrate ($> 5 \text{mm}$), the heating can be modelled as a 2D heat source at the mirror surface of the substrate. When the coating lies in the x-y-plane the boundary condition reads

$$\kappa \left[\frac{\partial T}{\partial z} \right]_{z=0} = \eta_{\text{abs}} I(x, y) - \sigma \epsilon \left[T(x, y, 0)^4 - T_0^4 \right], \quad (2.39)$$

with the absorption coefficient η_{abs} , the intensity profile of the impinging beam $I(x, y)$, the Stefan-Boltzmann constant σ , the emissivity ϵ , and the ambient temperature T_0 [54]. This equation describes a heat deposition given by absorption and heat removal according to the Stefan-Boltzmann law. The other boundary conditions are similar, except that no heat is deposited on these surfaces, i.e. the first term vanishes.

In order to calculate the deformation of the substrate induced by thermal expansion, Hooke's law describing the relation between the strain tensor E_{ij} and the stress tensor Θ_{ij} has to be solved [54, 56],

$$\Theta_{ij} = \delta_{ij} [\lambda \text{Tr}(E_{ij}) - \beta T] + 2\mu E_{ij}. \quad (2.40)$$

Here, λ and μ are the Lamé-parameters, and β is the stress thermal modulus. For this tensor equation, Einstein's sum convention applies. In general, it can only be solved numerically, for instance, using the finite-element method. In the following, the commercial software Comsol is used for that. In Refs. [54–56] these equations have been solved analytically for arbitrary beam profiles $I(r)$ with circular symmetry. The deformation of the coating then reads

$$Z(r) = \sum_{s=0}^{\infty} U_s [1 - J_0(\zeta_s r/a)] - B_s r^2, \quad \text{with} \quad (2.41)$$

$$U_s = \frac{\alpha(1+\nu)\epsilon P_{\text{abs}} a^2 p_s}{\kappa} \frac{\zeta_s + \chi - (\zeta_s - \chi) \exp(-2\zeta_s h/a)}{\zeta_s (\zeta_s + \chi)^2 - (\zeta_s - \chi)^2 \exp(-2\zeta_s h/a)}, \quad \text{and} \quad (2.42)$$

$$B_s = \frac{6\alpha\chi(1-\nu)\epsilon P a^3 p_s J_0(\zeta_s)}{\kappa h^3} \frac{1 - \zeta_s h/2/a - (1 + \zeta_s h/2/a) \exp(-\zeta_s h/a)}{\zeta_s^4 (\zeta_s - \chi + (\zeta_s + \chi) \exp(-\zeta_s h/a))} \quad (2.43)$$

Here, ζ_s is the s -th root of the function $f(\zeta) = \zeta J_1(\zeta) - \chi J_0(\zeta)$ (J_i are the Bessel-functions of the i -th kind). The incident intensity profile $I(r)$ can be expanded in a series

$$I(r) = P \sum_{s=0}^{\infty} p_s J_0(\zeta_s r/a), \quad (2.44)$$

$$\Rightarrow p_s = \frac{1}{P} \frac{2\zeta_s^2}{a^2(\chi^2 + \zeta_s^2) J_0^2(\zeta_s)} \int_0^a I(r) J_0(\zeta_s r/a) r dr. \quad (2.45)$$

The other constants are (with values for fused silica): α : Thermal expansion coefficient (1.38 K · W/m), κ : Coefficient of thermal conductivity ($5.4 \times 10^{-7} \text{ K}^{-1}$), P_{abs} : absorbed power in the coating, a : radius of the substrate, h : thickness of the substrate, and $\chi = 4\epsilon\sigma T_0^3 a/\kappa$.

2.4.2 Thermal lenses: Focusing and aberrations

Upon reflection, the deformation profile $Z(r)$ from Eq. (2.41) results in a spatial phase $\exp[ik2Z(r)]$. The effect of this phase can be classified into a (de)focusing effect and aberrations: As the fundamental Gaussian beam Eq. (2.7) has a parabolic phase front, the parabolic part of $Z(r)$ only changes the beam divergence. Any non-parabolic part, however, must be considered by adding higher-order modes according to Eq. (2.9). Thus,

the non-parabolic parts, called aberrations, couple power into higher-order modes. In order to quantify the aberrations, a best-fit parabola $P(r) = r^2/4f + d$ with focal length f must be found. For this fit, the focal length is chosen such that it minimises the aberrations for the incident beam Ψ . Mathematically, this can be written as

$$\max_f |\langle \Psi, \Phi \Psi \rangle|^2, \quad \text{with} \quad \Phi_f(r) = \exp [ik (2Z(r) - P_f(r))]. \quad (2.46)$$

Φ is called the aberration phase. Note that this focal length depends on the beam Ψ , in particular on its width. Calculation of $\partial_f |\langle \Psi, \Phi \Psi \rangle|^2 = 0$ yields [54]

$$f = \frac{1}{4} \frac{\langle r^2 \rangle \langle r \rangle - \langle r^3 \rangle}{\langle 2Z \rangle \langle r \rangle - \langle 2Zr \rangle} \quad (2.47)$$

with the shorthand notation $\langle \cdot \rangle = \langle \Psi, \cdot \Psi \rangle$.

In Fig. 2.4a, the optical path length difference $2Z(r)$ given by the mirror deformation is plotted from Eq. (2.41) and from a numerical solution obtained with Comsol. For a sufficiently high order of the series (here 15), the agreement is excellent, so that numerical solutions are only required if no radial symmetry exists. The best-fit parabola is also plotted. With it, the strength of the aberrations can be calculated according to

$$l_{\text{ab}} = 1 - |\langle \Psi, \Phi_{\text{best}} \Psi \rangle|^2, \quad (2.48)$$

where Φ_{best} is the phase factor from Eq. (2.46) with the best-fit parabola. The strength of the aberration corresponds to the power coupled from the beam Ψ into other modes. In the absence of mode degeneration, this corresponds to losses in the enhancement cavity.

2.4.3 Winkler's formula

In [57], a formula for the estimation of the thermally induced focal length was derived. It reads

$$\frac{1}{f_{\text{thermal}}} = -\gamma \frac{\alpha P_{\text{abs}}}{\kappa w_{\text{in}}^2}, \quad (2.49)$$

with the coefficient of thermal expansion α , the thermal conductivity κ , the beam radius of the impinging beam w_{in} and the absorbed power in the coating P_{abs} . Here, the proportionality constant γ is found by fitting the focal length from this equation to that of Eq. (2.41), see Fig. 2.4b. For $\gamma = 0.8$ a good agreement is achieved.

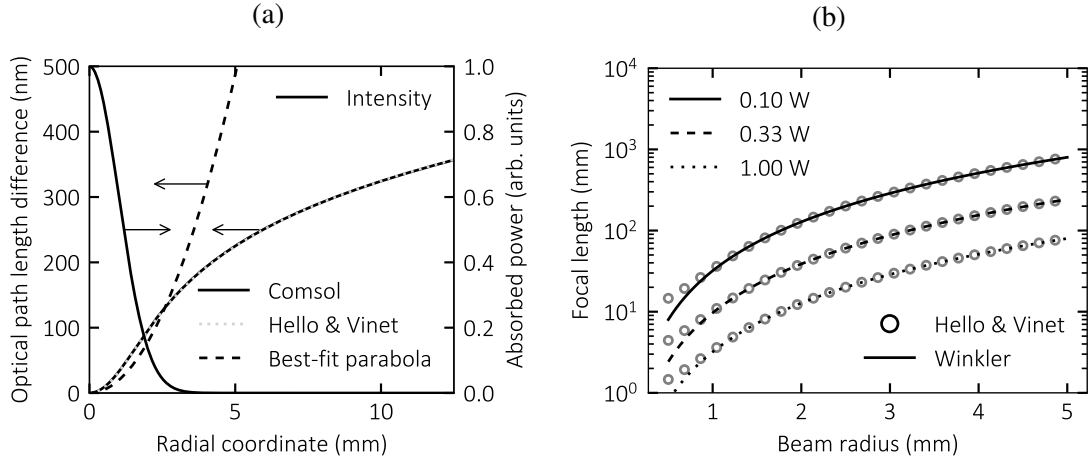


Figure 2.4 – (a) The optical path length difference $2Z(r)$ due to deformation of a 6-mm thick fused silica mirror with 1 W of absorbed power in the coating from a incident Gaussian beam with radius 2 mm. With a sufficient order of the series (here 15), the analytical solution (Hello & Vinet) agrees with the numerical one obtained with Comsol. A best-fit parabola minimising the aberrations was fitted to it. (b) Comparison of Eq. (2.49) with the focal length of the best-fit parabola calculated from the thermal deformation for a range of parameters. For $\gamma = 0.8$ the agreement is good for $w > 1$ mm.

2.5 High-order harmonic generation

2.5.1 Microscopic picture

In a simple picture, the process of high-harmonic generation can be understood in three steps [17, 18]: (i) An atom is ionized by a multiphoton process, (ii) the liberated electron is accelerated in the laser field, and (iii) it can recombine with the parent ion emitting one photon with energy $E_p + E_{acc}$, where E_p is the ionization energy of the atom and E_{acc} the energy obtained from the acceleration. The ionization rate Γ for step (i) can be calculated from models such as PPT or ADK [58, 59]. By solving the equations of motion for the electron in the laser field for step (ii), one finds that there are two trajectories yielding the same energy transfer, called short and long trajectory. The probability for recombination in step (iii) is very low due to the spreading of the electron wave packet. Thus, the overall efficiency of HHG is limited to about 10^{-6} [60].

The photon energy is limited by the energy gained from the acceleration within one cycle of the laser field to

$$E_{\text{cutoff}} \approx E_p + 3.2E_{\text{pon}} = E_p + \frac{3.2e^2}{8\pi c^3 \epsilon_0 m_e} I \lambda^2. \quad (2.50)$$

Here, E_{pon} denotes the ponderomotive energy, which depends on the electron charge e ,

the vacuum permittivity ϵ_0 , the electron mass m_e , and the laser intensity I and wavelength λ . The cut-off can therefore be increased by a higher intensity and/or a longer wavelength. In practice, the driving intensity is limited by phase matching (see next section), or, in enhancement cavities, by intensity clamping [61–63].

The strength and phase of the emitting dipoles can be obtained by solving the time-dependent Schrödinger equation [64, 65] or by using the Lewenstein-model [18]. From these, simple scaling laws for the dipole strength d_q of harmonic order q can be obtained [60, 66],

$$d_q \propto \left(\frac{I}{I_{\text{cutoff}}} \right)^p, \quad I > I_{\text{cutoff}}, \quad (2.51)$$

with the intensity I_{cutoff} at which the harmonic order q is the cutoff according to Eq. (2.50). Here, the scaling parameter p is chosen to be 4.3 [66]. This simplification allows for qualitative investigation of the principles of high-harmonic generation as described in the next section. For quantitative results, the aforementioned models have to be used. However, for the calculation of the conversion efficiency, other quantities such as ionisation rates have a large uncertainty, so that the simple model is sufficient.

2.5.2 Phase matching

In order to generate harmonic radiation efficiently, the wave numbers k_0 of the driving field and k_q of the harmonic field must be as similar as possible. In a free-space geometry, there are three major factors giving rise to a wave vector mismatch [67]: (i) The Guoy-phase shift, (ii) the dipole phase, and (iii) the dispersion of the partly ionised gas target. The difference in wave number due to the Guoy-shift is given by

$$\Delta k_{\text{guoy}} = -q \frac{\partial \phi_{\text{Guoy}}}{\partial z} = -q \frac{z_R}{z^2 + z_R^2}, \quad (2.52)$$

and that due to the intensity dependent dipole phase by

$$\Delta k_{\text{dipole}} = -\alpha_l \frac{\partial I}{\partial z}, \quad (2.53)$$

with the dipole parameters $\alpha_1 = 2 \times 10^{14} \text{ cm}^2/\text{W}$ for the short trajectory and $\alpha_2 = 2 \times 10^{15} \text{ cm}^2/\text{W}$ for the long trajectory [66]. In the following, the dipole phase will be neglected, as it is only relevant for the long trajectory. The radiation emitted from the long trajectory in general has a higher beam divergence [68, 69]. In the following, it will be ignored, because the principles are the same for both trajectories. A further justification for this will be discussed in Chapter 5: The photons generated via the long trajectory are not coupled out of the enhancement cavity used for the experiments in this thesis.

The wave number of a partly ionized gas can be written as [70, 71]

$$k_{\text{gas}}(\lambda) = \frac{2\pi}{\lambda} + \frac{2\pi N_a \delta(\lambda)}{\lambda} + N_e r_e \lambda. \quad (2.54)$$

Here, r_e is the classical electron radius, N_a is the number density of neutral atoms and N_e the number density of free electrons. With the ionization fraction η and the number density of the gas N they are given by $N_e = \eta N$ and $N_a = (1 - \eta)N$. The dispersion parameter per number density is given by $\delta(\lambda) = (n_{\text{gas}} - 1)/N$ with the refractive index of the gas n_{gas} . The wave vector mismatch due to the gas is then given by

$$\Delta k_{\text{gas}} = q k_{\text{gas}}(\lambda) - k_{\text{gas}}(\lambda/q) \quad (2.55)$$

$$= q k_0 N \Delta \delta \left(1 - \frac{\eta}{\eta_{\text{crit}}} \right) \quad \text{for } q \gg \frac{1}{q}, \quad (2.56)$$

$$\text{with } \eta_{\text{crit}} = \left(1 + \frac{\lambda^2 r_e}{2\pi \Delta \delta} \right)^{-1}. \quad (2.57)$$

Here, $\Delta \delta = \delta(\lambda) - \delta(\lambda/q)$. As long as η is smaller than the critical ionization η_{crit} , the Δk_{gas} is positive. In this case, it can compensate for the Guoy-shift from Eq. (2.52). If the ionization fraction is larger, no phase matching is possible as all three terms have the same sign. The coherence length is given by $L_{\text{coh}} = \pi/|\Delta k|$.

In order to achieve phase matching, i.e. $\Delta k = \Delta k_{\text{gas}} + \Delta k_{\text{guoy}} = 0$, the number density N of the gas must be adjusted. In the focus, the Guoy-shift reduces to $\Delta k_{\text{guoy}}(0) = -q/z_R$. Then, the phase matching density N_{pm} is given by

$$N_{\text{pm}} = \frac{\lambda^2}{2\pi^2 w_0^2 \Delta \delta (1 - \eta/\eta_{\text{crit}})}. \quad (2.58)$$

The required number density therefore increases for tighter focusing, for weaker dispersion and for higher ionization fractions. Thus, the combination of light gases with low dispersion such as neon and tight focusing requires very high gas densities for phase matching [67, 72, 73], as will be demonstrated in Chapter 5.

2.5.3 High-harmonic generation in absorbing media

The overall efficiency of HHG is not only limited by phase matching, but also by reabsorption of the harmonic radiation in the generating gas. In [60], a one dimensional model for the generation efficiency of HHG is given. On axis, the photon flux at harmonic

Table 2.1 – Important properties of noble gases relevant for high-harmonic generation. I_p : ionization potential, N_{pm} : phase matching density of H40 and $w_0 = 15 \mu\text{m}$, η_{crit} : critical ionization for H40.

Gas	I_p (eV)	N_{pm} (N_{normal})	η_{crit} (%)
Xenon	12.13	0.67	5.24
Argon	15.76	1.40	2.59
Neon	21.56	6.29	0.59
Helium	24.59	9.96	0.37

frequency ω_q per time and area is given by

$$F_q = \frac{\omega_q}{4c\epsilon_0\hbar} \left| \int_0^{L_{\text{med}}} \rho d_q(z) \exp\left(-\frac{L_{\text{med}} - z}{2L_{\text{abs}}}\right) \exp(i\phi_q(z)) dz \right|^2. \quad (2.59)$$

Here, L_{med} is the length of the gas target, L_{abs} is its absorption length, ρ is the gas density, and $\phi_q(z)$ is the phase mismatch between the harmonic and fundamental field. This integral was solved for constant d_q and constant ρ [60]:

$$F_q \propto \rho^2 d_q^2 \frac{4L_{\text{abs}}^2}{1 + 4\pi^2(L_{\text{abs}}/L_{\text{coh}})^2} \left[1 + \exp\left(-\frac{L_{\text{med}}}{L_{\text{abs}}}\right) - 2 \cos\left(\frac{\pi L_{\text{med}}}{L_{\text{coh}}}\right) \exp\left(-\frac{L_{\text{med}}}{2L_{\text{abs}}}\right) \right] \quad (2.60)$$

This equation can be used to investigate the influence of laser pulse parameters like intensity and duration on the conversion efficiency. For cavity-enhanced HHG, this will be done in Chapter 5. One important outcome of [60] is, that for $L_{\text{med}} > 3L_{\text{abs}}$ and $L_{\text{coh}} > 5L_{\text{abs}}$ the harmonic yield is absorption limited, i.e. a further increase of the coherence length and/or medium length does not increase the flux any more.

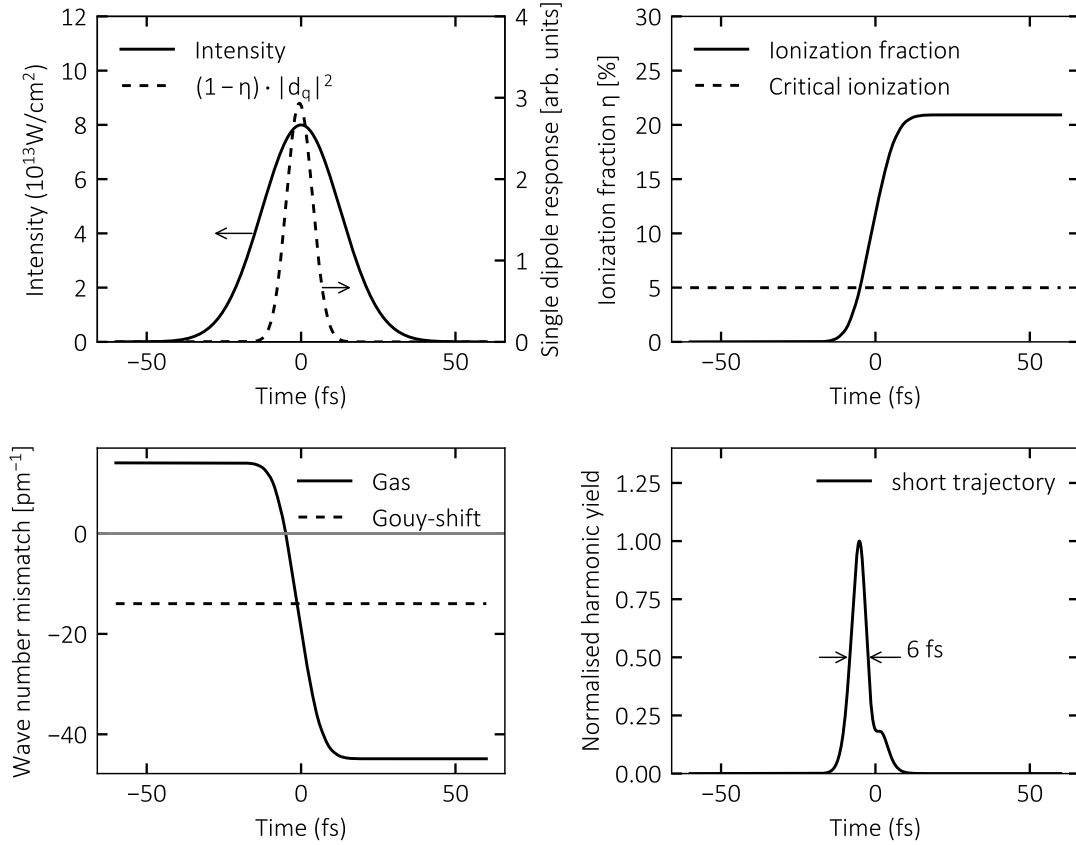


Figure 2.5 – From the intensity profile of a laser pulse (upper left, 30 fs), the ionization fraction η of the gas target was calculated with the PPT model ([58], upper right). From this, the dipole radiation (upper left) is given by $(1 - \eta) \cdot d_q$ (see Eq. (2.51)). Due to the ionization, the gas wave number mismatch changes over time (lower left). As soon as the ionization fraction exceeds the critical ionization, it cannot compensate the Guoy-shift any more and no phase matching is possible. Thus, the harmonic yield (lower right) according to Eq. (2.60) drops at the trailing edge of the pulse.

CHAPTER 3

Design of high-power enhancement cavities

This chapter deals with the design of high-power enhancement cavities for ultrashort pulses. In Section 3.1, design goals for high-power enhancement cavities are developed. Three example cavities are discussed in Section 3.2. They can be employed for applications such as high-harmonic generation or inverse-Compton scattering, whose specific requirements are discussed in Section 3.3. One important aspect for all these applications is robustness against perturbations. In Section 3.4, a metric for the misalignment sensitivity of enhancement cavities is introduced and investigated for the three cavity designs. The chapter closes with a discussion about the possibilities of astigmatic compensation in enhancement cavities in Section 3.5 with purely reflective optics.

3.1 Design considerations

Assumptions and laser induced damage

Here, stable optical resonators for high-finesse ($\mathcal{F} \gg 100$) setups are considered. Furthermore, it is assumed that no intracavity transmissive elements are present, but the theory can be readily extended for this case [74]. An empty cavity can support ultrashort pulses ($\ll 1$ ps) [33] and very high average powers ($\gg 1$ kW) [44] at the same time. Thus, both intensity-related effects such as mirror damage, and thermal lensing must be considered for the design. In the case of ultrashort pulses, the most important damage

mechanism of dielectric mirrors is avalanche ionization [75]. For this mechanism the peak intensity $I_{\text{peak}} = P_{\text{peak}}/A$ with the peak power P_{peak} and the illuminated area on the mirror A determines the damage threshold. Thus, to increase the achievable average power or peak intensity, the illuminated area on *all* cavity optics must be increased. In general this can be achieved by increasing the cavity length, by operation close to a stability edge, or by a combination of both. The disadvantage of the former is a reduced resonance linewidth, as discussed in Section 2.3.2. Note that even for pulsed operation with repetition rate f_{rep} the cavity length can be extended to integer multiples of the fundamental cavity length c/f_{rep} . However, in case of low-repetition-rate systems, these steps can be very large rendering this technique cumbersome. In the following sections, it will be illustrated that the operation close to a stability edge does not necessarily result in a higher sensitivity to perturbations.

Intensity discrimination

One important design criterion is to have at least one tight focus for frequency conversion processes like high-harmonic generation or Thomson-scattering. In particular for Thomson-scattering, intensities as high as possible are desired. Then, maximising the intensity discrimination, i.e. the ratio of the intensity in the focus to the highest intensity on any cavity mirror $D = I_0/I_{\text{mirror}}$, is crucial. As the intensity scales with the beam radius w^{-2} , this is equal to $D = w_{\text{mirror}}^2/w_0^2$, where w_{mirror} is the smallest beam radius on any mirror. From the propagation law for Gaussian-beams, $w(z) = w_0\sqrt{1 + (z/z_R)^2}$, with the Rayleigh-length $z_R = \pi w_0^2/\lambda$, follows $D = 1 + (z/z_R)^2 \approx (z/z_R)^2$ for $z \gg z_R$. When focusing a collimated beam with focal length f , the focus will be at $z = f$ with radius $w_0 = \lambda f/(\pi w)$. From this, it follows

$$D = \left(\frac{\lambda f}{\pi w_0^2} \right)^2 = \left(\frac{\pi w^2}{\lambda f} \right)^2 \quad (3.1)$$

These equations give relations for the intensity discrimination, the necessary beam size on the mirrors or focus size, and the focusing geometry. The intensity discrimination scales with the focal power squared and with the incident beam radius to the fourth power. Thus, tight focusing with large beams is desired. Ultimately, this is limited by thermal effects and aberrations, see Chapter 4.

Ring resonators

In the following, only ring resonators are considered, so that the interaction in the focus only takes place once per round-trip. This also allows for a simple geometric separation of the reflected beam at the input coupler from the incident one. However, the analysis of cavity sensitivity can also be used for linear resonators. For ring resonators, there will always be an astigmatism due to the non-zero angle of incidence on the focusing mirrors. In general, this will lead to a different position of the beam waist in the sagittal and tangential plane. However, if the resonator is symmetric with respect to the focal plane, the focus is in the middle of the focusing mirrors in both planes and the astigmatism manifests itself as a pure beam ellipticity, i.e. different beam radii in the sagittal and tangential plane emerge.

Planarity

Here, only planar cavities operated with a fundamental gaussian beam are considered. Then, any incoming polarization will be preserved in the cavity. Non-planar cavities can be used, for example, for astigmatic compensation. In this case, the intracavity polarisation depends both on the incident polarisation and the polarisation rotation during one round-trip, see Section 3.5. Also, the eigenmode cannot be written as product of two functions for the two transverse planes, so that the mathematical description of the cavity modes is more complicated [76]. Tailoring the intracavity mode can offer advantages for some applications even in plane resonators [77–80].

Summary

The very general design goals for high-power, ultrashort pulse cavities for frequency conversion are: (i) Large spot size on *all* optics, (ii) at least one tight focus, (iii) ring design, (iv) reduced astigmatism, and (v) robust against perturbations.

3.2 Cavity designs

3.2.1 Standard bow-tie cavity

The design goals are fulfilled by the so-called standard bow-tie cavity (SBT) at the inner stability edge. It consists of two identical focusing mirrors with radius of curvature R separated by a distance d and with round-trip length L . Commonly, this resonator is implemented using two or more plane folding mirrors as depicted in Fig. 3.1a. In principle, one folding mirror for a triangular geometry is sufficient. The stability range of the bow-tie resonator is given by

$$R < d < \frac{L - \sqrt{L^2 - 4LR}}{2}. \quad (3.2)$$

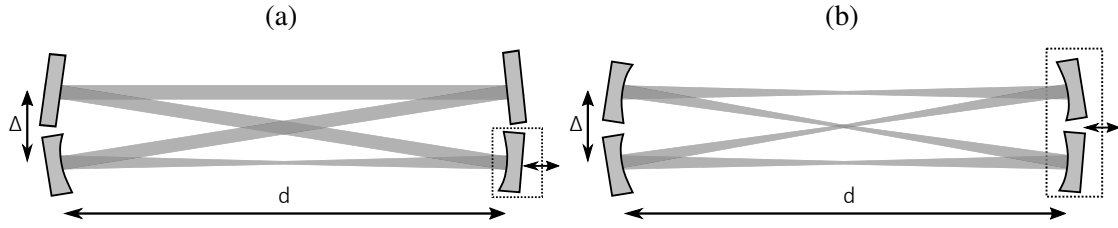


Figure 3.1 – (a) Schematic of a standard bow-tie resonator consisting of two curved mirrors with radius of curvature R separated by a distance d . The cavity round-trip length is L . In this configuration, the angle of incidence on the curved mirrors is given by $\beta_{\text{AOI}} = \arctan(\Delta/d)/2$. (b) The same for an all-curved-mirror cavity consisting of four identical curved mirrors.

Towards $d = R$ the inner stability edge is approached. Here, the beam is strongly focused between the curved mirrors and collimated in the other cavity arm, i.e. the beam size on all mirrors is nearly the same and large. At the outer stability edge, there is another focus in the long arm between the flat mirror(s), so that the beam is smaller on the folding mirror(s). For $R > L/4$ the outer stability edge does not exist and the cavity is stable up to $d = L/2$. For $d > L/2$ the two arms interchange.

The angle of incidence β_{AOI} on the curved mirrors depends on the focusing geometry. Using loose focusing (large R), it can become very small, as the distance between the curved mirrors increases according to Eq. (3.2). However, in order to obtain a tight focus with loose focusing, the cavity has to be operated very close to the stability edge. Here, the beam radius strongly depends on the mirror separation (see Fig. 3.3), so that even a small astigmatism leads to a significant beam ellipticity. The effective radius of curvature in the sagittal plane is given by $R_{\text{sag}} = R/\cos(\beta_{\text{AOI}})$ and that in the tangential plane by $R_{\text{tan}} = R \cdot \cos(\beta_{\text{AOI}})$. Thus, in the sagittal plane the stability edge is reached first, resulting in an elliptical beam with the larger axis in this plane. Depending on the required spot size in the focus, the focusing geometry should be optimized numerically taking into account the possible angle of incidence and how close to the stability edge the cavity has to be operated.

At the inner stability edge, the stability parameter $A+D$ approaches -2 . The round-trip Gouy-phase is approximately π , as there is almost no phase shift in the collimated arm and a phase shift of nearly π in the focused arm. This is consistent with Eq. (2.19). For this stability edge, the alignment sensitivity is not immediately obvious from Eq. (2.22), but in the following it will be shown that it is insensitive towards mirror tilts.

3.2.2 All-curved-mirror cavity

The all-curved-mirror (ACM) cavity consists of four identical focusing mirrors with radius of curvature R . They are arranged in a symmetrical way as depicted in Fig. 3.1b.

Towards the outer stability edge at $d = 2R$ it exhibits four tight foci, of which two are crossing each other in the centre of the resonator. For small angles of incidence the round-trip length is approximately $4d$. When operated at this stability edge, the resonator length is solely given by the mirror's radius of curvature, or, in turn, a given repetition rate of the seeding laser determines the focusing.

There are four strongly focused arms at the outer stability edge with $A + D = +2$. Thus, the round-trip Gouy-phase is 4π . This is again consistent with Eq. (2.19). From Eq. (2.22) it is immediately clear, that the position and the angle of the optical axis due to misalignment diverges at this stability edge, as the denominator approaches zero. This is a common property of all resonators with round-trip Gouy-phase $2\pi N$, $N \in \mathbb{N}$.

The two crossing foci in the ACM allow for non-collinear geometries of frequency conversion processes, so that the generated radiation might be coupled out between two cavity mirrors without the need of any other output coupling devices. This will be discussed in Section 3.3.

3.2.3 Further designs

The SBT and ACM cavities can be used as building blocks for more complicated cavity designs. In order to have equal beam sizes on all cavity mirrors, the resonator should typically be operated close to a stability edge. Then, it can often be dissected into collimated arms with Gouy-shift 0 and strongly focused arms with Gouy-shift π . As the alignment sensitivity diverges at a stability edge with $A + D = +2$ or round-trip Gouy phase $2\pi N$, $N \in \mathbb{N}$, there should be an odd number of strongly focused arms.

If two intersecting foci as in the ACM cavity are required, the ACM can be altered in order to circumvent the diverging alignment sensitivity. For example, by exchanging two opposing mirrors with radius of curvature R with two mirrors with radius of curvature $2R$, the beam would not be focused a fourth time, but it would be collimated in one arm, see Fig. 3.2. This cavity has three strongly focused arms, so that the alignment sensitivity does not diverge at the stability edge. The length of the collimated arm can be increased and folded via flat mirrors, so that the cavity length and the focusing geometry can be adjusted independently. The cavity should be set up such, that two pulses traverse the overlapping focus at the same time.

3.3 Application-specific requirements

3.3.1 High-harmonic generation

For high-harmonic generation, the peak intensity is limited due to an ionization-induced phase shift in the gas target to about 10^{14} W/cm² depending on the gas species [61, 63]. In order to efficiently drive high-harmonic generation, the enhancement factor of the

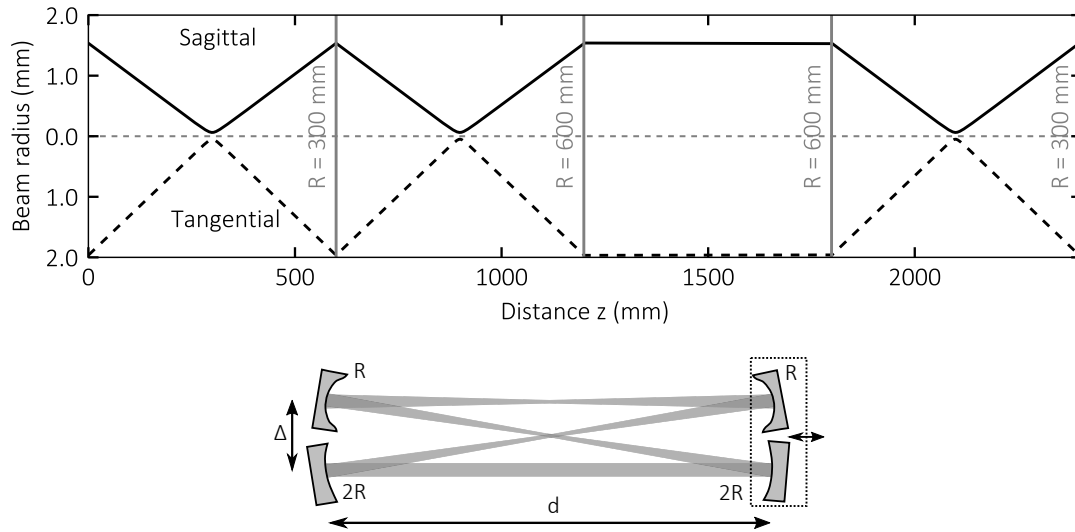


Figure 3.2 – The beam profile of the eigenmode along the optical axis (caustic) for an alternative cavity design with two crossing foci. The design is similar to an ACM, however, there are only three focused arm rendering this design robust against misalignment.

cavity is typically on the order of 100 – 200 [81, 82]. This will also be discussed in Section 5.1. Thus, the intracavity power is limited to the 10-kW level, as the available seed power is limited to the 100-W level due to thermo-optical effects. The focus size should be such, that the clamping intensity is not exceeded at the desired enhancement factor. Thus, loose focusing is typically used and the cavity does not have to be operated very close to the stability edge. Then, astigmatic compensation is not required.

In an empty cavity, the pulse parameters required for high-harmonic generation can be obtained with moderate effort. However, in order to separate the the generated XUV radiation from the driving laser light with low losses, an output coupler has to be integrated into the cavity. Often, the output coupler constitutes the weak point of the setup. For photon energies up to 20 eV, record flux from enhancement cavities has been obtained using thin plates put under Brewster’s angle subsequent to the gas target [81]. However, such a Brewster-plate adds dispersion to the cavity, absorbs light and therefore acts as a thermal lens [74], and it is prone to damage [81]. For higher photon energies, where shorter pulses and higher intensities are required, transmissive elements should be avoided in most cases. Using a nanograting [83, 84], comparable photon flux to these record values was achieved in Ref. [24]. The nanograting has to be put under grazing incidence subsequent to the cavity focus, so that the illuminated area on the grating is increased by a factor of $\arccos(\beta_{AOI})^{-1}$. Thus, a cavity design similar to the bow-tie cavity can be used. The nanograting does not add more dispersion than the underlying dielectric mirror. However, it was found that it is susceptible to contamination of

hydrocarbons resulting in an enhancement reduction [85]. Provided that this can be avoided by a clean vacuum and/or ozone purging, the nanograting is a good output coupling choice for applications where the spatial separation of the wavelength can be tolerated or is even advantageous.

Another technique is the so-called geometric output-coupling. For example, a small opening in the focusing mirror subsequent to the cavity focus can let some portion of the generated XUV radiation pass, while exhibiting moderate losses of about 0.5% [86]. Using this output coupler, photon energies exceeding 100 eV have been demonstrated from enhancement cavities. However, the damage threshold of such a pierced mirror is significantly lower than that of a standard mirror [87]. An alternative is non-collinear high-harmonic generation [88]. Here, two crossing foci as in the ACM or the alternative design from Fig. 3.2 are required. Then, the generated radiation can pass between the two side-by-side focusing mirrors, so that no other optical elements than standard dielectric mirrors are required. So far, this has not been demonstrated in enhancement cavities. In a single pass geometry, it can even be used as a gating method for the generation of isolated attosecond pulses [89] provided that the driving pulses are short enough. A related concept is quasi-imaging [77–79], where the cavity is operated at a point where several Gaussian-Hermite modes are degenerate. Then, tailored driving fields can be created, that have an on-axis maximum close to the focus, but no intensity on the subsequent focusing mirror, which can have a large opening for output coupling. It can be understood as non-collinear HHG with very small crossing angles and inherent synchronization between the two pulses. However, the cavity has to be operated at the center of the stability zone, where the beam size on the mirrors is smaller compared to the stability edge. On the other hand, the intensity at the mirror opening is smaller compared to the pierced mirror technique.

3.3.2 Thomson scattering

Hard x-rays can be generated by head-on scattering of photons in the NIR or visible range from relativistic electrons, a process called Thomson or inverse-Compton scattering [37]. Using this scheme, photon energies of several keV can be generated even with compact electron accelerators [38–40]. As this is a linear scattering process, the number of generated x-ray photons is proportional to the number of NIR photons interacting with the electrons, i.e. proportional to the peak intensity and the average power [37]. The pulse durations of both pulses should be matched and short enough, so that the interaction only takes place in the vicinity of the focus at high intensity. For example, if the electron beam can be focused to about 30 μm in radius, the laser beam of the same size has a Rayleigh-length of about 3 mm. Together with the speed of light $c = 0.3 \mu\text{m}/\text{fs}$, it follows, that both pulses should be shorter than 10 ps.

The pulse duration and focus radius is limited by that of the electrons. Typically,

durations in the picosecond-range and focus radii of several 10s of micrometer are achievable. The laser parameters should be chosen accordingly. With these boundary conditions, average powers on the order of 1 MW and an intensity exceeding 10^{15} W/cm² [40, 90] are desired. Due to these very demanding parameters, both intensity induced damage and thermal effects in the mirrors have to be considered. In general, a bow-tie resonator with astigmatic compensation (see Section 3.5) and measures against thermal lenses (see Chapter 4) can be employed.

The geometry for Thomson scattering can either be with or without an angle between the electron and laser beam. For a strict head-on geometry (no angle), one arm of an electron storage ring has to be put into the enhancement cavity [38], which implies a large distance between the focusing mirrors, i.e. loose focusing. Typically such a geometry will result in large angles of incidence, as the laser beam has to pass the bending magnets of the storage ring. Then, astigmatic compensation becomes indispensable. Output coupling in this geometry can be achieved using a back bored mirror [91]. However, it is prone to thermal deformation. If there is an angle between the propagation directions of the electron bunch and the laser pulse, the luminosity may drop for long pulse durations [92]. However, the achievable x-ray photon energy is not significantly affected by a small angle. Even in a 90°-configuration, the backscattered photon energy is still half of that generated in the head-on geometry.

Thus, from a cavity point-of-view the configuration with an angle is preferable, because it dictates less restrictions for the cavity design. In particular, tighter focusing and smaller angles of incidence are possible. However, for the whole system, also the electron accelerator and the synchronization between laser pulses and electron bunches have to be considered. More details can be found in Ref. [92].

3.3.3 Stack-and-dump

Another application requiring high-power enhancement cavities is a technique called stack-and-dump [93–95]. Here, pulses from a high-repetition rate (> MHz) amplifier are coupled into the cavity and then coupled out using a switch before/right after the build-up is finished. Thus, in contrast to HHG and Thomson scattering, the cavity is not operated in the steady state. The reason to implement this, is the fact that the achievable pulse energy from some laser amplifiers is limited by nonlinear effects, in particular for fibre amplifiers [96]. On the other hand, very high average powers can be obtained from fibres [97], so that they are best operated at high repetition rates. Using the stack-and-dump approach, several pulses can be stacked, so that the high repetition rate can be turned into a high pulse energy at still high average power levels.

The concept was first demonstrated using an acousto-optical-modulator [93]. However, any transmissive element constitutes a restriction for the cavity design in terms of damage and thermal effects. Ideally, only reflective optics should be employed, for

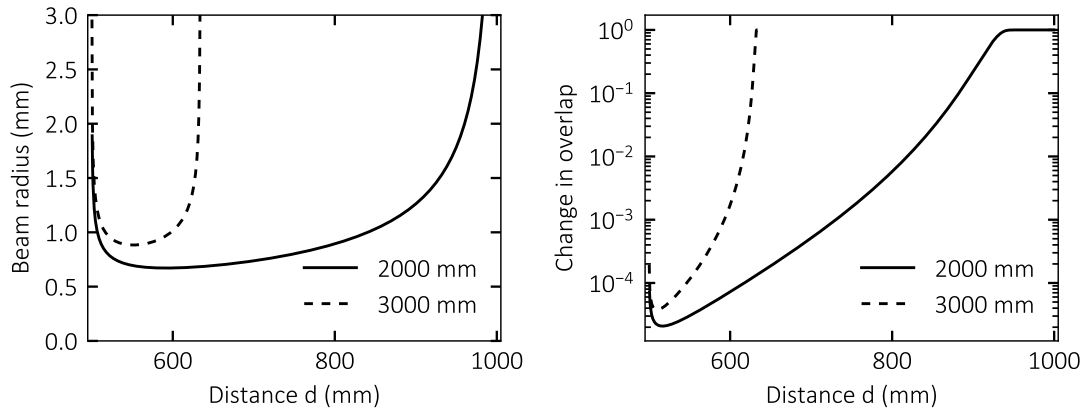


Figure 3.3 – (Left panel) Beam radius of a SBT with $R = 500$ mm and cavity length 2000 mm and 3000 mm. In the longer cavity, the beam size is larger for every point in the stability zone. (Right panel) However, the misalignment sensitivity is also increased in the longer cavity.

example a spinning wheel reflecting every N -th pulse out of the resonator [94]. As no high intensity is required in the cavity, the pulses can be stretched to circumvent intensity-induced mirror damage. However, very high average powers exceeding the MW-level are targeted [94]. As the dumping frequency is in the kHz-range, there will be no thermal steady state, but the cavity eigenmode will change within one dumping period. The cavity should be robust against thermal effects, as will be discussed in Chapter 4.

3.4 Misalignment sensitivity

3.4.1 Introduction

As discussed in the previous sections, for many applications enhancement cavities should be operated close to the stability edge with $A + D = -2$ in order to obtain large beams on all optics. While the alignment sensitivity diverges at $A + D = +2$, it is not immediately obvious for $A + D = -2$ from Eq. (2.22). Here, the alignment sensitivity of resonators with large spot sizes is investigated here.

In order to quantify the impact of misalignment in a resonator, the application of the resonator must be taken into account. For example, the output power of lasers fluctuate when the overlap between the resonator eigenmode and the pumped region in a laser crystal changes [98]. Also diffraction losses can increase [99]. For enhancement cavities, however, light from an external laser is coherently coupled into an empty resonator. Thus, the overlap between the incoming and the circulating beam determines how much power can be injected into the resonator. The situation is similar to the

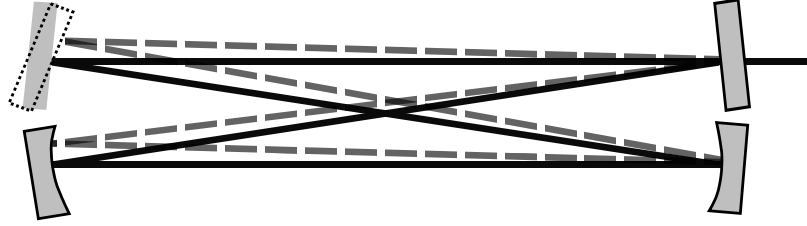


Figure 3.4 – Optical axis before (red) and after (blue) the upper left mirror is tilted.

coupling of laser light into an optical fiber. In both cases the the following aspects have to be considered for mode-matching: (a) The transverse beam shape – both size and divergence, and (b) the relative orientation of incident beam and the optical axis of the fiber or resonator – both offset and tilt. The mode matching determines how much power is coupled into the different (higher-order) modes of the fiber or resonator. In practise, power coupling factors of about 70%-90% into the fundamental mode (TEM_{00}) can be achieved. For enhancement cavities, in general this mode is non-degenerate with the higher-order Gauss-Hermite modes. When the cavity is operated with the fundamental mode, the power coupled into this mode is enhanced by the power enhancement factor \mathcal{E}_0 from Eq. (2.26), typically with $\mathcal{E}_0 \gg 100$, while the power coupled into the higher modes is attenuated in the cavity, as they not resonant, and can therefore be neglected. Thus, the spatial overlap between the incident laser beam and the cavity's fundamental eigenmode is crucial for an efficient operation of enhancement cavities.

The cavity eigenmode depends on both longitudinal and transverse alignment of the cavity: When the cavity optics are moved on the optical axis (longitudinal change), the eigen-q-parameter changes according to Eq. (2.16). When the cavity mirrors are tilted or internal transmissive elements are moved (transverse change), the position of the optical axis changes. Both effects can be modelled using the 3×3 -matrix formalism, that was introduced in Section 2.2.2. Note that these changes will in general lead to a dynamic response of the resonator, i.e. the resonator will need some short time to reach a new equilibrium after the change occurred. In the following, only the equilibrium states before and after a change is considered. Thus, the following considerations are valid for single, slow changes, such as manual alignment of the cavity, but not for fast and continuous changes, such as vibrations.

In order to quantify the impact of the alignment of cavities, the overlap U between the eigenmode before Ψ_{initial} and after a certain change $\Psi_{\text{perturbed}}$ is introduced as a metric here. For this metric, only two cavity eigenmodes are required. Physically, it can be interpreted as a situation where the overlap between the incident beam and the cavity mode is 1 before the perturbation. The change in overlap $1 - U$ is a measure for the sensitivity of the cavity toward this perturbation. When the change in overlap $1 - U$ is

large, the cavity is sensitive

Definition: Alignment sensitivity

$$U = \left| \int_{-\infty}^{\infty} \Psi_{\text{initial}} \Psi_{\text{perturbed}}^* dA \right|^2. \quad (3.3)$$

This metric maps any combination of misalignment to a single, physically meaningful number. The overlap between two beams does not change upon propagation through aberration-free optical systems. Thus, this metric can be evaluated anywhere in the resonators and depends only on the resonator geometry and on the considered perturbation.

In order to evaluate this metric, one first has to calculate the eigenmode of the unperturbed resonator. Then, the impact of the perturbation is calculated for both the lateral and longitudinal effect, e.g. using the 3×3 -matrix formalism. If both beams have a Gaussian shape, their respective q-parameters can be plugged into Eq. (2.3). Any lateral perturbations can be considered by [100]

$$\Psi_{\text{perturbed}}(x, y) = \Psi_{\text{initial}}(x - x_0, y) \exp(ik\alpha_0 x) \quad (3.4)$$

with the optical axis of the perturbed resonator described by x_0 and α_0 from Eq. (2.22). Alternatively, this metric can also be used without 3×3 -matrices, but with geometrical analysis [101] or numerical wave propagation [102] of the resonator.

As an example, one can study the impact of tilting one cavity mirror in a bow-tie resonator. Note that this is a pure transverse perturbation, i.e. the eigen-q-parameter does not change. For focusing mirrors with radius of curvature R , a round-trip length L and with a tilt of the first mirror by an angle $\Delta\alpha$, the round-trip matrix reads

$$\begin{pmatrix} 1 & d/2 & 0 \\ 0 & 1 & 0 \\ 0 & 0 & 1 \end{pmatrix} \cdot \begin{pmatrix} 1 & 0 & 0 \\ -2/R & 1 & \Delta\alpha \\ 0 & 0 & 1 \end{pmatrix} \cdot \begin{pmatrix} 1 & L-d & 0 \\ 0 & 1 & 0 \\ 0 & 0 & 1 \end{pmatrix} \cdot \begin{pmatrix} 1 & 0 & 0 \\ -2/R & 1 & 0 \\ 0 & 0 & 1 \end{pmatrix} \cdot \begin{pmatrix} 1 & d/2 & 0 \\ 0 & 1 & 0 \\ 0 & 0 & 1 \end{pmatrix} = \quad (3.5)$$

$$\begin{pmatrix} \frac{1}{R^2} (R^2 - 2Rd - 2(L-d)(R-d)) & \frac{1}{R^2} (LR^2 - 2LRd + Ld^2 + Rd^2 - d^3) & \Delta\alpha d \\ \frac{4}{R^2} (L - R - d) & \frac{1}{R^2} (R^2 + 2R(d-L) - 2d(d-L+R)) & 2\Delta\alpha \\ 0 & 0 & 1 \end{pmatrix}. \quad (3.6)$$

Here, the reference plane was chosen to be the focal plane in the focused arm. The

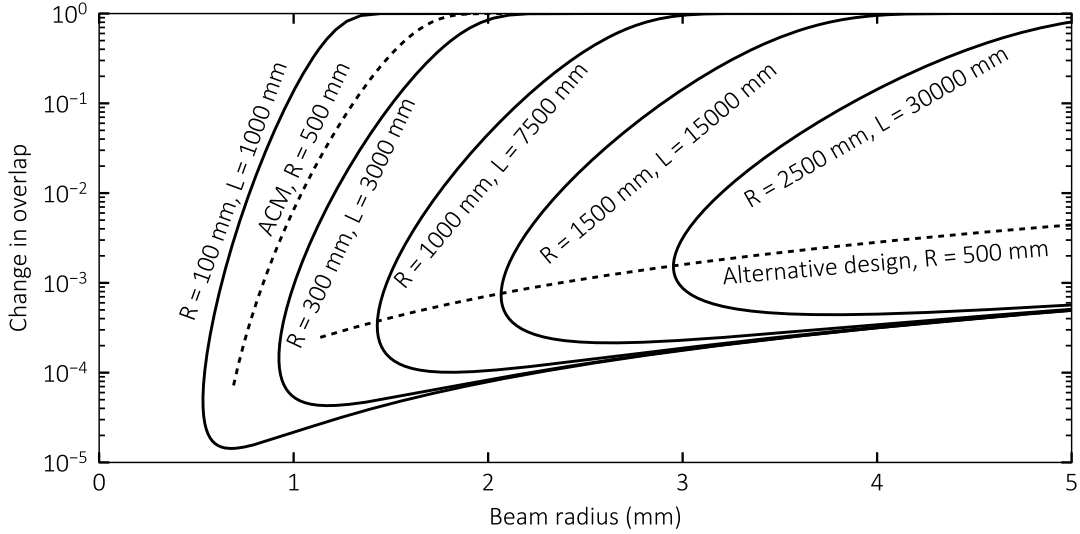


Figure 3.5 – The change in overlap for a tilt of $1 \mu\text{rad}$ of one mirror for several cavity designs as a function of the beam radius on that mirror. Solid lines represent standard-bow-tie cavities. Their sensitivity converges towards the inner stability edge (lower branch). Towards the outer edge, the sensitivity increases drastically, as the position of the optical axis diverges here. The same is true for the ACM (red dashed line). If two crossing foci are required, an alternative design should be used (blue dashed line), as discussed in the text.

eigenvector with eigenvalue 1 determines the optical axis of the perturbed cavity:

$$x_0 = R\alpha/2 \quad (3.7)$$

$$\alpha_0 = \frac{R\alpha(L-d)}{d^2 + L(R-d)} \quad (3.8)$$

Together with Eq. (3.4) and Eq. (3.3), the alignment sensitivity can be evaluated.

3.4.2 Comparison of cavity designs

In Fig. 3.3, the beam radius on the curved mirrors is plotted for the entire stability range for two bow-tie cavities with identical focusing, but with different lengths. In the right panel, the alignment sensitivity from Eq. (3.3) is plotted for a tilt of one of the curved mirrors of $1 \mu\text{rad}$. For kinematic mirror mounts for 25-mm optics, this corresponds to a position change of about 25 nm, which is about the smallest possible adjustment step with available motorized optomechanics. One can see that for the longer cavity the beam radius is larger for every point in the stability range, but so is the alignment sensitivity. As expected from Eq. (2.22), the alignment sensitivity diverges towards the outer stability edge. Even a small tilt of only $1 \mu\text{rad}$ can change the overlap by several

percent rendering the operation at this stability edge impractical. The sensitivity also increases towards the inner edge, but not as severely as towards the outer one.

In order to compare various cavity designs, the alignment sensitivity is plotted as a function of the beam radius on the curved mirrors in Fig. 3.5. In this parametric plot, the upper branch for a bow-tie cavity corresponds to the outer edge, and the lower branch to the inner edge. This depiction reveals that towards the inner edge the alignment sensitivity of all bow-tie cavities converges, i.e. it is only a function of the beam radius, but does not depend on the focusing geometry or the cavity length. More importantly, the increase is moderate. Even for very large beam radii of about 5 mm the overlap only changes by less than a per mill. Thus, large beam radii necessary for high-power enhancement cavities can be obtained with bow-tie cavities, either in long cavities or even in compact setups when operated very close to the inner stability edge.

For pulsed enhancement cavities, the cavity length has to be matched to the repetition rate of the seeding laser, i.e. $L_0 = c/f_{\text{rep}}$ for ring resonators. However, the cavity length can also be an integer multiple of L_0 , so that multiple pulses are circulating in the cavity. As discussed in Section 2.3.2, the resonance linewidth of longer cavities is narrowed, so that the demands on the frequency stability of the seeding laser are higher. Besides that, the choice of the cavity length depends also on other factors such as astigmatism (see Section 3.5) and thermal sensitivity (see Chapter 4). In the following experiments, the enhancement cavity length was doubled in comparison to the laser's cavity length, as this allows for a smaller angle of incidence for astigmatic mitigation. In Chapter 5 up to four pulses were circulating in the cavity, as then the thermally induced beam size increase is mitigated, as demonstrated in Chapter 4.

Towards the outer stability edge, i.e. for $A + D = +2$, the alignment sensitivity increases drastically for both the standard-bow-tie cavity and the all-curved-mirror cavity as expected from Eq. (2.22). As will be discussed in the next section, the sensitivity is too high for robust operation. If two crossing foci as in the ACM are required, a design should be chosen according to Fig. 3.2. This alternative cavity exhibits an alignment sensitivity, which is about one order of magnitude higher than the SBTs at the inner edge, which is still tolerable.

3.4.3 Experimental verification

For verification, two 125-MHz enhancement cavities with large spot sizes on all mirrors were implemented, namely an ACM with $R = 300$ mm at the outer stability edge and an SBT with $R = 600$ mm at the inner one. A single frequency non-planar ring oscillator (NPRO) [103] was locked using the Pound-Drever-Hall scheme [104, 105] to each of the cavities, see Fig. 3.6. The intracavity power P_{circ} was measured with a powermeter via the leakage through one high-reflective mirror with known transmission. The surface of one cavity mirror was imaged onto a CCD allowing for a measurement of the beam

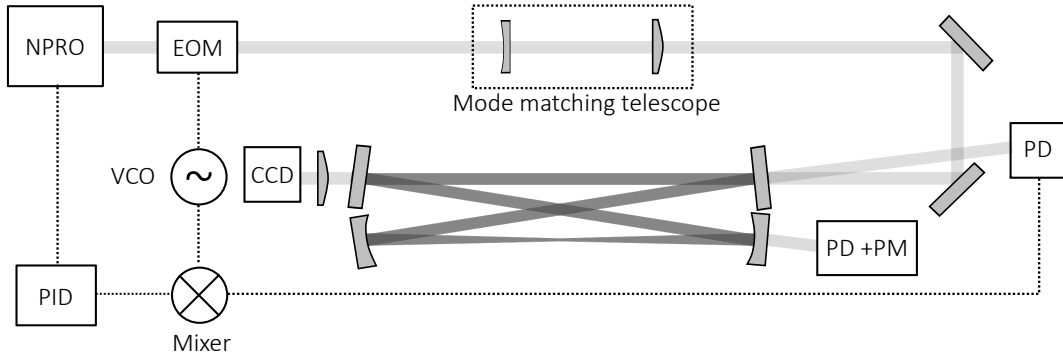


Figure 3.6 – Schematic of the experimental setup used to verify the alignment sensitivity. NPRO: non-planar ring oscillator, EOM: electro-optical-modulator, PD: photodiode, CCD: charge-coupled device, VCO: voltage-controlled oscillator, PM: power meter, PID: proportional-integral-differential controller.

size on that mirror. The magnification M can be calculated from the distance g between the cavity mirror and the imaging lens, and the distance b between that lens and the CCD, $M = b/g$. It is double-checked by a measurement of an obstacle directly in front of the mirror with known dimensions. From this, the position in the stability zone can be deduced according to Fig. 3.3. As the angles of incidence are known from a measurement of the distances Δ and d as defined in Fig. 3.1 for both cavities (1.24°), the beam ellipticity provides an independent measurement. One photodiode measured the transmission through a mirror for a quantification of power fluctuations in the cavity. Another photodiode measured the power level reflected from the input coupler. By comparing the levels in lock and off-resonance, the power fraction coupled into the cavity K can be calculated. The power enhancement \mathcal{E} is given by $P_{\text{circ}}/P_{\text{in}}$ with the incident power P_{in} . The power attenuation factor $A = a^2$ (see Eq. (2.28)) is given by $A = 1 - K/\mathcal{E}$. When the cavity attenuation is compared, changes of the overlap between the incident beam and the cavity eigenmode can be ruled out as a reason for changes of the power enhancement \mathcal{E} .

Both cavities were locked at several positions in the stability range. The mirror mounts were motorized, so that the mirrors can be tilted in steps of about $1 \mu\text{rad}$. In Fig. 3.7 the $1/e^2$ -intensity beam radius is plotted for both cavity planes. For the ACM, the beam radius is limited to $4.0 \text{ mm} \times 2.1 \text{ mm}$. Larger beams could not be obtained with satisfactory alignment, as the sensitivity of the ACM diverges at the outer stability edge. This behaviour is expected from Fig. 3.5, as even the very fine adjustment steps change the overlap by some 10s of percent. On the other hand, a spot size of $5.7 \text{ mm} \times 2.6 \text{ mm}$ was obtained in the SBT without affecting the round-trip attenuation. An even larger beam radius of more than 7 mm in the sagittal plane was achieved with slightly larger diffraction losses at the 25-mm mirrors. The alignment in this case was without problems as expected from the sensitivity metric.

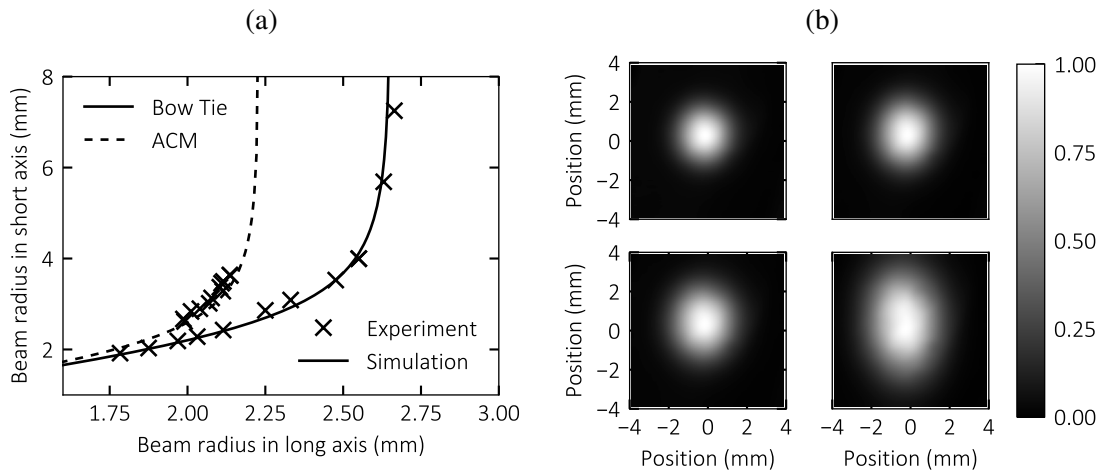


Figure 3.7 – (a) The measured beam radii in the long axis and short axis for a bow-tie cavity and for an all-curved mirror cavity. For the ACM, the achievable beam radius is limited by the alignment sensitivity. The solid line is a simulation based on the ABCD-matrix formalism. (b) Different modes from the bow-tie cavity measured with a CCD.

Power fluctuations in the cavity can arise from two sources: First, phase fluctuations between the laser and the cavity (see Eq. (2.29)), and second, changes of overlap between the incident beam and the cavity mode. During these experiments, the intracavity RMS noise did not increase when the cavities were operated closer to the stability edge and remained below 0.1% in the 20 Hz – 600 kHz band. Thus, when operated in an airtight environment, power fluctuations due to mirror vibrations are no limitation, even at a stability edge with diverging sensitivity. In fact, there is no necessity to operate an enhancement cavity close to a stability edge with diverging sensitivity, because alternative designs can be found. Then, the achievable beam size is limited by thermal effects and spherical aberrations as will be discussed in Chapter 4.

In principle, larger mirrors can be used if larger beam radii are required. Then, however, the angle of incidence must be increased, which results in a higher beam ellipticity. In order to increase the spot size also in the short axis, astigmatic compensation as discussed in Section 3.5 becomes more and more important. In Ref. [44], up to 18 kW of average power could be obtained with 200-fs pulses limited by intensity induced mirror damage. Compared to that setup, the beam area could be increased by more than a factor of 15 in the SBT. In terms of intensity damage, an average power of several 100s of kW seems feasible using this cavity design. Then, thermal effects in the cavity mirrors will occur. With appropriate measures, such average powers are still possible as will be demonstrated in Chapter 4.

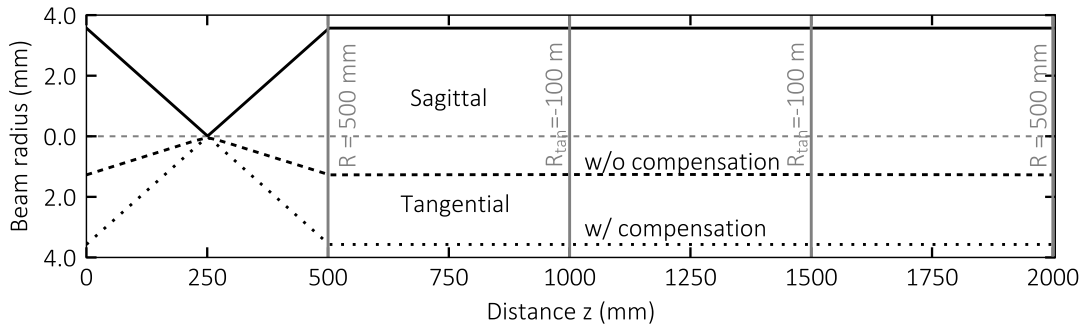


Figure 3.8 – Caustic of a 2-m long bow-tie cavity. The 500-mm curved mirrors are hit under an angle of 4° resulting in an elliptical beam shape (dashed line). Using two cylindrical mirrors with $R_{\text{tan}} = -100$ m as depicted, a round beam can be obtained.

3.5 Astigmatic compensation

3.5.1 In-plane compensation

Curved mirrors hit under an angle of incidence β_{AOI} exhibit effective radii of curvature of $R_{\text{sag}}^{\text{eff}} = R/\cos(\beta_{\text{AOI}})$ and $R_{\text{tan}}^{\text{eff}} = R \cdot \cos(\beta_{\text{AOI}})$. By proper choice of the angles of incidence and of the radii of curvature, this astigmatism can be turned into a pure ellipticity in a resonator, i.e. the position of the focus in the sagittal in tangential plane is the same. The most common example is a symmetric geometry with identical radii of curvature and identical angles of incidence as in the standard bow-tie cavity or in the all-curved-mirror cavity. Here, the ellipticity diverges towards the stability edges, as shown in Fig. 3.7a.

Without the astigmatism, the beam would be large in both planes, resulting in a significantly lower intensity on the cavity optics. Thus, astigmatic compensation is highly desirable, in particular for cavities with loose focusing operated very close to a stability edge. In laser resonators, this has been done using the astigmatism of the laser crystal [106]. However, for high-power enhancement cavities, an implementation without any transmissive elements is desired. The astigmatism can be compensated using cylindrical or toroidal mirrors. For example, a toroidal mirror with radii of curvature $R_{\text{tan}}^{\text{real}} = R/\cos(\beta_{\text{AOI}})$ and $R_{\text{sag}}^{\text{real}} = R \cdot \cos(\beta_{\text{AOI}})$ exhibits identical effective radii of curvature for a specific β_{AOI} resulting in a completely astigmatism-free cavity. Alternately, two plane mirrors in a bow-tie cavity can be replaced by two cylindrical mirrors of proper curvature. This should be implemented in a symmetrical way with respect to the focus plane, so that the cavity is astigmatism-free.

In Fig. 3.8, the caustic of a 2-m long bow-tie cavity with $R = 500$ mm curved mirror and an angle of incidence of 4° is plotted. Without astigmatic compensation, the beam size in this example is $3.6 \text{ mm} \times 1.3 \text{ mm}$. Using two -100-m cylindrical mirrors, the

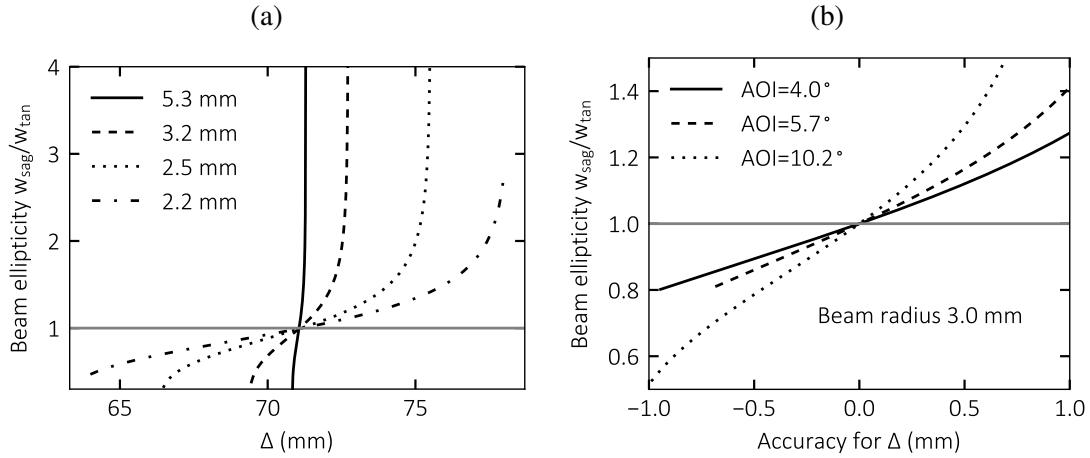


Figure 3.9 – (a) The beam ellipticity of the cavity depicted in Fig. 3.8 as a function of Δ as defined in Fig. 3.1a. When larger beams are desired, a better accuracy is required. (b) For larger angles of incidence, also a better accuracy for Δ is required.

beam radius can also be increased in the tangential plane, resulting in a almost three times larger beam area. In practise, the angle of incidence has to be fine-tuned in order to achieve a round beam profile. In Fig. 3.9a, the beam ellipticity is plotted as a function of Δ as defined in Fig. 3.1a, i.e. as a function of the angle of incidence. This figure reveals, that the required accuracy for the angle of incidence depends on how close the cavity is operated to the stability edge. Eventually, this will be the limitation for the achievable beam size. On the other hand, the required accuracy is not significantly increased even for large angles of incidence, as can be seen in Fig. 3.9b.

3.5.2 Non-planar cavities

Another possibility for astigmatic compensation are non-planar cavities. For instance, in a bow-tie cavity one of the curved mirrors could reflect the beam out of the plane with the same angle of incidence as for the other mirror. However, depending on how the cavity is closed, the intracavity light will see a polarisation rotation of an angle ρ . The incident field can be described by a Jones-vector $\mathbf{E}_{\text{in}} = (E_s, E_p)^T$ with vector components describing the p- and s-polarisation. The polarisation rotation can be taken into account using a rotation matrix \mathbb{R}_ρ . The steady-state equation similar to Eq. (2.24) for the circulating field \mathbf{E}_{circ} then reads

$$t \cdot \mathbf{E}_{\text{in}} + \mathbb{M}_{\text{RT}} \cdot \mathbf{E}_{\text{circ}} = \mathbf{E}_{\text{circ}}, \quad (3.9)$$

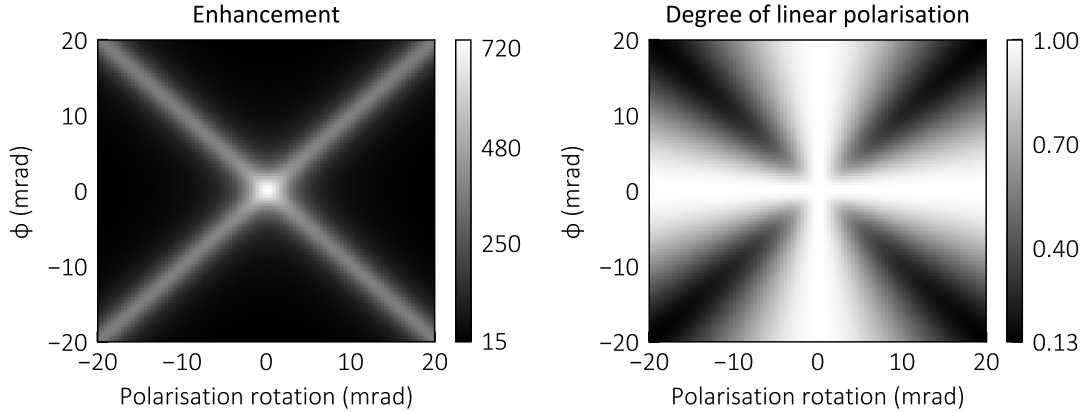


Figure 3.10 – (Left panel) The enhancement of an example cavity (see text) with linear input polarisation for a range of rotation angles (corresponding to -1° to $+1^\circ$) and round-trip phases. (Right panel) The degree of linear polarisation for the same range.

with the round-trip matrix $\mathbb{M}_{\text{RT}} = a \cdot r \cdot \exp(i\phi) \cdot \mathbb{R}_\rho$. The circulating field is then given by

$$\mathbf{E}_{\text{circ}} = (\mathbb{1} - \mathbb{M}_{\text{RT}})^{-1} \cdot t \cdot \mathbf{E}_{\text{in}}. \quad (3.10)$$

This equation was solved for an example cavity with $R = 99.5\%$ and 200 ppm losses and linear input polarisation, see Fig. 3.10. Without polarisation rotation, the enhancement is about 720 for $\phi = 0$ as expected from the scalar treatment. In the presence of a small rotation, the enhancement drops and occurs for $\phi = \rho$. Then, the degree of linear polarisation the in cavity is only about 13%, as the intracavity polarisation is elliptical (right-hand panel). Thus, if linear polarisation is required, the cavity must be built such that the round-trip polarisation rotation is a multiple of π . On the other hand, if circular polarisation is desired, the maximum enhancement can be obtained for any polarisation rotation for $\phi = \rho$. Another interesting special case is $\rho = \pi/2$ and linear input polarisation: Here, for $\phi = \pm\pi/2$, half of the maximum enhancement can be achieved and the intracavity polarisation is circular with the handedness depending on the sign of ϕ .

3.6 Conclusions

In this chapter, design guidelines for ultrashort pulse enhancement cavities are given. The achievable intensity and power levels are limited by intensity-induced mirror damage. This can be circumvented by increasing the beam size on all cavity optics. Then, the robustness against maladjustment is of utmost importance. Here, a new metric for the quantification of the misalignment sensitivity is introduced. With it, different

cavity designs were evaluated. An important outcome of this analysis is, that resonators operated close to the stability edge with $A + D = -2$ are robust against misalignment. In particular, the bow-tie resonator close to the inner stability edge fulfils all design goals for frequency conversion processes requiring a tight focus, for example high-harmonic generation and Thomson-scattering. On the other hand, resonators operated at the other stability-edge at $A + D = +2$, e.g. the ACM cavity, are too alignment sensitive for robust operation and can thus be ruled out for the experiments described in the next chapters. If two foci are required, an adapted design, which is also robust against misalignment, can be implemented, as was shown in Fig. 3.2. However, for the experiments demonstrated in this thesis, two crossing foci are not required, so that this cavity design will not be pursued any further.

Experimentally, an enhancement cavity based on the bow-tie design with large spot sizes on all optics was demonstrated. This cavity design will be used to explore the MW-level average power regime with ultrashort pulse enhancement cavities in the next chapter. When operated close to a stability edge, even a small astigmatism manifests as a considerable beam ellipticity. This can be compensated for by employing cylindrical mirrors in conjunction with standard spherical mirrors.

CHAPTER 4

Megawatt-level average power enhancement cavities for ultrashort pulses

In this chapter, thermal effects and their mitigation in enhancement cavities are discussed. It starts with an introduction in Section 4.1 on how thermal lenses affect the operation of enhancement cavities. In Section 4.2, a measure for the thermal sensitivity and a model for its calculation of arbitrary cavities will be introduced. Possibilities for mitigation of thermal effects using custom optics are reviewed in Section 4.3. Using the apparatus presented in Section 4.4, experiments targeting the power scaling of enhancement cavities were conducted, which are described in Section 4.5. The achievable power level in these experiments is limited by aberrations, which are examined in Section 4.6. The chapter is based on [43].

4.1 Introduction

In enhancement cavities, some light is inevitably absorbed by the mirror's coatings, leading to a thermal gradient and to a deformation of the substrate. As discussed in Section 2.4.1, a deformed mirror acts as a defocusing lens in reflection. In a bow tie resonator close to the inner stability edge, a defocusing lens results in an increased beam size, which in turn decreases the thermal focusing power, as the heat is now deposited

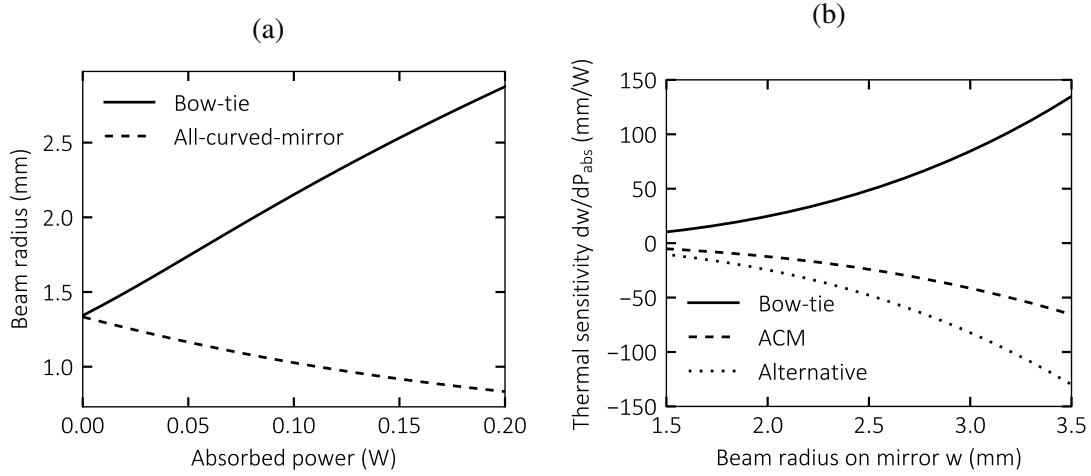


Figure 4.1 – (a) The change in beam size due to thermal deformation of the cavity mirrors. Bow-tie: $L = 2$ m, $R = 500$ mm, $d = 503$ mm. All-curved-mirror: $L = 2$ m, $R = 250$ mm, $d = 499$ mm. (b) The thermal sensitivity dw/dP_{abs} for various cavities as a function of the beam radius on the curved mirrors. All cavities are 2-m long and have a mirror separation of $d \approx 500$ mm, so that their focusing geometry is comparable.

in a larger area. Thus, the beam size increases until a new steady state is reached, where the thermal lens is in equilibrium.

An immediate consequence of this is that the increase (or decrease for other cavity designs) of the beam size depends on how the resonator responds to a defocusing lens. This thermal sensitivity of enhancement resonators will be discussed quantitatively in the next section. The thermal sensitivity also depends on the cavity mirrors, in particular on the coating absorption and on the thermal properties of the substrate, see Section 4.3. The treatment of thermal effects here will be restricted to cavities with purely reflective optics. It can be, however, extended to transmissive optics [74].

4.2 Quantitative model for the thermal sensitivity

4.2.1 Calculation of the steady state

Consider a resonator with N elements, that are affected by thermal effects. The focal length of the i -th element is given by $f_{total,i}^{-1} = f_{0,i}^{-1} + f_{thermal}^{-1}$, with the cold focal length f_0 and the thermal focus length $f_{thermal}$, e.g. calculated from Eq. (2.49). Note that f_0 and $f_{thermal}$ can have different signs. The beam size on that element is referred to as $w_i(\mathbf{f}_{total})$ and depends, among other things such as mirror separation, on all focal lengths, $\mathbf{f}_{total} = (f_{total,1}, f_{total,2}, \dots, f_{total,N})$. In the steady-state, these beam radii must be

in equilibrium with

$$w_{\text{th}}(f_{\text{th}}) = \sqrt{-\gamma f_{\text{th}} \frac{\alpha}{\kappa} P_{\text{abs}}}, \quad (4.1)$$

which is Eq. (2.49) solved for w . Mathematically, the steady-state is reached, when the difference in beam size between w_i and $w_{\text{th},i}$ vanishes:

$$w_i(\mathbf{f}_{\text{total}}) - w_{\text{th},i}(f_{\text{thermal},i}) = 0 \quad \forall \quad i = 1 \dots N \quad (4.2)$$

The solution of this set of coupled nonlinear equations yields a unique vector of thermal focusing lengths $\mathbf{f}_{\text{th}} = (f_{\text{th},1}, f_{\text{th},2}, \dots, f_{\text{th},N})$. With it, the eigenmode of the cavity can be calculated in the thermal steady state using the ABCD-formalism. The solutions are best found using numerical root finding algorithms for vector functions or by minimizing the sum of the squares of Eq. (4.2) [107]. Using this model, arbitrary cavity designs may be evaluated with different optical properties of the individual cavity optics. The model can be readily extended to include transmissive optical elements, when their thermally induced changes of the focal length can be calculated [74].

In Fig. 4.1a, the beam radius on the curved mirrors of a bow-tie cavity and an all-curved-mirror cavity is displayed as a function of the absorbed power. Each cavity consists of four fused silica mirrors and is operated close to a stability edge, where the beam radius is large on all optics. The deformation of the mirrors results in an increased focal length. Thus, the bow-tie cavity is pushed towards the stability edge at $d > R$, so that the beam radius increases. On the other hand, the all-curved-mirror cavity is pulled away from the stability edge at $d < 2 \cdot R$. Then, the beam radius decreases.

4.2.2 Thermal sensitivity

For small powers, the change in beam size is linear in good approximation. Thus, a good measure for the thermal sensitivity is the derivative of the beam radius with respect to the absorbed power,

Definition: Thermal sensitivity

$$S_{\text{thermal}} = \left. \frac{dw}{dP_{\text{abs}}} \right|_{P_{\text{abs}}=0} \quad (4.3)$$

The sensitivity is given for a certain position in the resonator, i.e. the position must be specified together with the sensitivity. As here only symmetric cavities with nearly identical spot sizes on all mirrors are considered, the beam radius on the curved mirrors is used. However, if asymmetric focusing or cavities operated far from a stability edge are considered, one must be cautious when comparing different cavities.

In an experiment, the beam radius can easily be measured as a function of the circu-

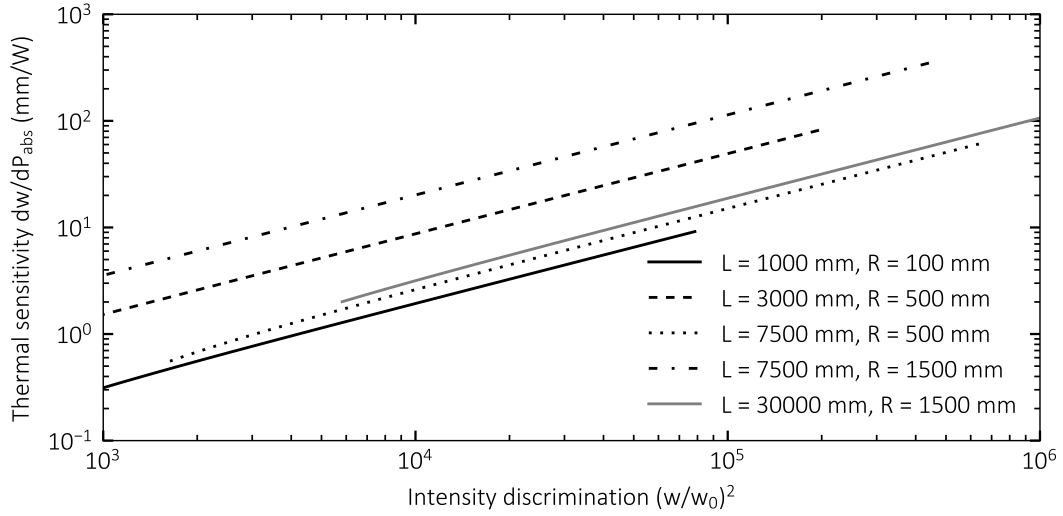


Figure 4.2 – The thermal sensitivity dw/dP_{abs} of several bow-tie cavities over their entire stability range. The lower branch (negative sensitivity) corresponds to the outer stability edge, the upper one to the inner edge.

lating power. Then, the thermal sensitivity can also be defined as dw/dP_{circ} . This relates to the previous definition via the coating absorption factor a_{coating} :

$$\frac{dw}{dP_{\text{abs}}} = a_{\text{coating}}^{-1} \cdot \frac{dw}{dP_{\text{circ}}}. \quad (4.4)$$

The experimental thermal sensitivity can be fitted to the calculated one with the coating absorption as the only free parameter. Thus, the increase in beam size can be used for a measurement of the coating absorption, provided that all mirrors exhibit the same absorption or that only one mirror dominates thermal lensing. Alternatively, the sensitivity can be measured before and after one mirror is replaced allowing for an absorption measurement of that mirror. The absolute precision depends on how well the absolute focal length of a deformed mirror can be obtained from simulations, or may be taken from an experimental calibration with mirrors of known absorption.

In Fig. 4.1, the calculated thermal sensitivity is plotted for a bow-tie cavity, an all-curved mirror cavity and the alternative design, that were all discussed in the previous chapter. One can see, that the absolute value of the sensitivity increases for larger beam radii, i.e. closer to the stability edge. In order to explain this, two counteracting factors have to be considered: First, towards the stability edge, all cavities become more susceptible toward changes of the focusing geometry, i.e. a given thermal deformation has a stronger impact closer to the stability edge. On the other hand, the focusing power of the thermal lens for a given absorbed power is weaker closer to the stability edge,

as here the beam radius is larger. However, the first factor prevails, so that overall the thermal sensitivity increases.

In Fig. 4.2 the thermal sensitivity of various bow-tie geometries is compared as a function of the intensity discrimination $D = w_{\text{mirror}}^2/w_0^2$. The cavities for this plot are assumed to be free of astigmatism, e.g. by a proper compensation mechanism as discussed in Section 3.5. Both tight focusing and a long cavity length decrease the sensitivity. In principle, the maximum cavity length is only limited by practical considerations, i.e. by space requirements and robustness of the cavity lock due to the narrow resonance linewidth. The achievable intensity discrimination is limited by aberrations, see Section 4.6. For tight focusing, the angle of incidence is large resulting in significant astigmatism without compensation.

4.3 Power scaling with custom optics

Thermal effects in enhancement cavities can be mitigated using mirrors with superior thermal properties. According to Eq. (2.49) the thermal properties of the substrate (coefficient of thermal expansion α , thermal conductivity κ) and the absorption coefficient of the coating matter determine the thermal performance of a cavity mirror.

4.3.1 Substrate materials

At first glance, only the ratio α/κ is important for the material choice of the substrate. Table 4.1 summarises this property relative to fused silica for common substrate materials. There are basically two types of available materials, which improve this quantity: Crystalline substrates due to their high thermal conductivity and low expansion glasses/ceramics. The latter include "ULE" from Corning, "Clearceram-Z" from Ohara and "Zerodur" from Schott. The table gives the specified "better than" values for the thermal properties of these materials. In general, these three perform similarly. While ULE is a transparent glass, which can be used in transmission for low-power applications, both Zerodur and Clearceram-Z are ceramics with a brownish color and therefore higher bulk absorption also in the near infrared. In the following, only ULE is considered, as it is readily available with very good surface quality almost as good as for fused silica. However, it cannot be used for the input coupler, as the bulk absorption is too high for the multi 100-W level. Note that the coefficient of thermal expansion can also become negative for these materials, which could be used to compensate for the defocusing lens of a mirror with positive expansion coefficient. This concept is related to work in Ref. [74], where a glass plate with positive thermal lensing was used for compensation. Compared to this, a mirror with negative expansion coefficient would behave just like a regular cavity mirror, i.e. it exhibits less dispersion than a thin plate and has low loss

Table 4.1 – Overview of important properties of substrate materials. α is the coefficient of thermal expansion, κ the thermal conductivity, α/κ is relative to fused silica. The rating for bulk transmission and surface quality is taken from the experience gained during the experiment described below. Only tested materials are rated.

Material	$ \alpha $ (10^{-6} K^{-1})	κ ($\text{W}/(\text{mK})$)	rel. α/κ	Bulk trans.	Surface Quality	Ref.
Fused silica	0.51	1.38	1	++	++	[108]
ULE	< 0.03	1.31	>16	○	+	[109]
Sapphire	5.8	42.0	2.7	+	○	[110]
Silicon	3.0	130.0	16	--	++	[111, 112]
CaF	18.9	9.7	0.2			[113]
YAG	7.0	23.0	1.2			[114]
Clearceram-Z	< 0.02	1.51	>28			[115]
Zerodur	< 0.02	1.46	>27			[116]
Diamond	1.0	1800	665			[117]

independent on the angle of incidence. Also, a thin plate easily deforms resulting in aberrations, which is not the case for the thick mirror.

Alternatives to these low-expansion materials are crystals with a significantly better thermal conductivity than fused silica. However, their coefficient of thermal expansion is also much higher, so that only a few materials such as sapphire or silicon constitute an improvement, while others such as YAG and CaF actually perform worse, see Table 4.1. In terms of α/κ , sapphire (Al_2O_3) is better by a factor of 2.5. Its bulk absorption is good enough for the use as an input coupler. However, being a very hard material, it is difficult to polish so that the surface quality is worse than that of fused silica, which results in a lower damage threshold. On the other hand, silicon is a non-transparent material with the highest thermal conductivity of all materials considered here. Here, all light transmitted through the coating is absorbed in the substrate, i.e. its effective coating absorption factor is the sum of the actual coating absorption and the coating transmission. As the transmission of dielectric mirrors can be very low (sub-ppm), it should still perform better than fused silica. However, in an evaluation experiment it exhibited a stronger thermal lens than fused silica for unknown reasons. Its use was therefore discarded. Compared to low-expansion materials, crystals will exhibit much lower peak temperatures in the steady-state as the heat is distributed more efficiently. Eventually, this will be an advantage if much power is absorbed in the coating, as the damage threshold may decrease at high temperature [118].

In conclusion, if the high peak temperatures can be tolerated, ULE constitutes the best substrate material for high-power enhancement cavities. However, it cannot be used for the input coupler, as the bulk absorption is too high. For this, sapphire or fused silica can be used. Sapphire performs better by a factor of 2.5 in terms of α/κ , but such mirrors have a lower damage threshold depending on the available surface quality. The thermal sensitivity of a four-mirror cavity (e.g. Fig. 4.2) can be decreased to a fourth, when all three high-reflective mirrors are replaced by ULE. Note that this is the same for all cavity designs, so that the relative sensitivities in Fig. 4.2 remain unchanged when the same amount of mirrors are changed.

4.3.2 Coating absorption

Here, only (quasi) quarter-wave stacks are considered as coating designs, as these exhibit almost zero dispersion for a certain bandwidth depending on the materials. The coatings consist of alternating layers of a high refractive index (high-n) and a low refractive index (low-n) material. The low-n material is typically SiO_2 . A high bandwidth – both for reflectivity and low dispersion – can be obtained with a large contrast $n_{\text{high}}/n_{\text{low}}$ [119]. However, a material with large refractive index in general exhibits a small bandgap [120] resulting in a low damage threshold.

The absorption of these is largely determined by the top 2 – 3 layers [121], as most

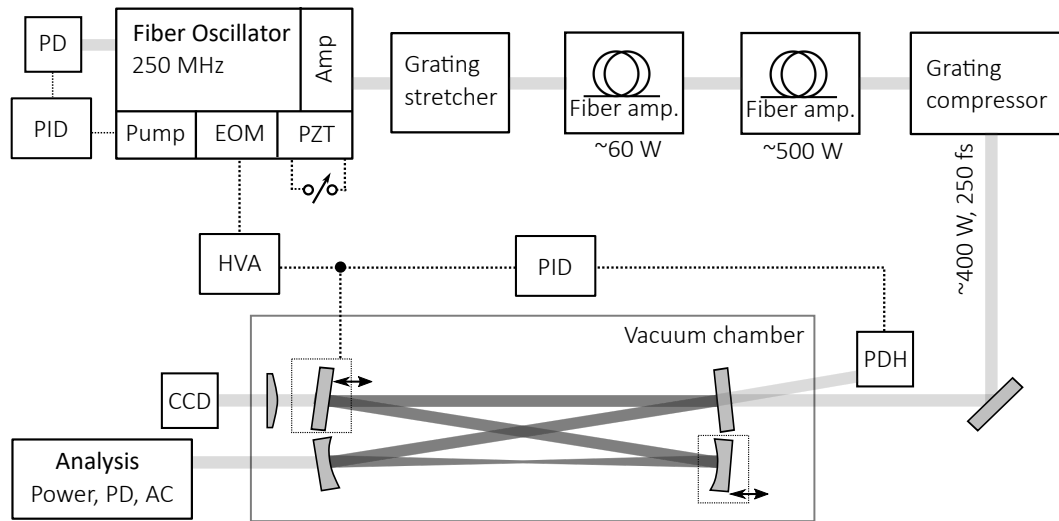


Figure 4.3 – Schematic of the experimental setup. See text for details. PD: photodiode, Amp: amplifier, PID: proportional-integral-differential controller, EOM: electro-optic modulator, PZT: piezo, PDH: Pound-Drever-Hall, HVA: high-voltage amplifier, AC: auto correlator, CCD: charged-coupled-device.

light is already reflected from these layers. Other designs such as chirped mirrors with a larger penetration depth exhibit a higher absorption. In these layers, the absorption is dominated by the high- n material. The lowest absorption can be reached with Ta_2O_5 . Then, the coating absorption can be as low as 1 ppm and the total losses of commercially available mirrors is only about 20 ppm¹. The use of SiO_2 – Ta_2O_5 coatings allows for the enhancement of sub-100-fs pulses at enhancement factors of about 200 [86]. Alternatively, Nb_2O_5 can be employed allowing for pulses as short as 25 fs [63], but at the expense of a four times higher absorption and of a lower damage threshold.

4.4 Experimental apparatus

In order to demonstrate the MW average power level in enhancement cavities with ultrashort pulses, a setup using a high-power fibre amplifier is used. The laser system is described in [122] and was built by the fibre laser group at the "Institute for Applied Physics" at the University of Jena. A schematic can be found in Fig. 4.3. The seeding laser is a commercial fibre oscillator (Menlo orange) with a first amplifier stage emitting stretched femtosecond pulses at 250 MHz repetition rate. The power in the broad spectrum (1005 – 1055 nm) is 2.5 W. It is equipped with three actuators for the oscillator

¹These values were reached using mirrors supplied by Layertec GmbH, Mellingen.

cavity length:

- An electro-optical modulator (EOM) for fast fluctuations (bandwidth >100 kHz), but with a small range of about $1\ \mu\text{m}$.
- A long range piezo with a smaller bandwidth (<10 kHz), but longer travel range of about $10\ \mu\text{m}$. This piezo also affects the carrier-to-envelope frequency f_0 . In the experiment it was used to manually control f_0 while the laser is locked to the cavity.
- A stepper motor for coarse adjustment of the repetition rate. This allows the repetition rate to be changed within a range of 249 MHz to 251 MHz, which would be necessary for designs such as the all-curved-mirror cavity, where the cavity length cannot be changed independent of the focusing geometry. However, for the following experiments it was not used.

The modelocking in this oscillator is achieved using nonlinear polarisation rotation implemented with four wave-plates. Thus, there are many modelocking states with vastly different phase noise properties. The phase noise is strongly coupled to the amplitude noise in such oscillators [123]. It was found, that optimizing the amplitude fluctuations when the laser is modelocked using the wave-plates yields good modelocking states that allow for a reliable and tight lock of the laser to the cavity. The noise-eater described in Ref. [123] was also implemented. While it allowed to improve the quality of the lock of bad modelocking states, its impact for optimized states was small.

The pre-amplified pulses are further stretched to about 900 ps in an all-reflective grating stretcher and then amplified. In the stretcher the spectrum centred at 1042 nm is cut to 18 nm. The first amplifier fiber has a cladding diameter of $170\ \mu\text{m}$, a core diameter of $40\ \mu\text{m}$, and has a length of 1.5 m. After this stage the average power is about 50 W. The main amplifier fiber has cladding and core diameters of $500\ \mu\text{m}$ and $35\ \mu\text{m}$, respectively. The average power after this 12 m long fibre is more than 500 W, which is limited by mode instabilities [13]. These pulses are then compressed in a all-reflective grating stretcher to 250 fs at an average power of up to 420 W [122]. The whole system is set up on a $2.2\ \text{m} \times 1.4\ \text{m}$ breadboard. Despite the high average power, the laser has an excellent beam quality with an M^2 value of 1.2 , which is necessary for efficient coupling to the fundamental Gaussian mode in the enhancement cavity.

From the reflected light at the input coupler, an error signal is obtained using the Pound-Drever-Hall scheme. With it, the laser is locked to the cavity with an PID controller (Vescent D2-125 Laser Servo) actuating on an intra-oscillator EOM via a fast high-voltage-amplifier (Falco-systems WMA 300). Because the EOM only has a very small range, a slow loop actuating on a piezo in the enhancement cavity is used to adjust the EOM's signal to zero. This piezo is clamped between one translation stage and its

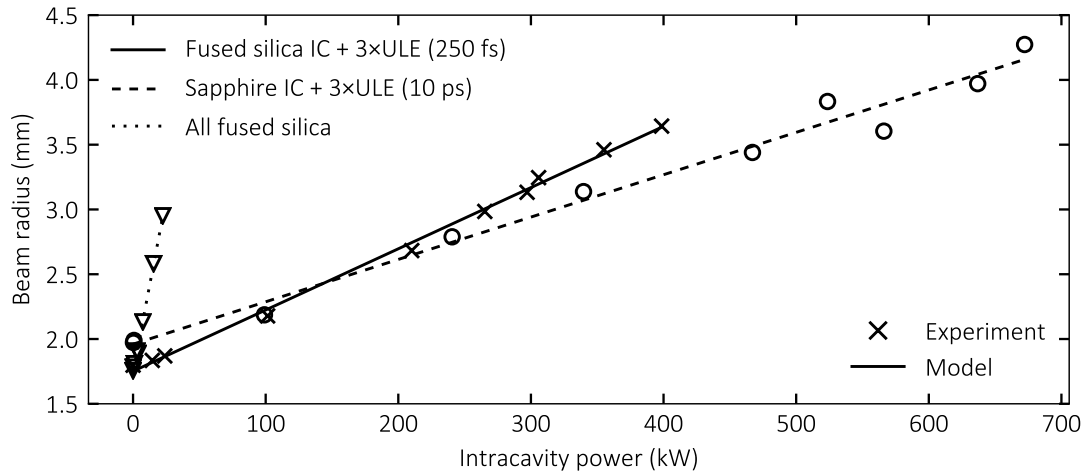


Figure 4.4 – The increase of beam size with increasing intracavity power for three different cavity configurations. By employing ULE substrates for the high-reflective mirrors, the beam size increase can be mitigated significantly. In addition, sapphire can be used for the input coupler improving the thermal sensitivity even further. However, it is prone to damage as the surface quality is worse.

adjustment screw. In this configuration, the slow loop does not act on the comb's offset frequency f_0 . If instead the intra-oscillator piezo was used, any drift compensated by the slow loop led to changes of f_0 , resulting in intracavity power fluctuations.

The enhancement cavity is set up in a vacuum chamber with a pressure of 10^{-4} mbar. As the SBT-cavity was identified as the most viable option for the following power scaling experiments, this design was implemented using two 600-mm radius of curvature mirrors and two plane folding mirrors. The cavity length is a 2.4 m. All three high-reflective mirrors are on ULE substrates. The input coupler is either on fused silica or sapphire (see next section). In this configuration, the angle of incidence is only 1.2° , so that the beam ellipticity is moderate. The intracavity light is analysed via the transmission through the high-reflective mirrors. The intracavity power is measured with a germanium-photodiode powermeter, the pulse duration can be estimated from an autocorrelation trace, and the cavity mode on one cavity mirror is imaged onto a CCD with calibrated magnification, which also allows one to determine the position in the stability range.

4.5 Experimental results

In Fig. 4.4, the increase in beam size for increasing power is plotted for three different cavity configurations. When only fused silica substrates with coatings similar to [44] are employed, the slope of the increase is 53.6 mm/MW. At some point, a further increase of

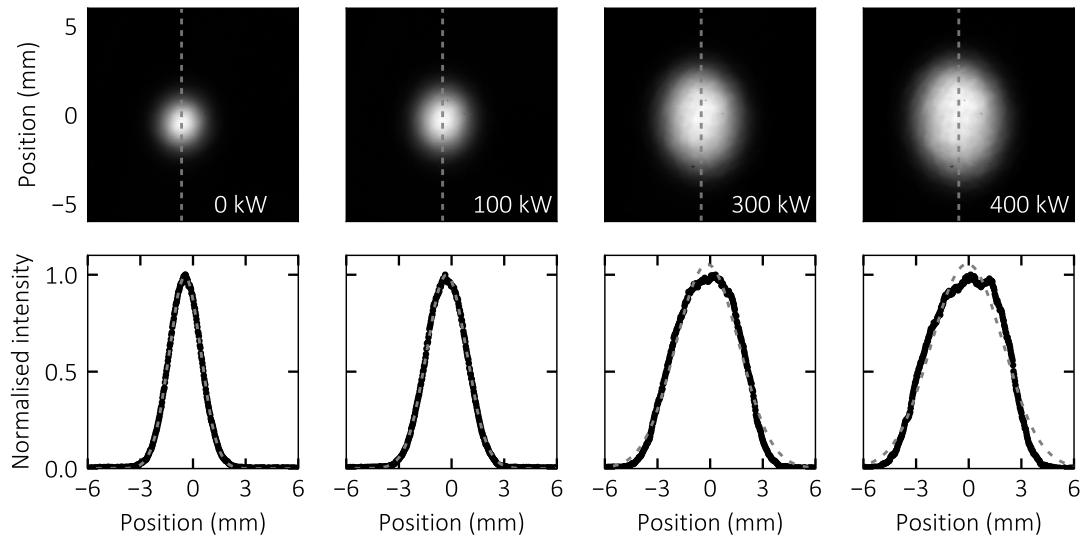


Figure 4.5 – Example intracavity beam profiles for increasing power. Apart from the increase in beam size, also a deviation from a purely Gaussian beam shape can be observed, as thermal aberrations couple power into higher-order modes. The vertical blue line indicates the linecut for the lower panels (blue dots), the dashed red line is a Gaussian fit.

the incident power does not lead to a higher intracavity power, because the cavity finesse is reduced by aberrations, as will be discussed in Section 4.6.

Using coatings optimized for a low absorption and ULE as the substrate material for the high-reflective mirrors and fused silica for the input coupler, this increase was reduced to 4.7 mm/MW. In this configuration, up to 400 kW of average power with a pulse duration of 250 fs at 250 MHz repetition rate were obtained. This corresponds to 1.6-mJ pulses with 55 GW peak power, that are focused to a $25 \mu\text{m} \times 34 \mu\text{m}$ focus resulting in a peak intensity of $4 \times 10^{14} \text{ W/cm}^2$. This was achieved with an input power of 315 W and a power enhancement factor of 1270. Again, the finesse was reduced by thermal aberrations. At low powers, the power enhancement was 2000. Here, the thermal sensitivity was improved by a factor of 4 due to the use of ULE and another factor of 3.8 due to a reduced coating absorption compared to the all fused silica case from Fig. 4.4. This result constitutes an improvement of a factor of 20 in terms of average power compared to previous record value reported in [44].

In Fig. 4.5, the cavity beam profile on one cavity mirror is plotted for different power levels. One can see that not only the size increases, but that also the shape deviates from a Gaussian beam at high power levels. This is because energy is coupled into higher-order modes by the thermally deformed mirrors, in this case only by the input coupler. When significant portions are coupled into higher-order modes, these show up in the circulating beam profile. In this configuration, a further increase of the incident

power did not lead to a higher intracavity power.

The thermal sensitivity was further reduced by employing sapphire as the substrate material of the input coupler, see Section 4.3. The slope of the increase in beam size was 3.3 mm/MW, see Fig. 4.4, although for this experiment the initial beam size was larger than for the other two cases. However, the input couplers on sapphire substrates were repeatedly damaged even with stretched pulses. Probably, this is due to the higher surface roughness of sapphire compared to fused silica. Up to 670 kW of average power were achieved with 10-ps pulses.

During these experiments, an optical bi-stability as described in [124] was observed. This is because of fast changes of the cavity length due to thermal expansion of the mirrors, see Section 4.6.3. While locking the laser to the cavity, this might result in oscillations of the intracavity signal on the kHz-scale. The locking loop, including the slow integrator, must be faster than this. When the piezo acted on the intra-oscillator piezo instead, that also changes the comb's offset frequency, locking instabilities occurred. This is because the intracavity power depends on the comb's offset frequency [125], which in turn is changed by the locking loop when the power changes. For reliable operation, both comb parameter f_{rep} and f_0 must be controlled with as little crosstalk as possible. This was enabled by letting the slow integrator act on a piezo in the enhancement cavity, which only changes the cavity length, but not the optical offset frequency.

4.6 Limitations for the achievable intensity and average power

In the experiments, the power level could not be improved by increasing the incident power, because the power enhancement factor declined at high powers. This can be attributed to aberrations. As discussed in Section 2.4.2, aberrations couple power from the fundamental mode to higher-order modes. If the high-order modes are not degenerate, this constitutes a loss mechanism for the cavity, which explains the observed behaviour. In this section, the role of spherical and thermal aberrations will be discussed.

4.6.1 Spherical aberrations

In cylindrical coordinates, a spherical surface with radius R touching the origin can be written as $r^2 + (z + R)^2 = R^2$. From this, the optical-path-length difference $\Delta(r)$ can be calculated,

$$z(r) = \Delta(r)/2 = \sqrt{R^2 - r^2} - R \quad (4.5)$$

$$\approx -\frac{r^2}{2R} + \frac{r^4}{8R^3} \mp \dots, \quad (4.6)$$

where $\sqrt{1+x} \approx 1 + x/2 - x^2/8$ was used. The acquired phase is then given by $\phi(r) = \exp [ik \cdot \Delta(r)]$. From the comparison with a parabola, $p(r) = r^2/(4f)$, the focal length of a spherical mirrors follows, $f_{\text{sp}} = R/2$. The spherical aberrations scale with w^4 and R^{-3} .

For enhancement cavities, a good measure for the strength of aberrations is the overlap of a fundamental Gaussian beam after reflection from an optical element disregarding its focusing effects [54], as discussed in Section 2.4.2. From Eq. (2.48), the aberration losses can be calculated. This value is plotted for a range of beam radii and mirror curvatures in Fig. 4.6. While in many cases spherical aberrations can be neglected (e.g. for losses < 1 ppm), their strength can be significant for large beam sizes and tight focusing. Note that the intensity discrimination scales with w^4 and f^{-2} (Eq. (3.1)), while the spherical aberrations scale with w^4 and f^{-3} (Eq. (4.6)). Thus, tight focusing (small f) reduces spherical aberrations stronger than it decreases the intensity discrimination. If high intensities are desired, tight focusing in conjunction with astigmatic compensation should be employed.

For example, in order to achieve an intensity discrimination of 10^5 required for a peak intensity of 10^{16} W/cm² with a focus of $7 \mu\text{m}$, $f \approx 50$ mm focusing must be employed according to Eq. (3.1). This implies a beam radius of 2.21 mm on the curved mirrors. The aberration losses for this configuration are 1.75% for each mirror, limiting the maximum enhancement to less than 30. An intensity discrimination of 10^4 for a peak intensity of 10^{15} W/cm² can be obtained with $f \approx 15$ mm and $w_0 = 7 \mu\text{m}$. Then, the spherical aberrations are 0.25%. With two curved mirrors and a focus radius of $7 \mu\text{m}$, this limits the achievable enhancement to 200. Thus, in enhancement cavities employing spherical mirrors, the peak intensity is limited to the 10^{15} W/cm²-level assuming a damage threshold of 10^{11} W/cm². Higher intensities might be obtained using parabolic reflectors [126] or by increasing the beam divergence, e.g. by employing Gauss-Bessel beams [80, 127, 128]. For focus radii smaller than $10 \mu\text{m}$, the paraxial approximation [129] does not hold any more and corrections to it have to be considered [130, 131].

4.6.2 Thermal aberrations

In contrast to spherical aberrations, thermally induced aberrations are independent of the beam size, as it is the case for transmissive thermal lenses [15]: The aberrations are proportional to the phase difference $\Delta\phi$ between the middle and the edge of the beam acquired upon reflection. This only depends on the absorbed power and on the thermal properties of the substrate, $\Delta\phi \propto \alpha/\kappa \cdot P_{\text{abs}}$, but not on the beam radius [57]. In Fig. 4.7, the thermally induced focal length of a 25-mm round substrate with a thickness of 6.3 mm is plotted from Eq. (2.41). From the deformation profile, the aberrations can be calculated (right hand panel). This confirms that for standard 25-mm optics the strength of thermal aberrations is independent of the incident beam radius even when

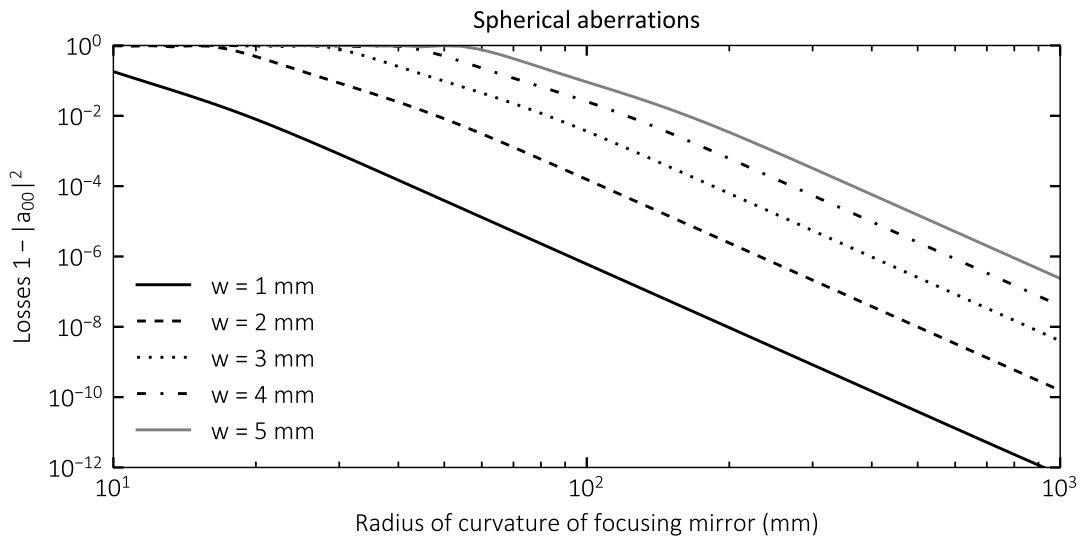


Figure 4.6 – The aberration losses $l_{ab} = 1 - |a_{00}|^2$ for a range of beam radii and mirror curvatures. The plot covers 13 orders of magnitude – for many cases spherical aberrations can be neglected, while they become significant for tight focusing with large beams.

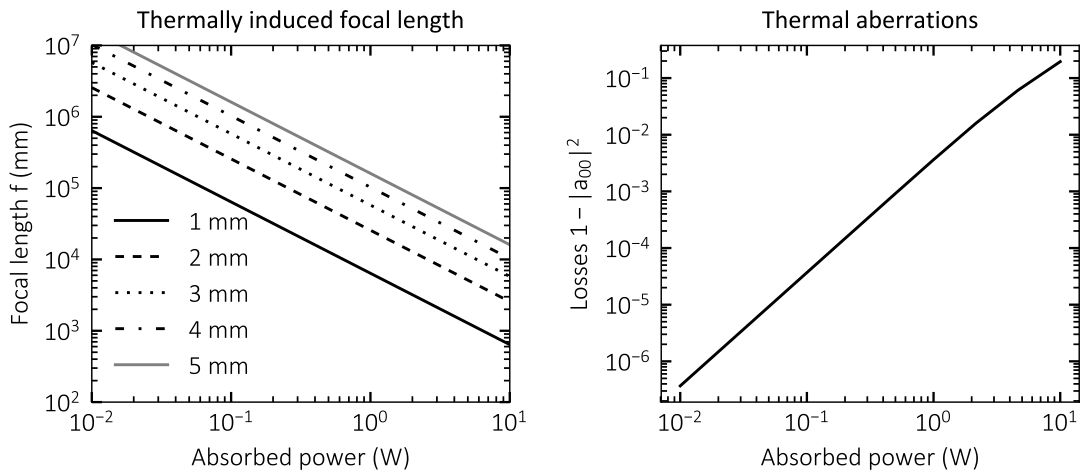


Figure 4.7 – (Left) The thermally induced focal length obtained from a best-fit parabola for the deformation profile given by Eq. (2.41) for a standard round 25-mm diameter fused silica substrate with a thickness of 6.3 mm. (Right) From the deformation profile, the strength of thermal aberrations is calculated. It is independent of the incident beam radius.

the finite dimensions of the substrate are considered.

The aberration losses for an absorbed power of 0.4 W, corresponding to 400 kW of average power with an coating absorption of 1 ppm as in the experiment, are 0.06%. This explains the drop in enhancement in the experiment from 2000 at low powers to 1270 at 400 kW. For 1 W of absorbed power (1 MW of average power) the losses are already 0.36% limiting the achievable enhancement in an impedance matched case to less than 300. In order to reach 1 MW, one would then need a 3.5 kW laser, which does not exist yet [97, 132, 133]. Thus, with currently available laser technology and state-of-the-art dielectric mirrors, the average power in enhancement cavity using one fused silica mirror is limited to less than 1 MW. This is independent of the cavity design.

Summary: The achievable intensity and average power levels

The power and intensity in ultrashort pulse enhancement cavities is limited by mirror damage. In principle, this may be circumvented by proper cavity design with large spot sizes on all optics can be obtained, as discussed in Chapter 3. However, ultimately aberrations reduce the achievable enhancement. With state-of-the-art optics and laser technology, the peak intensity is limited to the 10^{15} W/cm² level with two spherical mirrors and to the 1 MW average power level with one fused silica input coupler. Better values might be obtained using parabolic reflectors and/or alternative input couplers.

4.6.3 Transient thermal lensing

In Fig. 4.8 the transient thermal deformation of a standard 25-mm mirror heated by a 2-mm Gaussian beam with 1 W of absorbed power is shown in time steps of 0.3 s (upper left panel). This was obtained by numerical solution of the time-dependent heat equation and Hooke's law, see Section 4.1, using the commercial software Comsol. Alternatively, analytical models can be employed [56]. In the lower panels, the transient behaviour of the focal length and aberrations losses are plotted.

The thermal lens needs a few seconds to build up. One important implication is that for intensity-induced mirror damage, one has to consider the beam size of the cold cavity, because the build-up of the intracavity power takes place in less than one millisecond. On the other hand, significant deformation of some nanometers occurs on the timescale of milliseconds (upper right panel of Fig. 4.8). For high-finesse cavities the resonance linewidth with respect to the cavity length is less than 1 nm. Thus, thermally induced perturbations occur on the kHz scale, which has been observed during the experiments. The feedback loop including the slow part for large perturbations must be faster than this.

In reality, the transient behaviour of the enhancement cavity is more complex: Any

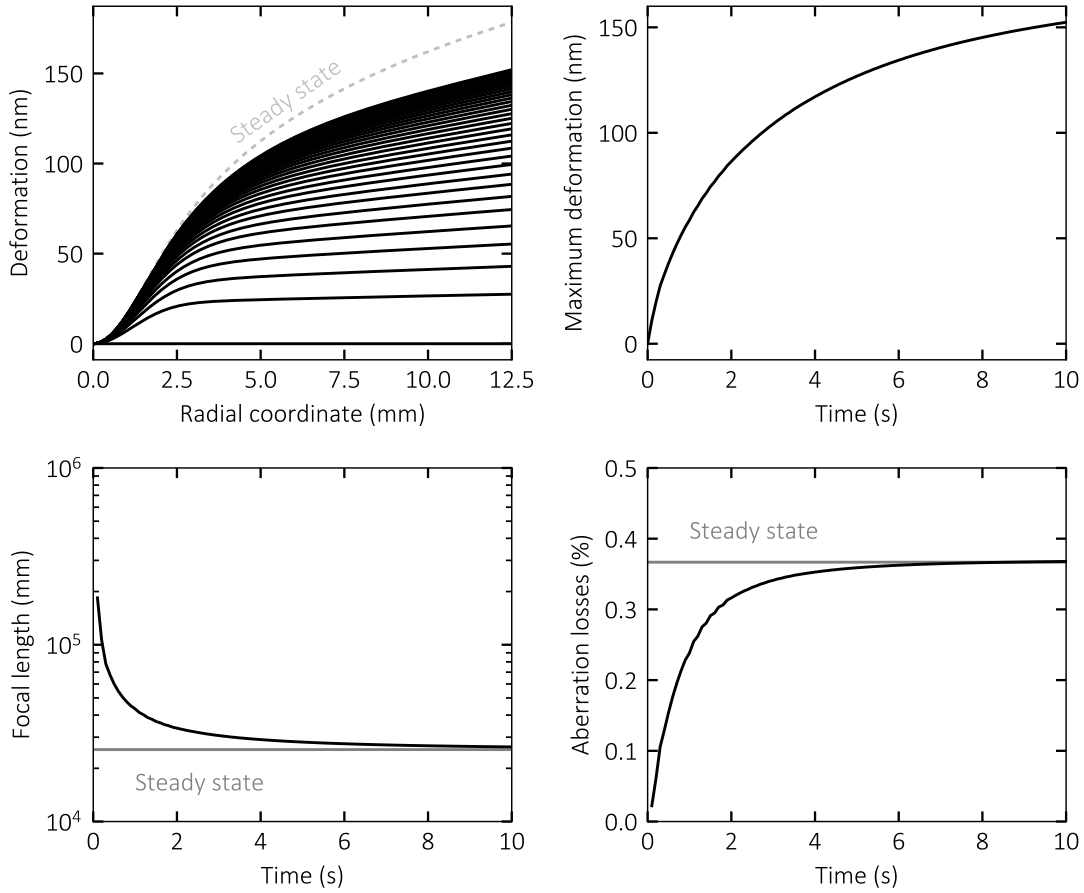


Figure 4.8 – Time-dependent thermal lensing. (Upper left) The deformation profile in time steps of 0.3 s. (Upper right) The maximum deformation as a function of time. Deformation on the scale of one resonance linewidth (1 nm) occurs on the millisecond time scale. (Lower left) Thermal focal length obtained by a best-fit parabola as a function of time. (Lower right) Aberrations losses as a function of time.

change in thermal lensing leads to a change of the cavity eigenmode, which in turn changes thermal lens. This could be simulated by numerical wave propagation [134, 135] under consideration of the transient thermal lensing. In principle, such an algorithm would work like the following. The algorithm is based on numerical wave propagation using a fast-fourier transformation of two-dimensional fields. Here, a complex field $E_z(x, y)$ can be propagated from one z -plane to another at distance Δz using a two-dimensional Fourier transformation \mathfrak{F} [136]:

$$E_{z+\Delta z}(x, y) = \mathfrak{F}^{-1} \left[\mathfrak{F}[E_z(x, y)] \cdot H(k_x, k_y, \Delta z) \right] \quad (4.7)$$

with the Fraunhofer transfer function ($k_0 = 2\pi/\lambda$) with Fourier-space grid variables

k_x, k_y [136]

$$H(k_x, k_y, \Delta z) = \exp\left(\frac{i(k_x + k_y)^2 \Delta z}{2k_0}\right). \quad (4.8)$$

In the following, the k_x, k_y dependency will be dropped, $H(\Delta z) = H(k_x, k_y, \Delta z)$. Reflection from a mirror is governed in the real space by multiplication with a phase factor $\exp(ikZ_{\text{OPL}}(x, y))$ determined by the optical-path-length difference $Z_{\text{OPL}}(x, y)$, which includes both the spherical shape and thermal deformation.

These formulas are used to propagate the field through the cavity. When macroscopic length scales are used for the propagation, an additional scalar phase factor has to be multiplied onto the circulating field, so that it can interfere constructively with the incident field at the input coupler. A good estimate for it is given in Ref. [134]. The following example is for a standard bow-tie cavity with cavity length L consisting of two spherical mirrors with radius-of-curvature R separated by a distance d . For simplicity, it is assumed that the light is coupled in through one of these curved mirrors, so that no other optical elements have to be considered.

Algorithm

- Initialize parameters, $E_{\text{in}}(x, y)$: input field, t, r : input coupler field transmission and reflectivity, a : round-trip field attenuation
- Circulating field $E_{\text{circ}}(x, y) = t \cdot E_{\text{in}}$
- For $N \approx 3\mathcal{F}$ round-trips do:
 - Calculate intracavity average power and use it for the transient thermal deformation, e.g. using Comsol. Update the thermally induced path-length difference Z_{thermal} of the input coupler.
 - Propagate $E_{\text{circ}}(x, y)$ through cavity:
 1. $E_{\text{circ}} = \mathfrak{F}^{-1} [\mathfrak{F}[E_{\text{circ}}] \cdot H(d)]$
 2. $E_{\text{circ}} = E_{\text{circ}} \cdot \exp(i\phi_{\text{mirror}}(R))$
 3. $E_{\text{circ}} = \mathfrak{F}^{-1} [\mathfrak{F}[E_{\text{circ}}] \cdot H(L - d)]$
 4. $E_{\text{circ}} = E_{\text{circ}} \cdot \exp(i\phi_{\text{mirror}}(R, Z_{\text{thermal}}))$
 - Find on-resonance phase factor φ [134]
 - Input coupling: $E_{\text{circ}} = ar e^{i\varphi} \cdot E_{\text{circ}} + t \cdot E_{\text{in}}$

4.7 Conclusions

In this chapter, thermal effects in ultrashort pulse enhancement cavities were investigated. A quantitative model for the impact of reflective and transmissive thermal lenses in cavities was developed. It turns out, that the thermally induced beam increase can be mitigated by employing longer cavities and/or tight focusing geometries. This allows for the design of enhancement cavities with MW-scale average powers. In an experiment, up to 400 kW with 250-fs pulses and up to 670 kW with 10-ps pulses were obtained at a repetition rate of 250 MHz. This constitutes an improvement of more than one order of magnitude of the average power over previous results [44]. The results are enabled by mirrors on substrate materials with superior thermal properties, in this case ULE, for the high-reflective mirrors and with a coating absorption as low as 1 ppm. Intensity induced mirror damage was avoided by the cavity design developed in the previous chapter, namely a bow-tie cavity operated close to the inner stability edge with large beam sizes on all optics. These results are limited by thermal lensing: For the input coupler either sapphire or fused silica have to be used because of their low bulk absorption, which results in significant thermal lensing at the 100-kW average power level. This setup lends itself for the generation of hard x-rays by inverse Compton-scattering from relativistic electrons.

Aberrations induced by the deformation of the input coupler transfer power into higher-order modes. This power is effectively lost due to the mode filtering properties of optical resonators. It was shown that with currently available laser technology and state-of-the-art dielectric mirrors, the average power in enhancement cavities using one fused silica mirror is limited to less than 1 MW. Higher power levels might be obtained by even better substrate materials, for example diamond. However, currently single crystal diamond substrates are not available in sufficient size and for a reasonable price. Alternatively, one could use a reflective input coupler based on a grating [137, 138]. On the other hand, a further increase of the cavity length would mitigate the thermally induced beam increase, which is crucial for certain applications such as HHG (see Chapter 5), but would not allow for a higher intracavity power, as this is limited by aberrations, which are only dependent on the absorbed power and substrate properties.

CHAPTER 5

High-harmonic generation at 250 MHz repetition rate

This chapter is about cavity-enhanced high-harmonic generation. In Section 5.1, the requirements, efficiency, and limitations in enhancement cavities are discussed. The apparatus for the experiments is introduced in Section 5.2 and the results obtained with it are presented in Section 5.3. The results and their impact are concluded in Section 5.4.

5.1 High-harmonic generation in enhancement cavities

5.1.1 Motivation

The first application for ultrashort pulse enhancement cavities were frequency combs in the (extreme) ultraviolet via high-harmonic generation [33, 34]. There are two major reasons for an enhancement cavity instead of using a simple single-pass geometry: First, it allows for the necessary intensities of $10^{13} \text{ W/cm}^2 - 10^{14} \text{ W/cm}^2$ at repetition rates on the order of 100 MHz. Even with ultrashort pulses and tight focusing, this implies average powers of several kW, which is currently unattainable from a single laser. Second, if the conversion efficiency inside the enhancement cavity is the same as that of single pass experiments, the overall generation efficiency would be better by a factor identical to the power enhancement. However, as of the time of writing, the photon flux from single-

pass sources is better than that from enhancement cavities. There are several reasons for this: In cavity-enhanced high-harmonic generation the achievable intensity is limited by a non-linear phase shift upon target ionization [61–63], the generation efficiency is limited by a cumulative plasma at MHz-repetition-rate [35, 82], and a certain part of the generated radiation is lost upon output coupling [139–141]. In the following sections, these factors will be discussed.

Enhancement cavities are used for the generation of frequency combs in the extreme ultraviolet [33, 34]. In this spectral region, neither powerful cw-lasers, nor pulsed lasers exist. Thus, one transfers lasers emitting in the visible to the near-infrared, for example titanium-sapphire [33, 81, 142] or ytterbium doped fibre lasers [24, 79], into the desired spectral range using non-linear effects, in this case high-harmonic generation. This process has been shown to preserve the long coherence time necessary for high precision spectroscopy [143, 144]. Then, one can perform direct frequency comb spectroscopy, i.e. the comb is used both for frequency measurement and for excitation of the probe [24, 145]. Several transitions in the XUV are of particular interest. For example, the quantum electrodynamic corrections to the energy levels of hydrogen-like ions scale with Z^4 [25]. Thus, one would like to measure the two-photon 1s-2s transitions of He^+ at 40 eV (e.g. 20 eV + 20 eV or 39 eV + 1 eV) or Li^{2+} at 91 eV (e.g. 45.5 eV + 45.5 eV or 90 eV + 1 eV). By wavelength scaling of frequency combs, also nuclear transitions come into reach, for instance a nuclear transition of ^{235}U at 76 eV [27]. This would allow for new insights into nuclear physics and possibly for next generation optical clocks with unprecedented accuracy [24].

Another class of applications, which would benefit from high-repetition rate extreme ultraviolet sources are pump-probe experiments. In particular, experiments concerned with the detection of photoelectrons suffer from long integration times or poor signal to noise ratio, because space charge effects limit the usable electrons per shot (ideally only one). The only way to improve the electron flux is to increase the repetition rate. When high time resolution is desired, also high photon energies are required, because only then photoelectrons are fast enough to leave the sample within, say, a few femtoseconds. For example, electrons liberated by 91 eV photons from a material with work function 5 eV have a speed of $v_e = 5 \times 10^8$ cm/s, which allows a time resolution for nanoplasmonic structures of 1 nm of 180 as [29]. Experimentally, this might be achieved using a photoelectron emission microscope in conjunction with a time-of-flight spectrometer [29]. For 100 nm structures, a time resolution of 18 fs would be achievable. So far, this experiment was only possible for single pictures at kHz repetition rate [30]. Advancing high-harmonic sources to the multi-MHz level will allow recording many pictures for a time-resolved measurement. Other time-domain applications include angularly-resolved photoelectron spectroscopy (ARPES) [31] and cold-target recoil-ion momentum spectroscopy (COLTRIMS) [32]. Typically, the usable repetition rate in these experiments is limited by the detector, e.g. to the 10 MHz level by time-of-flight

detectors or to about 100 MHz by a multichannel plate (MCP). Thus, a repetition rate of 250 MHz as used here is too high for these experiments. However, the methodology for improving the XUV photon flux also applies to lower repetition rate enhancement cavities [146]. In fact, for lower repetition rates the cumulative plasma discussed below is lower, so that the photon flux should be even higher.

5.1.2 Intensity clamping

Upon propagation through the gas target, the pulse ionizes a certain part of it, resulting in a rapid change of the refractive index. The accumulated phase shift is approximately given by

$$\Theta(t) = r_e \lambda \eta(t) \rho L_{\text{med}} \quad (5.1)$$

with the classical electron radius r_e , the center wavelength of the pulse λ , the ionization fraction $\eta(t)$, the number density of the gas ρ , and the length of the gas target L_{med} [63]. The maximum phase shift at the end of the pulse Θ_{max} is limited to about $6.3/\mathcal{F}$ [63]. Since for stronger phase shifts the pulse would be distorted too much for efficient interference with the next pulse at the input coupler. Thus, the intracavity peak intensity is limited [61] and this so-called clamping intensity depends on the pulse duration, the cavity finesse, medium length, and the gas species [63]. Note that the intensity for efficient high-harmonic generation is also limited because for too high intensities the critical ionization from Eq. (2.57) is exceeded which impedes phase matching. However, as of this writing the clamping intensity in experiments was lower than that of similar single-pass experiments resulting in a lower conversion efficiency, see Section 5.1.4. In both cases the limitation depends on the ionization degree, so that shorter pulses allow for higher intensities, which is highly desirable.

5.1.3 Cumulative plasma

At densities typical for high-harmonic generation the plasma recombination is governed by a three-body-process with a rate

$$\frac{dn_e}{dt} = -bn_e^3 \quad (5.2)$$

with the electron density n_e and a proportionality constant b [63]. This differential equation has the following analytical solution with $n_e(0) = n_{\text{max}}$

$$n_e(t, n_{\text{max}}) = \frac{1}{\sqrt{2bt + n_{\text{max}}^{-2}}}. \quad (5.3)$$

The recombination times predicted by this model are on the order of several 10s of nanoseconds and therefore longer than the pulse repetition times $\tau = 1/f_{\text{rep}}$ considered

here, e.g. 4 ns at 250 MHz. Thus, a cumulative plasma arises. This is depicted schematically in the left panel of Fig. 5.1. With every pulse, the electron density increases by a number Δn_e and decays to a non-zero value n_{low} . In the steady state, the number of recombined electrons according to Eq. (5.3) plus the number of electrons leaving the interaction region $\Delta n_{e,leaving}$ must be equal to the number of generated electrons upon one pulse transit. With $n_{high} = n_{low} + \Delta n_e$:

$$\Delta n_e + \Delta n_{e,leaving} = n_{high} - n_e(\tau, n_{high}) \quad (5.4)$$

This equation is solved for a range of peak intensity of 30-fs pulse for xenon in the right panel of Fig. 5.1. The cumulative or steady-state plasma n_{low} is mainly governed by the tail with low decay rate. Thus, for higher intensities the cumulative electron density saturates.

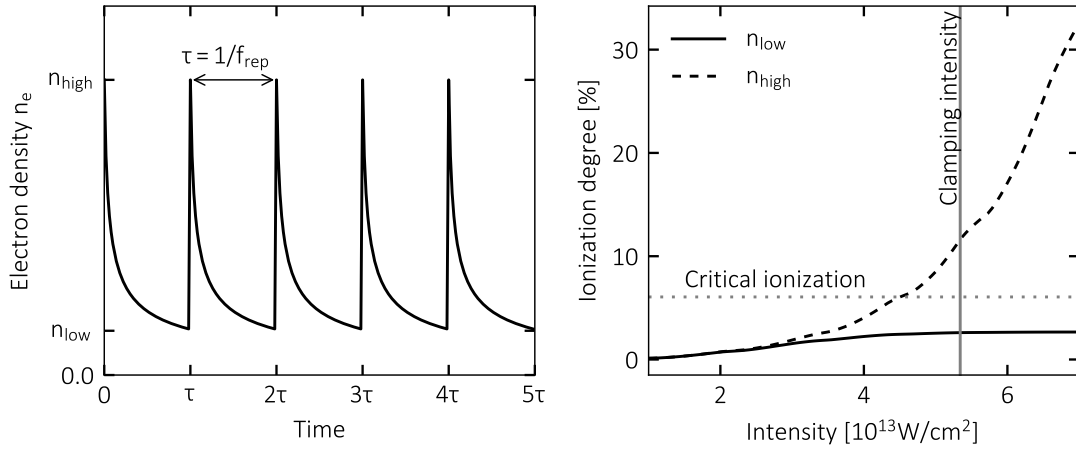


Figure 5.1 – (Left) Course of the electron density. It does not decay to zero, but to cumulative density n_{low} (Right) Electron density before and after ionisation of a 30-fs pulse. The bumps are due to the PPT ionisation rate.

5.1.4 Conversion efficiency

The on-axis conversion efficiency can be calculated with the model from Section 2.5.3. However, important parameters as the ionization rates and the dipole strength are not described with high enough accuracy, one cannot use this model for a global optimization. Still, an analysis of these equations provides good insights into the principles of efficient high-harmonic generation.

Critical ionization

In general, one has to achieve phase matching of the single emitters at high intensities of the driving field, as the dipole strength scales highly nonlinearly with the intensity

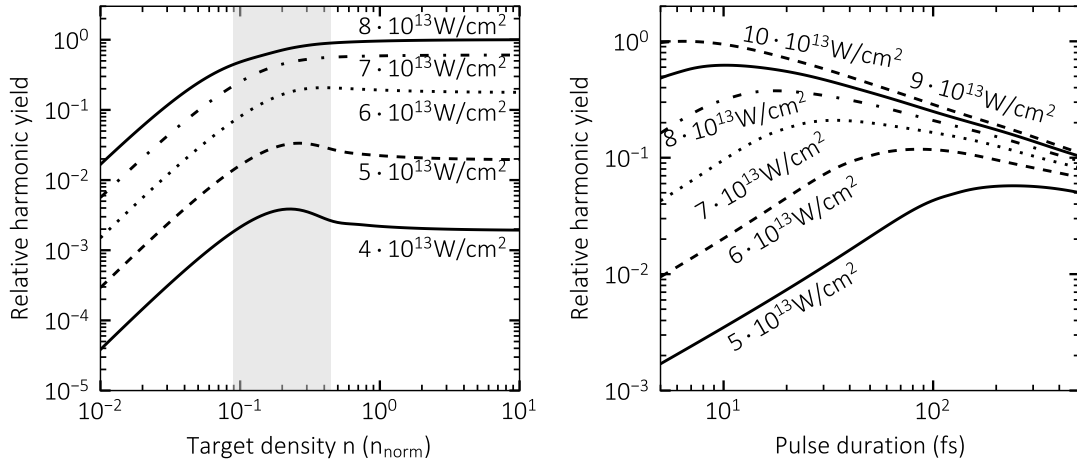


Figure 5.2 – (Left) Relative harmonic yield as a function of the target density for H17 in xenon. The shaded area indicates the phase matching density for an ionization degree relative to the critical ionization from 0.0 to 0.8. (Right) Relative harmonic yield as a function of pulse duration. For each point, the density as optimised numerically.

Eq. (2.51). No phase matching can be achieved for ionization degrees exceeding the critical ionization from Eq. (2.57), which limits the usable driving intensity. As a rule of thumb, the intensity should be chosen such that the critical ionization is only slightly exceeded. For higher intensities, no further increase in harmonic flux is expected.

Pressure induced phase matching

In the left panel of Fig. 5.2 the flux of the 17th harmonic from a 200- μm long xenon target is plotted for a 30-fs pulse. The shaded area indicates the phase matching density from Eq. (2.58) for ionization degrees relative to the critical ionization ranging from 0.0 to 0.8. The phase matching density at the critical ionization would be infinity Eq. (2.58). For every intensity, the flux increases with density until it reaches an optimum around the phase matching density. The optimum slightly shifts towards higher densities for higher intensities as here the relative ionization degrees are higher. At low intensities, Maker fringes can be observed, but at optimal intensities, the yield saturates for high gas densities. The fringes can also be observed experimentally [72]. An increase of $7 \times 10^{13} \text{ W/cm}^2$ to $8 \times 10^{13} \text{ W/cm}^2$ does not increase the on-axis flux significantly in this example. In an experiment, one would choose a focus size to obtain an intensity in this range.

Optimal intensity

In the right panel of Fig. 5.2 the harmonic flux from a 200- μm long xenon target is plotted for various peak intensities as a function of the pulse duration for an optimum density for each point. Note that for this on-axis model only the peak intensity and the

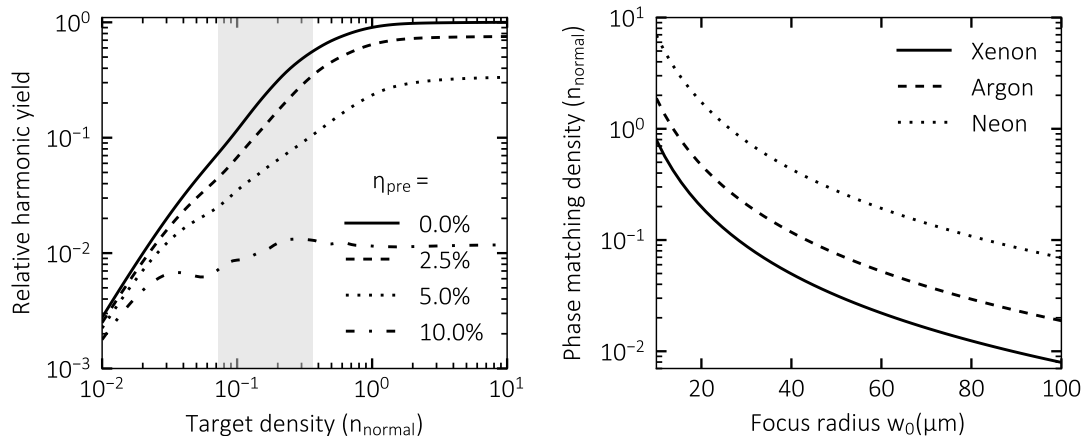


Figure 5.3 – (Left) Relative harmonic yield of the 17th harmonic in xenon from a 30-fs pulse in a pre-ionized medium. (Right) Phase matching density in units of the density at normal conditions for xenon, argon, and neon.

pulse duration are important. One can interpret this plot as if the pulse has constant energy and focus size is adjusted to obtain each intensity. At low intensities, for instance $5 \times 10^{13} \text{ W/cm}^2$, the critical ionization is not exceeded. Then, longer pulses are actually beneficial because then more light cycles can coherently emit phase matched. For too long pulses the critical ionization is exceeded so that the flux decreases here again. Thus, there is an optimal pulse duration for every peak intensity. This optimum improves and shifts towards shorter pulses for increasing intensities. As expected, high intensities are highly beneficial, but can only be used for short enough pulses. In other words: Short driving pulses are desired, because high-harmonic generation can be driven at higher intensities without exceeding the critical ionization.

Cumulative plasma limitations

In the presence of a cumulative plasma, every pulse in the enhancement cavity propagates through a pre-ionized gas target. Then, the phase matching window – the time until the critical ionization is exceeded – is shorter, resulting in a lower generation efficiency. In the left panel of Fig. 5.3, the relative harmonic yield is plotted for different pre-ionization levels. For a pre-ionized medium, the efficiency is lower and the optimal density shifts to higher values, as the average ionization degree is higher according to Eq. (2.58).

5.1.5 Limitations of the on-axis model

Of course, an on-axis model does not describe any transverse spatial effects, in particular the influence of the focus size. For a large focus the focal volume, i.e. the volume in which the intensity exceeds a certain value, is increased because of the larger transverse beam size and because of the smaller beam divergence. Thus, harmonic radiation is

emitted from a larger volume and one could assume that the flux is improved. However, experimentally it was found that the focus size has only a minor influence [72] provided that absorption-limited and phase matched conditions can be achieved in a tight-focusing geometry [67]. One explanation for this might be the following: The overall flux is proportional to the number of emitters that can be phase matched. For tight focusing, the cross sectional area is smaller (scaling w_0^2), but the phase matching density is higher and scales with w_0^{-2} (Eq. (2.58)), so that the integral of the emitters over a cross-section is independent of w_0 . The reduced beam divergence does not improve the flux in an absorption-limited case, because the coherence length is limited by reabsorption and not by the beam divergence [60].

These considerations only hold, if the absorption limit can be reached. For photon energies $\gg 100$ eV, the reabsorption typically becomes small, resulting in very long absorption lengths. Then, it is not trivial to reach the absorption limit, because very long coherence lengths are required. They might be obtained using quasi phase matching in hollow core fibers [147]. For example, the absorption length for 60 nm in xenon at standard conditions is only 12 μm , that of neon at 13 nm is 125 μm , and that of helium in the water window at 4 nm is 24 mm [148].

5.2 Experimental apparatus

5.2.1 Laser system and enhancement cavity

In Fig. 5.4 a schematic of the experimental setup used for the generation of high harmonics is depicted. The seeding laser was the same as in the previous chapter and is described in more detail in [122]. The pulses are coupled into a large-pitch fiber [149, 150] with a mode-field-diameter of 59 μm . Here, the spectrum of the pulses is broadened via self-phase modulation from 15 nm to about 120 nm matching the supported bandwidth of $\text{SiO}_2\text{-Nb}_2\text{O}_5$ mirror coatings [125]. The pulses are then compressed using chirped mirrors to 30 fs pulse duration.

After spatial mode matching in a telescope, these pulses are coupled into the enhancement cavity. It consists of six mirrors in total: four high-reflective mirrors on ULE substrates, one pierced mirror and one input coupler on fused silica. All mirrors have a quasi-quarter-wave-stack coating consisting of alternating layers of SiO_2 and Nb_2O_5 . The cavity was operated in two different configurations:

- (a) Using $R = 600$ mm mirrors and a round-trip length of $L = 4800$ mm (four circulating pulses)
- (b) using $R = 200$ mm mirrors and a round-trip length of $L = 3600$ mm (three circulating pulses)

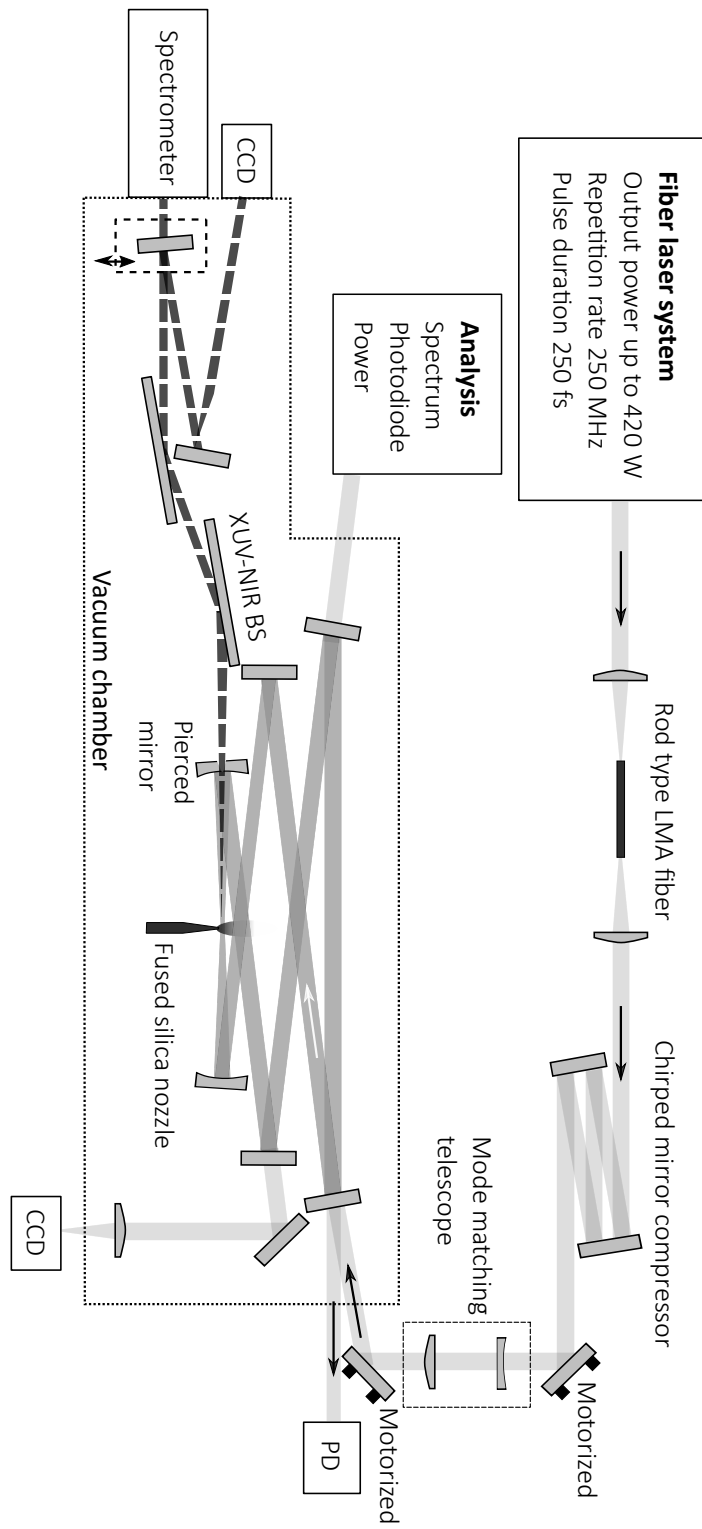


Figure 5.4 – Schematic of the experimental setup for high-harmonic generation. See text for more detail. LMA: large-mode-area, PD: photodiode, CCD: charge-coupled device, BS: beamsplitter

Previous experiments showed that the dispersion of eight mirrors is too high to support 30-fs pulses in the cavity [151]. In both cases, the longest cavity that fits into the vacuum chamber with six mirrors was set up, as this reduces the thermally induced beam increase and thus allows for a more robust operation of the experimental setup.

The analysis of the intracavity light and the locking scheme is similar to that described in Section 4.4. Here, the power was measured with a thermal powermeter (Thorlabs S302C), as its response is flat for the entire spectrum of the pulse. The beam profile on the pierced mirror is imaged onto a CCD and can be used to verify that the mirror opening is centred on the beam. For long-term stability, a beam stabilization consisting of two motorized mirror mounts, two four-quadrant photodiodes and four PID controllers (two axes for each mirror mount) was integrated into the laser system.

In order to obtain a high density target for high-harmonic generation in the tight-focusing regime, the gas nozzle has to be put very close to the cavity beam, so that it will always clip and absorb a small portion of the intracavity light. Nozzles made of borosilicate glass easily melt. Instead, nozzles made of fused silica are used here, because of their lower absorption (typically 10^{-5} cm^{-1} instead of 10^{-3} cm^{-1} for borosilicate) and much higher softening point (1650° instead of 800° for borosilicate). The fabrication is somewhat more elaborate. Nozzles with opening diameters of about $100 \mu\text{m}$ can be made by tapering capillaries with a high-temperature flame, e.g. with an acetylene-oxygen welder. Additionally, high backing pressures have to be applied. In order to handle the high gas loads, a powerful pumping system is necessary. Here, a magnetically levitated turbo-molecular pump with a pumping speed of $16001/\text{s}$ (for N_2) and, more importantly, a maximum gas throughput of $8 \text{ Pa m}^3/\text{s}$ for N_2 and $3 \text{ Pa m}^3/\text{s}$ for Ar is employed (Edwards STP-iXR1606). This pump is backed by an Edwards iXL120 with a maximum pumping speed of $110 \text{ m}^3/\text{h}$.

Three mirrors, namely the pierced mirror and the two successive ones, are purged with ozone (O_3). The ozone reacts with hydrocarbons on these mirrors and the product evaporates and leaves the chamber through the pumps. Otherwise, the generated XUV radiation would crack the hydrocarbons leaving a thin layer of carbon, which diminishes the reflections of these mirror. With ozone purging reliable operation over the whole period of experiments was possible. Hydrocarbon contamination was reported to be problematic for cavity-enhanced HHG before [85].

5.2.2 XUV output coupling

Output coupling techniques were discussed in Section 3.3.1. Here, the pierced mirror technique is chosen [86, 139], which it is the only technique demonstrated so far for photon energies exceeding 40 eV. It offers the following features: It adds no additional dispersion apart from the mirror's coating, all harmonic orders are coupled out collinearly, and any polarisation can be used. The cavity is operated with a fundamental

Gaussian beam. At the pierced mirror, a certain power fraction is transmitted through the hole and the same fraction is coupled into higher-order modes. If they are not degenerate with the fundamental mode, this results in power losses of $1 - \exp[-4(r_h/w)]$ [86], with the hole radius r_h and the beam radius on the pierced mirror w .

The output coupling efficiency of the pierced mirror depends on the divergence of the generated XUV radiation. For the q -th harmonic order and a Gaussian beam profile, it is given by $T_q = 1 - \exp[-2(r_{\text{XUV}}/w_q)]$ with the free aperture for the XUV radiation r_{XUV} and the beam radius of the q -th harmonic w_q on the pierced mirror [86]. Depending on how the holes are manufactured, the free aperture for the XUV radiation can be significantly smaller than the outer hole radius r_h (see below). In a simple picture, one can assume that the XUV divergence is smaller by a factor q (because the wavelength is smaller by that factor) and higher by a factor \sqrt{p} , $p \approx 5$ (because spot size of the XUV light is smaller by this factor) compared to the divergence of the fundamental light [86]. However, this neglects the significant influence of the dipole phase, so that the actual divergence is higher [152, 153] and the resulting output coupling efficiency lower than predicted by the simple model. For a more accurate estimation of the output coupling efficiency, full simulations of the coherent build up in the gas target must be conducted [79, 154]. The model is based on the Lewenstein-model for the dipole strength and full propagation of the generated radiation through the ionised gas target¹. However, for several critical parameters the values are inflicted with a large uncertainty from the experiment (gas target position, peak intensity) or cannot be calculated with sufficient accuracy (ionization rate), so that this only constitutes an estimation. An example is depicted in Fig. 5.5. One can see that when the gas target is moved in front of the focus, the generation efficiency can be maintained when the gas density is increased accordingly (upper panel). Here, the XUV divergence is minimized because the phase front of the driving field partly compensates for the dipole phase, resulting in an improved output coupling efficiency (lower panel). The output coupled power is maximised for the gas target placed about half a Rayleigh-length in front of the focus (middle panel). Then, the output coupling efficiency for the 79th harmonic is 8% in this example, for which the losses for the driving field are 0.5%. In this example, the free aperture of the hole r_{XUV} was assumed to be identical to the outer radius r_h .

In practice, the free aperture can be significantly smaller than the outer radius. For example, the holes can be drilled with short laser pulses in an inverse geometry [87]. Depending on the process parameters, the edges of the hole can exhibit significant chipping (shell brakes). During the experiments, holes drilled by this method² were repeatedly damaged at low power levels of a few kW. This is most likely due to the quality of the hole's edges. Improving the edges results in significantly higher damage

¹The model was implemented by Maximilian Högner and Valer Tosa. The simulations were conducted by Maximilian Högner

²These mirrors were manufactured by Dominik Esser (Fraunhofer ILT Aachen)

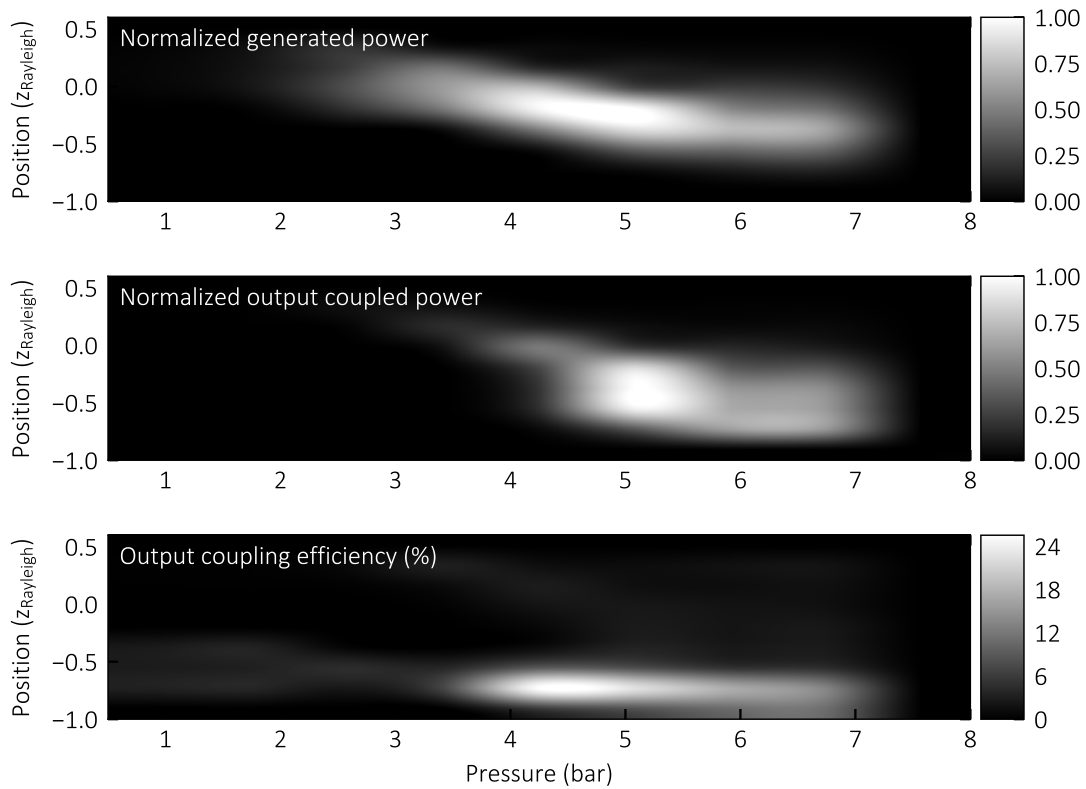


Figure 5.5 – The generated power, output coupled power, and output coupling efficiency, calculated for the following parameters: 35 μJ , 35 fs, 2.5 mm beam radius, and 88 μm hole radius, resulting in 0.5% loss. See text and references therein for details of the model.

thresholds. Here, holes drilled by the company Microon GmbH were used. Some relevant parameters can be found in [151], but due to the complex nature of the process, it is not clear which differences to the method described in [87] are crucial. One important distinction is that after breakthrough of the mirror opening, the mirrors were turned around and the mirror's edges were refined by a second drilling step. Thus, the free aperture r_{XUV} of these mirrors is significantly smaller than the outer diameter r_h . These mirrors were available with fused silica substrates and enabled the operation with 10 kW of average power. For future improvements, mirrors with a larger free aperture and in ULE for reduced thermal lensing are desired. If the free aperture could be increased to the outer diameter from 120 μm to 180 μm , the output coupling efficiency would almost double to about 10%.

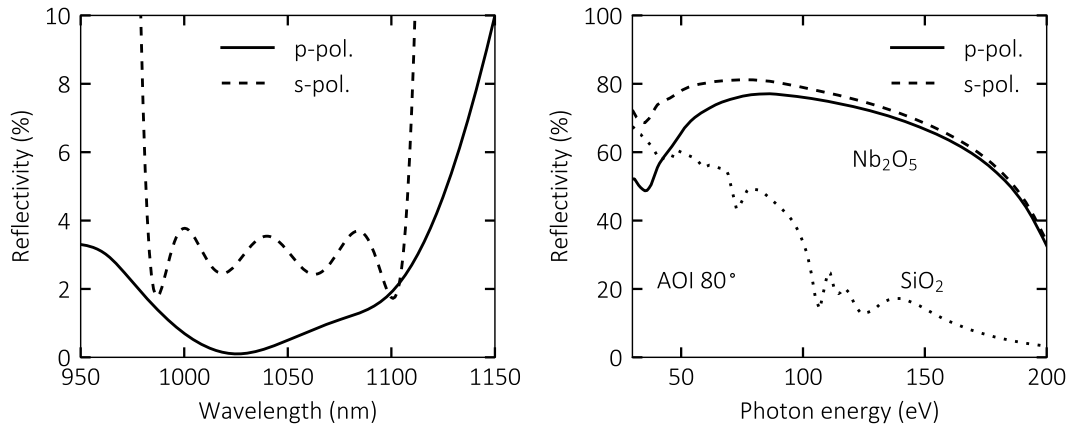


Figure 5.6 – (Left) The reflectivity of two different anti-reflective coating for an angle of incidence of 80° for s- and p-polarisation, respectively. The coatings consist of alternating layers of SiO_2 and Nb_2O_5 with the latter on top. (Right) The reflectivity of the top Nb_2O_5 layer in the XUV spectral range for an angle of incidence of 80° [148] and that of SiO_2 [155] for comparison.

5.2.3 XUV diagnostics

Not only XUV light is transmitted through the mirror opening, but also a part of the fundamental NIR radiation. This power is on the order of half of the input coupled power – in these experiments up to 100 W – which is significantly too high for thin metal filters such as aluminium and zirconium. Typically, these filters can withstand up to about 1 W of average power. This can be achieved using XUV-NIR beamsplitters consisting of an anti-reflective coating for the NIR. Such beamsplitters have been used before with SiO_2 [140, 156] or HfO_2 [86] as a top layer. However, these materials suffer from low reflectivity at high photon energies around 100 eV. Here, an alternative design using Nb_2O_5 was employed. Due to the high refractive index of Nb_2O_5 , a broadband anti-reflective coating for a bandwidth of about 100 nm can be designed, either for s- or for p-polarisation, see Fig. 5.6³. Here, the design for p-polarisation is used. It has a 135-nm thick Nb_2O_5 -layer on top. The reflectivity is plotted in the right panel of Fig. 5.6, at 100 eV it is 75%. With s-polarisation, the reflectivity is slightly better, in particular for photon energies smaller than 80 eV, but then the anti-reflection coating is worse. For comparison, the reflectivity for SiO_2 is shown.

The XUV radiation was analysed using a grazing-incidence spectrometer (McPherson 248/310G). It consists of a XUV grating that images an entrance slit onto the Rowland-circle. The spectrally dispersed radiation is measured with a XUV-CCD (Andor DO-series). This configuration allows for the measurement of many harmonic orders at the

³The beamsplitter for p-polarisation was designed and fabricated by Layertec GmbH, the one for s-polarisation was designed by Vladimir Pervak.

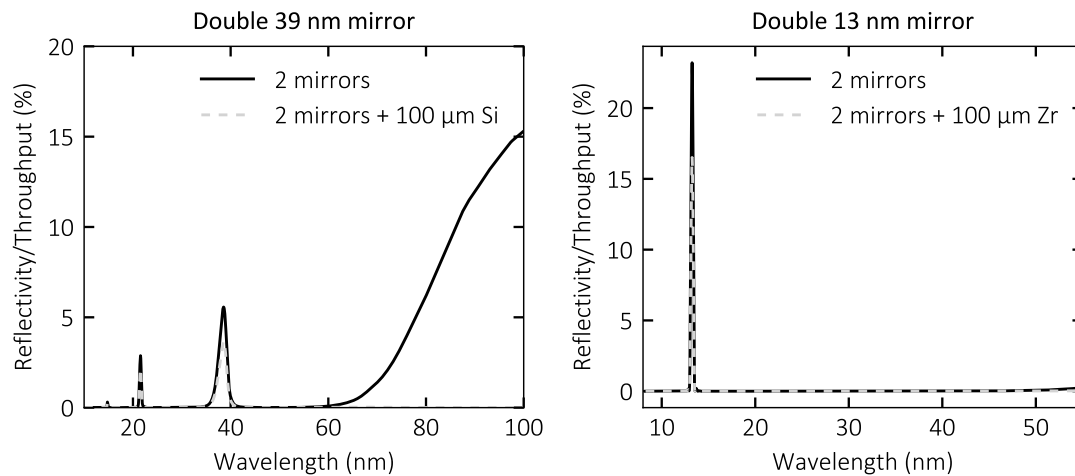


Figure 5.7 – Reflectivity curves for XUV mirrors for 39 nm and for 13 nm. The reflected radiation for wavelengths longer than 60 nm can be filtered using a silicon filter. The 13-nm mirror is used in conjunction with zirconium filters, which attenuates any light for $\lambda > 20$ nm.

same time, but does not allow for a reliable estimation of the output coupled power, because it is not known how much power is clipped at the entrance slit. Instead, the XUV beam can be directed onto a photodiode (IRD AXUV100, with optional aluminium coating). From the generated photo-current, the power can be calculated from the photodiode's sensitivity. When a spectrum is recorded with the same parameters, the power in each harmonic order can be estimated from the relative signal strength in the spectrum. Alternatively, a single harmonic order can be filtered using narrow band mirrors in the XUV⁴, see Fig. 5.7. The spectrally filtered beam can then be directed either onto the photodiode or onto the XUV-CCD. Both schemes allow for an estimation of the power, as the sensitivities are known and the beam is not clipped.

5.3 Experimental results

In a first experiment, the compressed pulses were enhanced in a 4.8-m long cavity with 600-mm focusing to an average power of 20 kW. In this configuration without a pierced mirror, stable long-term operation was possible without damage issues. The incident and circulating spectrum are shown in Fig. 5.8 along with a measured cavity autocorrelation. The intracavity pulse duration was 30 fs.

High harmonics were generated in xenon, argon and neon. Due to their different ionisation potential and different driving intensities, the generated wavelengths span a wide range, of which 11 nm–70 nm (18 eV–110 eV) were detected. The spectra are

⁴These mirrors were designed and fabricated by Alexander Guggenmos.

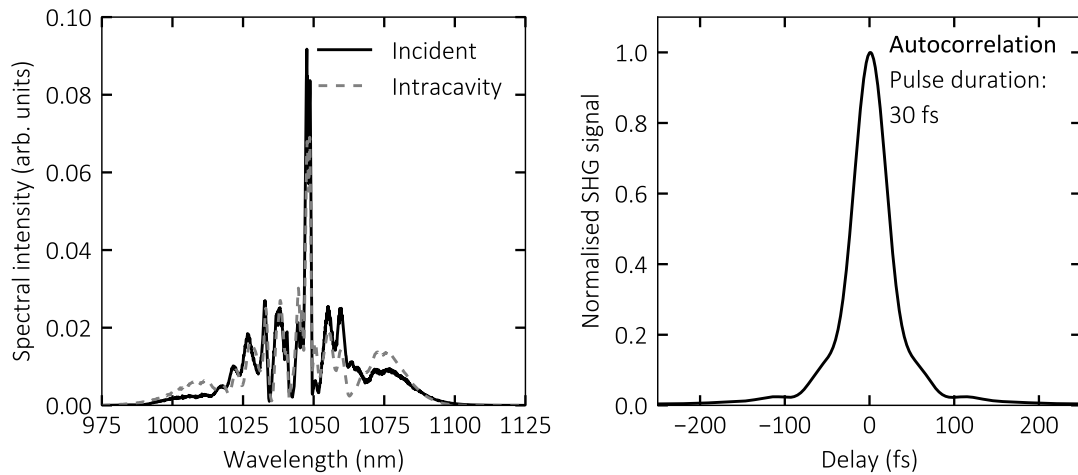


Figure 5.8 – (Left) The reflectivity of two different anti-reflective coating for an angle of incidence of 80° for s- and p-polarisation, respectively. The coatings consist of alternating layers of SiO_2 and Nb_2O_5 with the latter on top. (Right) The reflectivity of the top Nb_2O_5 layer in the XUV spectral range for an angle of incidence of 80° [148] and that of SiO_2 [155] for comparison.

shown in Fig. 5.9. Each spectrum is calibrated to the power directly behind the pierced mirror.

The neon spectrum was obtained using a bow-tie cavity with $R = 200$ mm and $L = 3600$ mm, i.e. three circulating pulses. The pulses were focused to a $10 \mu\text{m} \times 18 \mu\text{m}$ focus resulting in a peak intensity of $3 \times 10^{14} \text{ W/cm}^2$ at an average power of 10 kW. The beam on the mirrors is $1.8 \text{ mm} \times 3.3 \text{ mm}$, see Fig. 5.11. The generated radiation from 11 nm to about 35 nm cannot be filtered using a single material. Instead, for the high photon energies a zirconium filter was used, which transmits XUV radiation for $\lambda < 20$ nm. For $\lambda > 17$ nm, aluminium can be used. In the lower panel of Fig. 5.9 spectra with each filter are shown. The power was measured with identical conditions using the previously described narrow band mirrors at 95 eV (H79). Both spectra were then normalised to match the power at 95 eV. For H79 the measured power was 1.3 nW corresponding to 9×10^7 photons/s. Here, a nozzle with an opening diameter of $100 \mu\text{m}$ and 11 bar of backing pressure was used. From numerical simulation, a 200- μm long gas target with a density 5 times that at room temperature is estimated. The output coupled power is improved by more than two orders of magnitude over previous results at MHz-repetition-rate [86]. For frequency comb spectroscopy, this would correspond to 500 times more power per comb mode, as the repetition rate was also three times higher than in [86].

The output coupling efficiency in this configuration is estimated to be smaller than 5% from numerical simulations, see Section 5.2.2. The pierced mirror has a free aperture of

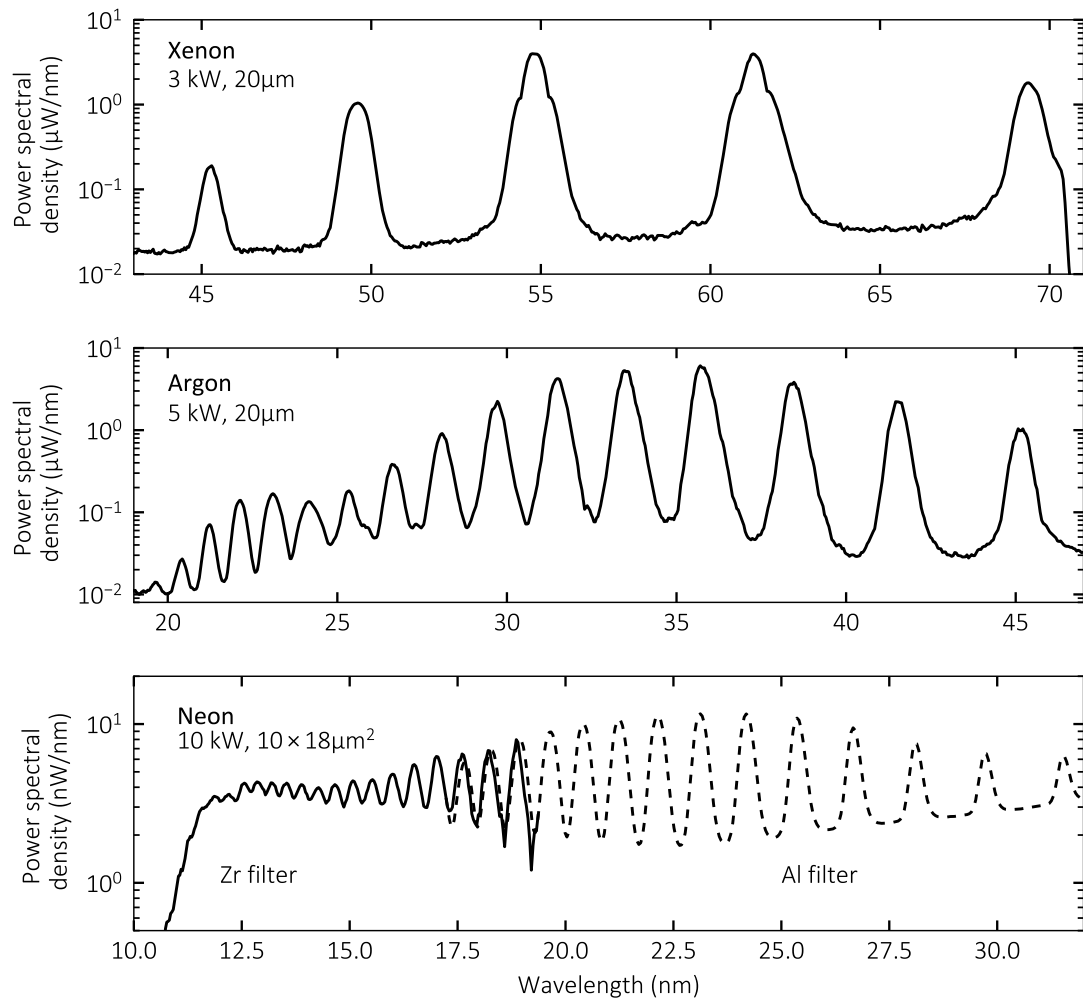


Figure 5.9 – XUV spectra obtained from high-harmonic generation in xenon, argon, and neon. See text for details.

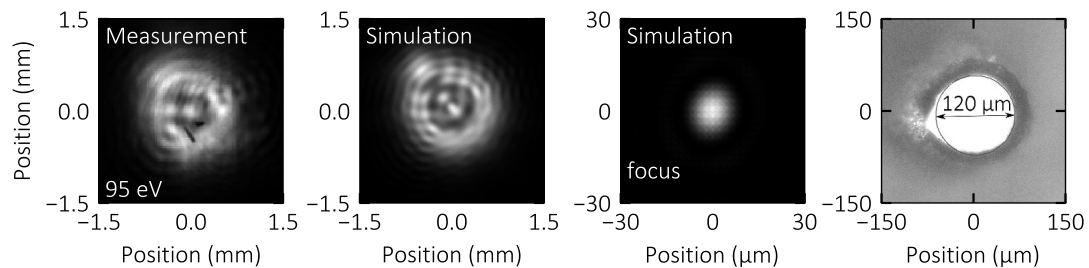


Figure 5.10 – From left to right: Measured beam profile at 95 eV filtered using two narrow-band XUV mirrors, detected with a XUV-CCD. Simulated beam profile obtained from clipping a spherical wave at the mirror opening. Simulated focus obtained by focusing with $f = 50$ mm. The free aperture of the pierced mirror with an opening diameter of 120 μm.

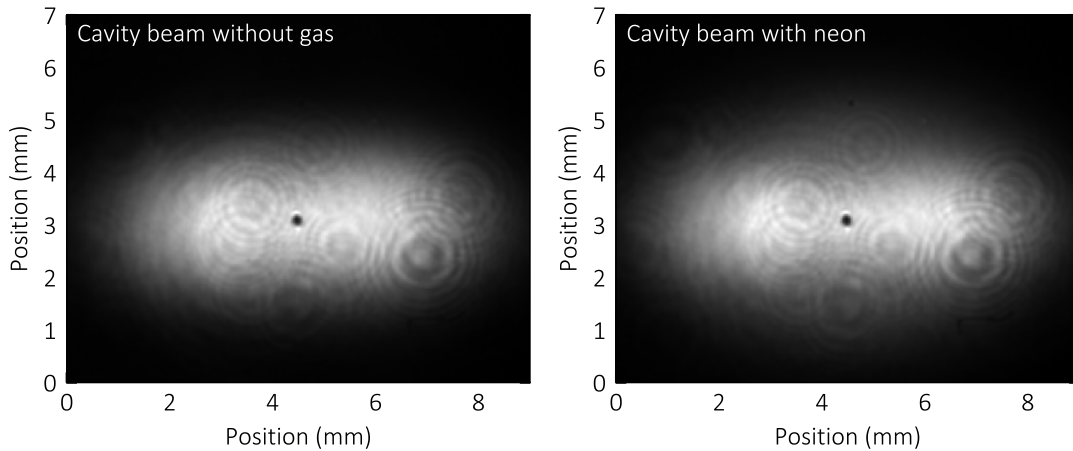


Figure 5.11 – The cavity beam on the pierced mirror without (left) gas and with neon (right). Plasma lensing leads to coupling into higher order modes, as is visible in particular in the vertical axis.

120 μm and an outer diameter of 180 μm resulting in losses of 0.4%. If the free aperture was 180 μm as well, the output coupling efficiency would almost double.

In Fig. 5.10 the measured beamprofile at 95 eV is shown. The structure is due to diffraction at the mirror opening, which is also depicted. It can be simulated by assuming a point source in the cavity focus, which is propagated for $d = 100$ mm and then clipped at the pierced mirror according to the microscope picture. In other words: At the pierced mirror, the beam in the simulation has an infinite extension and a phase front curvature of $R = 100$ mm. After clipping, the beam is propagated using the Fresnel-formula for $d = 1400$ mm, which is the distance between the pierced mirror and the CCD. Fig. 5.10 also shows a simulation of the focused XUV beam using a $f = 50$ mm focusing element.

In Fig. 5.9 spectra obtained with argon and xenon are shown. The power per harmonic in the plateau is on the μW -level, e.g. 4 μW at 40 nm with argon. This is about the same as in [86] (5 μW at 40 nm) with the same output coupling technique and comparable output coupling efficiency, but here with shorter pulses (30 fs instead of 60 fs), higher NIR power (5 kW instead of 3.4 kW), and a lower finesse (150 instead of 600). The only explanation, why the flux could not be improved is the cumulative plasma, which is expected to be significantly higher at 250 MHz than at 80 MHz.

In order to test the impact of the cumulative plasma on the conversion efficiency, a mixture of helium of xenon was compared to pure xenon. This was done by mixing the gas flows from two separate bottles at equal pressure, see Fig. 5.12. The amount of helium flow was regulated by hand with a valve. The overall flow of the mixture was regulated with a second valve. With this proof-of-concept scheme, the harmonic flux using xenon was improved by 30%. The reason for this is the increased particle speed of the helium-xenon mixture compared to pure xenon, as helium is much lighter (4 u) than

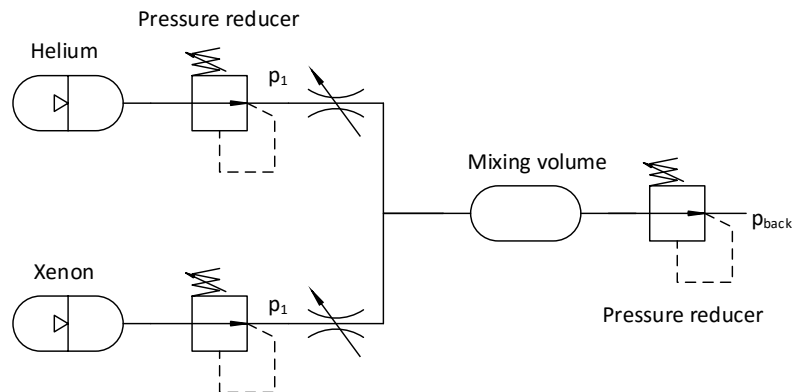


Figure 5.12 – Apparatus for mixing the gas flow of xenon and helium. The gases are mixed at equal pressure p_1 using two valves into a mixing volume. The pressure of the mixture is then reduced to the working pressure p_{back} .

xenon (131 u). However, using this apparatus, setting an appropriate mixture of xenon is cumbersome. Instead, one could fill a gas bottle with both gases and use the mixture from that volume. Then, also the volume ratios of the two gases are controllable. This method does not significantly accelerate light gases such as neon (20 u), but for xenon it can be used to significantly increase the XUV flux at high repetition rates.

5.4 Conclusions

A broadband (15 eV to 110 eV) pulsed XUV source based on cavity-enhanced high-harmonic generation at 250 MHz was demonstrated. The radiation was coupled out through an opening in the cavity mirror subsequent to the gas target. At 95 eV the output coupled flux was 1.3 nW or 9×10^7 photons/s in a 2% bandwidth, which constitutes an improvement of more than two orders of magnitude compared to previous results at 80 MHz repetition rate [86]. Together with a stabilized offset frequency, this would correspond to 500 times more power per comb line as the repetition rate is also three times higher than in [86]. Between 15 eV and 50 eV, the output coupled power of the harmonic radiation in argon and xenon is on the μW -level. Similar power levels have been reported before [82, 86]. For photon energies up to 20 eV, significantly higher output coupled powers were demonstrated from enhancement cavities [24, 81, 146]. This is because the pierced mirror output coupling is inefficient for low-order harmonics.

The *generated* power at the 100-eV level is comparable to that obtained from kHz single pass systems [73]. However, due to output coupling less than 5% of the generated photons can be used in an experiment. Still, it is already sufficient for PEEM experiments,

where the detection rate of the photoelectrons is limited to a few millions of electrons per second. Together with typical quantum efficiencies of 10^{-3} to 10^{-1} this yields a usable photon flux of 10^7 to 10^9 photons/s in a 10% bandwidth. Note that for the prospected experiments [29, 30], a repetition rate around 10 MHz instead of 250 MHz is desired. Provided that the same average power and the same peak intensity can be obtained in a longer cavity, an even higher photon flux is expected using the same methodology, because the cumulative plasma is weaker. Apart from a lower repetition rate, further improvements of the usable photon flux is expected from alternative output coupling schemes, e.g. quasi-imaging [77–79], non-collinear high-harmonic generation [88, 89], or grating output coupling [83]. The technique must be chosen to fit the specific requirements of one of the manifold applications enabled by cavity-enhanced high-harmonic sources.

When the same intensity with an optimised gas target can be obtained in an enhancement cavity, e.g. using specially designed mirrors for the nonlinear interaction (see Chapter 6), the generated power will be higher by a factor equal to the power enhancement compared to a single-pass system operating at the same repetition rate. Simulations revealed a possible power enhancement of about 50 for this situation [151]. Even with a standard-approach cavity, the clamping law [63] predicts, for example, an intracavity intensity of 7×10^{13} W/cm² for a finesse of 200 and optimised xenon gas jet. According to Fig. 5.2, this should allow for a generation efficiency, which is within a factor of 3 for single-pass experiments at 30 fs, while the power enhancement can be 100 in this case. However, this is only true if the cumulative plasma has little influence on the efficiency, which should be the case for repetition rates around 10 MHz instead of 250 MHz.

It should be noted that photon energies exceeding 100 eV cannot be obtained at 250 MHz without an enhancement cavity due to limited pulse energy of state-of-the-art lasers at this repetition rate. Thus, such a combination of high photon energy and high repetition rate is feasible only with enhancement cavities and they even offer the prospective of increasing the photon flux for both time-domain experiments and frequency-comb spectroscopy.

CHAPTER 6

Summary & Outlook

Enhancement cavities are a mature technology with various applications ranging from spectroscopy to the generation of hard x-ray radiation. The enhancement of laser pulses to ultra high average powers is beneficial for all light-matter interactions with small cross-section, either for spectroscopy (detection) or for frequency conversion (generation). The results from this thesis have implications in particular for two of them, namely inverse-Compton scattering and cavity-enhanced high-harmonic generation. In the following, these results are summarised and further possible improvements are discussed in this respect.

6.1 Power scaling of enhancement cavities for inverse-Compton scattering

Using the methodology developed in Chapter 3, average powers of up to 400 kW with 250-fs pulses and up to 670 kW with 10-ps pulses have been demonstrated in Chapter 4 with peak intensities exceeding 10^{14} W/cm². Using 30-fs pulses an average power of 20 kW was obtained in Chapter 5. This constitutes an improvement of more than one order of magnitude over previous results [44, 82]. The achievable power is limited by both spherical and thermally induced aberrations in the cavity. For further scaling of the power and intensity, longer cavities (e.g. 10 MHz) with tight focusing may be

employed, because this reduces both the thermal sensitivity and spherical aberrations. Then, astigmatic compensation becomes indispensable, see Section 3.5. Still, thermally induced aberrations will limit the achievable average power. In Chapter 4, one mirror with an absorption of 1 ppm on a fused silica substrate was used. If this thermal lens was avoided or mitigated, powers exceeding 1 MW would come into reach. This might be possible with mirrors with an even lower absorption (for cw lasers at 1064 nm a value of 0.2 ppm has been reported [157]), by employing a grating-based reflective input coupler on a ULE substrate [138], or if superior materials such as diamond become available in the future [57, 110]. Spherical aberrations can be avoided using parabolic reflectors [126]. However, it is yet to be demonstrated if the delicate adjustment of parabolas is possible in enhancement cavities with several kilowatt of average power.

Higher power and intensity levels are in particular important for inverse-Compton scattering based sources of coherent hard x-ray radiation [38]. For this application, power levels on the order of 1 MW are desired [40]. This power regime was demonstrated for the first time here. These apparatus are commercially available with a photon flux sufficient for many applications [158]. However, an increase of intensity and average power would directly benefit the photon flux, which is necessary for a widespread use of these apparatus. Specifically for this purpose, the thermal performance of output couplers for the generated radiation [91, 159] must be investigated and optimized if possible.

6.2 Cavity-enhanced high-harmonic generation

For high-harmonic generation the intensity is limited by phase matching conditions, see Section 5.1. In standard enhancement cavities it is furthermore limited to lower and non-ideal values due to the ionization-related intensity clamping [61–63]. Thus, for high-harmonic generation one should not (only) look at the achievable power and intensity in an empty cavity, but for optimised conditions in the gas target under consideration of the nonlinear interaction. Further progress is expected from the following improvements:

- Shorter pulses are advantageous for high-harmonic generation. They may be obtained with novel dielectric mirrors. For example, two types of slightly chirped mirrors with opposite sign may have almost zero dispersion over a bandwidth of 260 nm enabling pulses as short as 15 fs [151].
- The transmission and phase of the input coupler can be optimized for the nonlinear interaction, possibly allowing for higher intensities despite the ionization induced phase shift [63].
- In this thesis, cumulative plasma effects were shown to have detrimental influence on the conversion efficiency. The cumulative effects are less pronounced at lower

repetition rates, so that long cavities of about 10 MHz can be employed for improved XUV photon flux. In order to have a high-power seeding laser at this repetition rate with pulses shorter than 20 fs, novel pulse compression schemes must be employed [160–162].

- For frequency comb spectroscopy, often the power per comb mode should be optimized. For this, a quantitative understanding of the impact of cumulative effects is crucial. Using a pulse picker, the photon flux can be measured as a function of the repetition rate at otherwise identical parameters (pulse energy, pulse duration, focusing, gas jet) enabling the development of an empirical law.
- Output coupling techniques such as quasi-imaging [78, 79], nanograting [83, 84], and noncollinear HHG [88, 89] may exhibit superior output coupling efficiency, but they are yet to be demonstrated with enhancement cavities for high photon energies.
- With shorter pulses, even gating for the generation of isolated attosecond pulses comes into reach, e.g. by noncollinear optical gating [89] or polarisation gating [163, 164].
- The cutoff in high-harmonic generation may be extended using longer driving wavelengths [17, 18], e.g. implemented with high-power thulium fibre lasers operating at 2 μm which are currently emerging [165, 166].

The photon flux demonstrated in Chapter 5 at 95 eV is already sufficient for PEEM experiments. For such an experiment a repetition rate of not more than 40 MHz should be used in order to avoid the mistake of successive pulse's signals. With the aforementioned compression schemes in Kagome fibres or bulk [160–162] and improved quality of the pierced mirrors, an average power of more than 10 kW with 30-fs pulses is possible at 40 MHz inside an enhancement cavity. Then, the cumulative effects are much weaker compared to the 250-MHz experiment, resulting in an even higher photon flux. In conjunction with gating for the generation of isolated attosecond pulses, these techniques may be used for the implementation of an attoPEEM apparatus [29] at MHz repetition rate. In such an experiment, the photoelectrons emitted by 91 eV photons leave nanostructures extending 1 nm within 180 as, enabling measurements down to that time resolution. Larger structures may be investigated with femtosecond time resolution with the pulse parameters already demonstrated in this thesis.

Bibliography

- [1] L. Garwin and T. Lincoln, eds., *A century of nature: Twenty-one discoveries that changed science and the world* (University of Chicago Press, Chicago, 2003).
- [2] F. Zernike, “How I Discovered Phase Contrast”, *Science* **121**, 345–349 (1955).
- [3] Marvin Minsky, “Microscopy apparatus”, US3013467 A (7. Nov. 1957).
- [4] J. B. Pawley, ed., *Handbook of biological confocal microscopy*, 3. ed. (Springer, New York, NY, 2006).
- [5] T. W. Hänsch, “Nobel Lecture: Passion for precision”, *Reviews of Modern Physics* **78**, 1297–1309 (2006).
- [6] T. Udem, R. Holzwarth, and T. W. Hänsch, “Optical frequency metrology”, *Nature* **416**, 233–237 (2002).
- [7] P. Cloetens, R. Barrett, J. Baruchel, J.-P. Guigay, and M. Schlenker, “Phase objects in synchrotron radiation hard x-ray imaging”, *Journal of Physics D: Applied Physics* **29**, 133 (1999).
- [8] R. Fitzgerald, “Phase-Sensitive X-Ray Imaging”, *Physics Today* **53**, 23 (2000).
- [9] A. Momose, “Phase-sensitive imaging and phase tomography using X-ray interferometers”, *Optics Express* **11**, 2303 (2003).
- [10] M. Herrmann, M. Haas, U. D. Jentschura, F. Kottmann, D. Leibfried, G. Saathoff, C. Gohle, A. Ozawa, V. Batteiger, S. Knünz, N. Kolachevsky, H. A. Schüssler, T. W. Hänsch, and T. Udem, “Feasibility of coherent XUV spectroscopy on the 1S–2S transition in singly ionized helium”, *Physical Review A* **79** (2009).
- [11] F. Krausz and M. Ivanov, “Attosecond physics”, *Reviews of Modern Physics* **81**, 163–234 (2009).
- [12] A. Einstein, “Zur Quantentheorie der Strahlung”, *Physikalische Zeitschrift* **18** (1917).

- [13] C. Jauregui, J. Limpert, and A. Tünnermann, “High-power fibre lasers”, *Nature Photonics* **7**, 861–867 (2013).
- [14] H. Fattahi et al., “Third-generation femtosecond technology”, *Optica* **1**, 45 (2014).
- [15] P. Russbuedt, D. Hoffmann, M. Hofer, J. Lohring, J. Luttmann, A. Meissner, J. Weitenberg, M. Traub, T. Sartorius, D. Esser, R. Wester, P. LOOSEN, and R. Poprawe, “Innoslab Amplifiers”, *IEEE Journal of Selected Topics in Quantum Electronics* **21**, 447–463 (2015).
- [16] X. F. Li, A. L’Huillier, M. Ferray, L. A. Lompré, and G. Mainfray, “Multiple-harmonic generation in rare gases at high laser intensity”, *Physical Review A* **39**, 5751–5761 (1989).
- [17] P. B. Corkum, “Plasma perspective on strong field multiphoton ionization”, *Physical review letters* **71**, 1994 (1993).
- [18] M. Lewenstein, P. Balcou, M. Ivanov, A. L’Huillier, and P. Corkum, “Theory of high-harmonic generation by low-frequency laser fields”, *Physical Review A* **49**, 2117–2132 (1994).
- [19] T. Popmintchev, M.-C. Chen, D. Popmintchev, P. Arpin, S. Brown, S. Alisauskas, G. Andriukaitis, T. Balciunas, O. D. Mucke, A. Pugzlys, A. Baltuska, B. Shim, S. E. Schrauth, A. Gaeta, C. Hernandez-Garcia, L. Plaja, A. Becker, A. Jaron-Becker, M. M. Murnane, and H. C. Kapteyn, “Bright Coherent Ultrahigh Harmonics in the keV X-ray Regime from Mid-Infrared Femtosecond Lasers”, *Science* **336**, 1287–1291 (2012).
- [20] C. Spielmann, N. H. Burnett, S. Sartania, R. Koppitsch, M. Schnürer, C. Kan, M. Lenzner, P. Wobrauschek, and F. Krausz, “Generation of Coherent X-rays in the Water Window Using 5-Femtosecond Laser Pulses”, *Science* **278**, 661–664 (1997).
- [21] E. Goulielmakis, M. Schultze, M. Hofstetter, V. S. Yakovlev, J. Gagnon, M. Uiberacker, A. L. Aquila, E. M. Gullikson, D. T. Attwood, R. Kienberger, F. Krausz, and U. Kleineberg, “Single-Cycle Nonlinear Optics”, *Science* **320**, 1614–1617 (2008).
- [22] K. Zhao, Q. Zhang, M. Chini, Y. Wu, X. Wang, and Z. Chang, “Tailoring a 67 attosecond pulse through advantageous phase-mismatch”, *Optics Letters* **37**, 3891 (2012).
- [23] T. Brabec and F. Krausz, “Intense few-cycle laser fields: Frontiers of nonlinear optics”, *Reviews of Modern Physics* **72**, 545–591 (2000).

- [24] A. Cingöz, D. C. Yost, T. K. Allison, A. Ruehl, M. E. Fermann, I. Hartl, and J. Ye, “Direct frequency comb spectroscopy in the extreme ultraviolet”, *Nature* **482**, 68–71 (2012).
- [25] Z.-C. Yan, W. Nörtershäuser, and G. W. F. Drake, “High Precision Atomic Theory for Li and Be+: QED Shifts and Isotope Shifts”, *Physical Review Letters* **100**, 243002 (2008).
- [26] C. J. Campbell, A. G. Radnaev, and Kuzmich A., “Wigner Crystals of ^{229}Th for Optical Excitation of the Nuclear Isomer”, *Physical Review Letters* **106**, 223001 (2011).
- [27] A. D. Panov, “Quantitative conversion spectroscopy of the ultrasoft isomeric transition of uranium-235 and the electronic structure of uranium oxides”, *Journal of Experimental and Theoretical Physics* **85**, 313–324 (1997).
- [28] S. Passlack, S. Mathias, O. Andreyev, D. Mittnacht, M. Aeschlimann, and M. Bauer, “Space charge effects in photoemission with a low repetition, high intensity femtosecond laser source”, *Journal of Applied Physics* **100**, 24912 (2006).
- [29] M. I. Stockman, M. F. Kling, U. Kleineberg, and F. Krausz, “Attosecond nanoplasmonic-field microscope”, *Nature Photonics* **1**, 539–544 (2007).
- [30] S. H. Chew, F. Süßmann, C. Späth, A. Wirth, J. Schmidt, S. Zharebtsov, A. Guggenmos, A. Oelsner, N. Weber, J. Kapaldo, A. Gliserin, M. I. Stockman, M. F. Kling, and U. Kleineberg, “Time-of-flight-photoelectron emission microscopy on plasmonic structures using attosecond extreme ultraviolet pulses”, *Applied Physics Letters* **100**, 51904 (2012).
- [31] T. Rohwer, S. Hellmann, M. Wiesenmayer, C. Sohr, A. Stange, B. Slomski, A. Carr, Y. Liu, L. M. Avila, M. Källäne, S. Mathias, L. Kipp, K. Rossnagel, and M. Bauer, “Collapse of long-range charge order tracked by time-resolved photoemission at high momenta”, *Nature* **471**, 490–493 (2011).
- [32] J. Ullrich, R. Moshhammer, A. Dorn, R. Dörner, L. P. H. Schmidt, and H. Schmidt-Böcking, “Recoil-ion and electron momentum spectroscopy: reaction-microscopes”, *Reports on Progress in Physics* **66**, 1463 (2003).
- [33] C. Gohle, T. Udem, M. Herrmann, J. Rauschenberger, R. Holzwarth, H. A. Schuessler, F. Krausz, and T. W. Hänsch, “A frequency comb in the extreme ultraviolet”, *Nature* **436**, 234–237 (2005).
- [34] R. J. Jones, K. D. Moll, M. J. Thorpe, and J. Ye, “Phase-coherent frequency combs in the vacuum ultraviolet via high-harmonic generation inside a femtosecond enhancement cavity”, *Physical Review Letters* **94**, 193201 (2005).

- [35] A. K. Mills, T. J. Hammond, Lam, Matthew H C, and D. J. Jones, “XUV frequency combs via femtosecond enhancement cavities”, *Journal of Physics B: Atomic, Molecular and Optical Physics* **45**, 142001 (2012).
- [36] A. Börzsönyi, R. Chiche, E. Cormier, R. Flaminio, P. Jojart, C. Michel, K. Osvay, L. Pinard, V. Soskov, A. Variola, and F. Zomer, “External cavity enhancement of picosecond pulses with 28,000 cavity finesse”, *Applied Optics* **52**, 8376 (2013).
- [37] W. J. Brown and F. V. Hartemann, “Three-dimensional time and frequency-domain theory of femtosecond x-ray pulse generation through Thomson scattering”, *Physical Review Special Topics - Accelerators and Beams* **7** (2004).
- [38] Z. Huang and R. D. Ruth, “Laser-Electron Storage Ring”, *Physical Review Letters* **80**, 976–979 (1998).
- [39] J. Riffkin, R. J. Loewen, and R. D. Ruth, “APPARATUS, SYSTEM, AND METHOD FOR HIGH FLUX, COMPACT COMPTON X-RAY SOURCE”, US 7,277,526 B2 (2007).
- [40] W. S. Graves, W. Brown, F. X. Kaertner, and D. E. Moncton, “MIT inverse Compton source concept”, *Compton sources for X/gamma rays: Physics and applications* **608**, S103–S105 (2009).
- [41] A. Variola, J. Brasile, C. Bruni, R. Chehab, R. Chiche, R. Cizeron, F. Couchot, Y. Fedala, J. Haissinski, M. Jacquet, D. Jehanno, M. Lacroix, P. Lepercq, B. Mouton, R. Roux, V. Soskov, A. Vivoli, and F. Zomer, “The LAL Compton program”, *Nuclear Instruments and Methods in Physics Research Section A: Accelerators, Spectrometers, Detectors and Associated Equipment* **608**, S83–S86 (2009).
- [42] H. Carstens, S. Holzberger, J. Kaster, J. Weitenberg, V. Pervak, A. Apolonski, E. Fill, F. Krausz, and I. Pupeza, “Large-mode enhancement cavities”, *Optics Express* **21**, 11606 (2013).
- [43] H. Carstens, N. Lilienfein, S. Holzberger, C. Jocher, T. Eidam, J. Limpert, A. Tünnermann, J. Weitenberg, D. C. Yost, A. Alghamdi, Z. Alahmed, A. Azzeer, A. Apolonski, E. Fill, F. Krausz, and I. Pupeza, “Megawatt-scale average-power ultrashort pulses in an enhancement cavity”, *Optics Letters* **39**, 2595 (2014).
- [44] I. Pupeza, T. Eidam, J. Rauschenberger, B. Bernhardt, A. Ozawa, E. Fill, A. Apolonski, T. Udem, J. Limpert, Z. A. Alahmed, A. M. Azzeer, A. Tünnermann, T. W. Hänsch, and F. Krausz, “Power scaling of a high-repetition-rate enhancement cavity”, *Optics Letters* **35**, 2052–2054 (2010).
- [45] H. Carstens, M. Högner, T. Saule, S. Holzberger, N. Lilienfein, A. Guggenmos, C. Jocher, T. Eidam, D. Esser, V. Tosa, V. Pervak, J. Limpert, A. Tünnermann, U. Kleineberg, F. Krausz, and I. Pupeza, “High-harmonic generation at 250 MHz with photon energies exceeding 100 eV”, *Optica* **3**, 366 (2016).

- [46] A. E. Siegman, *Lasers*, 5th ed. (Univ. Science Books, Mill Valley and Calif, 1986).
- [47] W. G. Nagourney, *Quantum electronics for atomic physics*, Oxford graduate texts (Oxford University Press, Oxford, 2010).
- [48] H. Kogelnik and T. Li, “Laser beams and resonators”, *Proceedings of the IEEE* **54**, 1312–1329 (1966).
- [49] S. Gigan, L. Lopez, N. Treps, A. Maître, and C. Fabre, “Image transmission through a stable paraxial cavity”, *Physical Review A* **72**, 23804 (2005).
- [50] A. Gerrard and J. M. Burch, *Introduction to matrix methods in optics*, Wiley series in pure and applied optics (Wiley, London u.a, 1975).
- [51] J. A. Arnaud, “Degenerate Optical Cavities”, *Applied Optics* **8**, 189–195 (1969).
- [52] J. A. Arnaud, “Degenerate Optical Cavities. II: Effect of Misalignments”, *Applied Optics* **8**, 1909–1917 (1969).
- [53] S. de Silvestri, P. Laporta, and V. Magni, “Rod thermal lensing effects in solid-state laser ring resonators”, *Optics Communications* **65**, 373–376 (1988).
- [54] J.-Y. Vinet, “Reducing thermal effects in mirrors of advanced gravitational wave interferometric detectors”, *Classical and Quantum Gravity* **24**, 3897–3910 (2007).
- [55] P. Hello and J.-Y. Vinet, “Analytical models of thermal aberrations in massive mirrors heated by high power laser beams”, *Journal de Physique* **51**, 1267–1282 (1990).
- [56] P. Hello and J.-Y. Vinet, “Analytical models of transient thermoelastic deformations of mirrors heated by high power cw laser beams”, *Journal de Physique* **51**, 2243–2261 (1990).
- [57] W. Winkler, K. Danzmann, A. Rüdiger, and R. Schilling, “Heating by optical absorption and the performance of interferometric gravitational-wave detectors”, *Physical Review A* **44**, 7022–7036 (1991).
- [58] Perelomov, Popov, and Terent’ev, “IONIZATION OF ATOMS IN AN ALTERNATING ELECTRIC FIELD”, *SOVIET PHYSICS JETP* **1966**, 924–934 (1966).
- [59] M. V. Ammosov, N. B. Delone, and V. P. Krainov, “Tunnel ionization of complex atoms and of atomic ions in an alternating electromagnetic field”, *JETP* **64**, 1191 (1986).
- [60] E. Constant, D. Garzella, P. Breger, E. Mével, C. Dorrer, C. Le Blanc, F. Salin, and P. Agostini, “Optimizing high harmonic generation in absorbing gases: model and experiment”, *Physical Review Letters* **82**, 1668–1671 (1999).

- [61] T. K. Allison, A. Cingöz, D. C. Yost, and J. Ye, “Extreme nonlinear optics in a femtosecond enhancement cavity”, *Physical Review Letters* **107**, 183903 (2011).
- [62] D. R. Carlson, J. Lee, J. Mongelli, E. M. Wright, and R. J. Jones, “Intracavity ionization and pulse formation in femtosecond enhancement cavities”, *Optics Letters* **36**, 2991–2993 (2011).
- [63] S. Holzberger, N. Lilienfein, H. Carstens, T. Saule, M. Högner, F. Lücking, M. Trubetskov, V. Pervak, T. Eidam, J. Limpert, A. Tünnermann, E. Fill, F. Krausz, and I. Pupeza, “Femtosecond Enhancement Cavities in the Nonlinear Regime”, *Physical Review Letters* **115**, 023902 (2015).
- [64] A.-T. Le, T. Morishita, and C. D. Lin, “Improved Lewenstein model for high-order harmonic generation of atoms and molecules with scattering wavefunctions”, *Arxiv*, 0707.4192 (2007).
- [65] T. Morishita, A.-T. Le, Z. Chen, and C. D. Lin, “Accurate retrieval of structural information from laser-induced photoelectron and high-order harmonic spectra by few-cycle laser pulses”, *Physical review letters* **100**, 013903 (2008).
- [66] S. Kazamias, S. Daboussi, O. Guilbaud, K. Cassou, D. Ros, B. Cros, and G. Maynard, “Pressure-induced phase matching in high-order harmonic generation”, *Physical Review A* **83**, 063405 (2011).
- [67] C. M. Heyl, J. Güdde, A. L’Huillier, and U. Höfer, “High-order harmonic generation with μJ laser pulses at high repetition rates”, *Journal of Physics B: Atomic, Molecular and Optical Physics* **45**, 74020 (2012).
- [68] P. Salières, A. L’Huillier, and M. Lewenstein, “Coherence Control of High-Order Harmonics”, *Physical Review Letters* **74**, 3776–3779 (1995).
- [69] M. Gaarde, F. Salin, E. Constant, P. Balcou, K. Schafer, K. Kulander, and A. L’Huillier, “Spatiotemporal separation of high harmonic radiation into two quantum path components”, *Physical Review A* **59**, 1367–1373 (1999).
- [70] T. Popmintchev, M.-C. Chen, A. Bahabad, M. Gerrity, P. Sidorenko, O. Cohen, I. P. Christov, M. M. Murnane, and H. C. Kapteyn, “Phase matching of high harmonic generation in the soft and hard X-ray regions of the spectrum”, *Proceedings of the National Academy of Sciences of the United States of America* **106**, 10516–10521 (2009).
- [71] A. Paul, E. A. Gibson, X. Zhang, A. Lytle, T. Popmintchev, X. Zhou, M. M. Murnane, I. P. Christov, and H. C. Kapteyn, “Phase-Matching Techniques for Coherent Soft X-Ray Generation”, *IEEE Journal of Quantum Electronics* **42**, 14–26 (2006).

- [72] J. Rothhardt, M. Krebs, S. Hädrich, S. Demmler, J. Limpert, and A. Tünnermann, “Absorption-limited and phase-matched high harmonic generation in the tight focusing regime”, *New Journal of Physics* **16**, 33022 (2014).
- [73] J. Rothhardt, S. Hädrich, A. Klenke, S. Demmler, A. Hoffmann, T. Gotschall, T. Eidam, M. Krebs, J. Limpert, and A. Tünnermann, “53 W average power few-cycle fiber laser system generating soft x rays up to the water window”, *Optics Letters* **39**, 5224–5227 (2014).
- [74] N. Lilienfein, H. Carstens, S. Holzberger, C. Jocher, T. Eidam, J. Limpert, A. Tünnermann, A. Apolonski, F. Krausz, and I. Pupeza, “Balancing of thermal lenses in enhancement cavities with transmissive elements”, *Optics letters* **40**, 843–846 (2015).
- [75] R. M. Wood, *Laser-induced damage of optical materials*, Series in optics and optoelectronics (Institute of Physics, Bristol, 2003).
- [76] S. J. Habraken and G. Nienhuis, “Modes of a twisted optical cavity”, *Physical Review A* **75**, 033819 (2007).
- [77] J. Weitenberg, P. Rußbüldt, T. Eidam, and I. Pupeza, “Transverse mode tailoring in a quasi-imaging high-finesse femtosecond enhancement cavity”, *Optics Express* **19**, 9551–9561 (2011).
- [78] J. Weitenberg, P. Rußbüldt, I. Pupeza, T. Udem, H.-D. Hoffmann, and R. Poprawe, “Geometrical on-axis access to high-finesse resonators by quasi-imaging: a theoretical description”, *Journal of Optics* **17**, 25609 (2015).
- [79] I. Pupeza, M. Högner, J. Weitenberg, S. Holzberger, D. Esser, T. Eidam, J. Limpert, A. Tünnermann, E. Fill, and V. S. Yakovlev, “Cavity-Enhanced High-Harmonic Generation with Spatially Tailored Driving Fields”, *Physical Review Letters* **112** (2014).
- [80] D. N. Schimpf, J. Schulte, W. P. Putnam, and F. X. Kärtner, “Generalizing higher-order Bessel-Gauss beams: analytical description and demonstration”, *Optics express* **20**, 26852–26867 (2012).
- [81] J. Lee, D. R. Carlson, and R. J. Jones, “Optimizing intracavity high harmonic generation for XUV fs frequency combs”, *Optics Express* **19**, 23315–23326 (2011).
- [82] D. C. Yost, A. Cingöz, T. K. Allison, A. Ruehl, M. E. Fermann, I. Hartl, and J. Ye, “Power optimization of XUV frequency combs for spectroscopy applications [Invited]”, *Optics Express* **19**, 23483–23493 (2011).
- [83] D. C. Yost, T. R. Schibli, and J. Ye, “Efficient output coupling of intracavity high-harmonic generation”, *Optics Letters* **33**, 1099 (2008).

- [84] Y.-Y. Yang, F. Süßmann, S. Zherebtsov, I. Pupeza, J. Kaster, D. Lehr, H.-J. Fuchs, E.-B. Kley, E. Fill, X.-M. Duan, Z.-S. Zhao, F. Krausz, S. L. Stebbings, and M. F. Kling, “Optimization and characterization of a highly-efficient diffraction nanograting for MHz XUV pulses”, *Optics express* **19**, 1954–1962 (2011).
- [85] D. C. Yost, “Development of an Extreme Ultraviolet Frequency Comb for Precision Spectroscopy”, PhD Thesis (University of Colorado, Boulder, 2011).
- [86] I. Pupeza, S. Holzberger, T. Eidam, H. Carstens, D. Esser, J. Weitenberg, P. Rußbüldt, J. Rauschenberger, J. Limpert, T. Udem, A. Tünnermann, T. W. Hänsch, A. Apolonski, F. Krausz, and E. Fill, “Compact high-repetition-rate source of coherent 100 eV radiation”, *Nature Photonics* **7**, 608–612 (2013).
- [87] D. Esser, J. Weitenberg, W. Bröring, I. Pupeza, S. Holzberger, and H.-D. Hoffmann, “Laser-manufactured mirrors for geometrical output coupling of intracavity-generated high harmonics”, *Optics Express* **21**, 26797 (2013).
- [88] A. Ozawa, A. Vernaleken, W. Schneider, I. Gotlibovych, T. Udem, and T. W. Hänsch, “Non-collinear high harmonic generation: a promising outcoupling method for cavity-assisted XUV generation”, *Optics Express* **16**, 6233–6239 (2008).
- [89] C. M. Heyl, S. N. Bengtsson, S. Carlström, J. Mauritsson, C. L. Arnold, and A. L’Huillier, “Noncollinear optical gating”, *New Journal of Physics* **16**, 52001 (2014).
- [90] J. Bonis, R. Chiche, R. Cizeron, M. Cohen, E. Cormier, P. Cornebise, N. Delerue, R. Flaminio, D. Jehanno, F. Labaye, M. Lacroix, R. Marie, B. Mercier, C. Michel, Y. Peinaud, L. Pinard, C. Prevost, V. Soskov, A. Variola, and F. Zomer, “Non-planar four-mirror optical cavity for high intensity gamma ray flux production by pulsed laser beam Compton scattering off GeV-electrons”, *Journal of Instrumentation* **7**, P01017 (2012).
- [91] R. J. Loewen, J. Riffkin, and R. D. Ruth, “X-RAY TRANSMISSIVE OPTICAL MIRROR APPARATUS”, US 7,242,748 B2 (2007).
- [92] R. J. Loewen, “A Compact Light Source: Design and Technical Feasibility Study of a Laser-Electron Storage Ring X-Ray Source”, PhD thesis (Stanford University, Stanford, 2003).
- [93] T. Heupel, M. Weitz, and T. W. Hänsch, “Phase-coherent light pulses for atom optics and interferometry”, *Optics Letters* **22**, 1719 (1997).
- [94] S. Breitkopf, T. Eidam, A. Klenke, L. von Grafenstein, H. Carstens, S. Holzberger, E. Fill, T. Schreiber, F. Krausz, A. Tünnermann, I. Pupeza, and J. Limpert, “A concept for multiterawatt fibre lasers based on coherent pulse stacking in passive cavities”, *Light: Science & Applications* **3**, e211 (2014).

- [95] G. Mourou, B. Brocklesby, T. Tajima, and J. Limpert, “The future is fibre accelerators”, *Nature Photonics* **7**, 258–261 (2013).
- [96] T. Eidam, J. Rothhardt, F. Stutzki, F. Jansen, S. Hädrich, H. Carstens, C. Jau-regui, J. Limpert, and A. Tünnermann, “Fiber chirped-pulse amplification system emitting 3.8 GW peak power”, *Optics express* **19**, 255–260 (2011).
- [97] T. Eidam, S. Hanf, E. Seise, T. V. Andersen, T. Gabler, C. Wirth, T. Schreiber, J. Limpert, and A. Tünnermann, “Femtosecond fiber CPA system emitting 830 W average output power”, *Optics Letters* **35**, 94–96 (2010).
- [98] N. Hodgson and H. Weber, “Misalignment sensitivity of stable resonators in multimode operation”, *Journal of Modern Optics* **39**, 1873–1882 (1992).
- [99] R. Hauck, H. P. Kortz, and H. Weber, “Misalignment sensitivity of optical resonators”, *Applied Optics* **19**, 598–601 (1980).
- [100] W. B. Joyce and B. C. DeLoach, “Alignment of Gaussian beams”, *Applied Optics* **23**, 4187–4196 (1984).
- [101] F. Kawazoe, R. Schilling, and H. Lück, “Eigenmode changes in a misaligned triangular optical cavity”, *Journal of Optics* **13**, 55504 (2011).
- [102] A. Fox and T. Li, “Resonant modes in a maser interferometer”, *Bell Syst. Tech. J* **40**, 453–488 (1961).
- [103] T. J. Kane and R. L. Byer, “Monolithic, unidirectional single-mode Nd:YAG ring laser”, *Optics Letters* **10**, 65–67 (1985).
- [104] R. W. P. Drever, J. L. Hall, F. V. Kowalski, J. Hough, G. M. Ford, A. J. Munley, and H. Ward, “Laser phase and frequency stabilization using an optical resonator”, *Applied Physics B: Lasers and Optics* **31**, 97–105 (1983).
- [105] E. Black, “An introduction to Pound–Drever–Hall laser frequency stabilization”, *American Journal of Physics* **69**, 79 (2001).
- [106] H. Kogelnik, E. Ippen, A. Dienes, and C. Shank, “Astigmatically compensated cavities for CW dye lasers”, *IEEE Journal of Quantum Electronics* **8**, 373–379 (1972).
- [107] W. H. Press, *Numerical recipes 3rd edition: The art of scientific computing* (Cambridge university press, 2007).
- [108] Heraeus Quarzglas, *Thermal properties of fused silica*, http://heraeus-quarzglas.com/en/quarzglas/thermalproperties/Thermal_properties.aspx.
- [109] Corning, *ULE Datasheet*, <https://www.corning.com/media/worldwide/csm/documents/D20FD2EA-7264-43DD-B544-E1CA042B486A.pdf>.

- [110] Kyburz Saphir, *Datasheet Sapphire*, http://www.kyburz-sapphire.ch/upload/content/Saphir_Material_de.pdf.
- [111] C. J. Glassbrenner and G. A. Slack, “Thermal Conductivity of Silicon and Germanium from 3°K to the Melting Point”, *Physical Review* **134**, A1058–A1069 (1964).
- [112] Y. Okada and Y. Tokumaru, “Precise determination of lattice parameter and thermal expansion coefficient of silicon between 300 and 1500 K”, *Journal of Applied Physics* **56**, 314 (1984).
- [113] Corning, *Datasheet CaF*, https://www.corning.com/media/worldwide/csm/documents/Calcium_Fluoride_PI_Sheet_September_2014.pdf.
- [114] Northrop Grumman, *Datasheet undoped YAG*, <http://www.northropgrumman.com/BusinessVentures/SYNOPTICS/Products/SpecialtyCrystals/pages/UndopedYAG.aspx>.
- [115] Ohara, *Datasheet Clearceram-Z*, <http://www.oharacorp.com/pdf/ccz-2013-nav.pdf>.
- [116] Schott, *Datasheet Zerodur*, http://www.schott.com/advanced_optics/german/download/schott_zerodur_katalog_july_2011_en.pdf.
- [117] Diamond Materials, *Thermal properties of CVD Diamond*, http://www.diamond-materials.com/EN/cvd_diamond/thermal_properties.htm.
- [118] N. Bloembergen, “Role of Cracks, Pores, and Absorbing Inclusions on Laser Induced Damage Threshold at Surfaces of Transparent Dielectrics”, *Applied Optics* **12**, 661–664 (1973).
- [119] A. M. Weiner, *Ultrafast optics* (Wiley, Hoboken, N.J, 2009).
- [120] I. B. Angelov, M. von Pechmann, M. K. Trubetskov, F. Krausz, and V. Pervak, “Optical breakdown of multilayer thin-films induced by ultrashort pulses at MHz repetition rates”, *Optics Express* **21**, 31453 (2013).
- [121] J. Steinlechner, I. W. Martin, J. Hough, C. Krüger, S. Rowan, and R. Schnabel, “Thermal noise reduction and absorption optimization via multimaterial coatings”, *Physical Review D* **91** (2015).
- [122] C. Jocher, T. Eidam, S. Hädrich, J. Limpert, and A. Tünnermann, “Sub 25 fs pulses from solid-core nonlinear compression stage at 250 W of average power”, *Optics Letters* **37**, 4407–4410 (2012).
- [123] A. Cingöz, D. C. Yost, T. K. Allison, A. Ruehl, M. E. Fermann, I. Hartl, and J. Ye, “Broadband phase noise suppression in a Yb-fiber frequency comb”, *Optics Letters* **36**, 743–745 (2011).

- [124] K. An, B. A. Sones, C. Fang-Yen, R. R. Dasari, and M. S. Feld, “Optical bistability induced by mirror absorption: measurement of absorption coefficients at the sub-ppm level”, *Optics Letters* **22**, 1433 (1997).
- [125] S. Holzberger, N. Lilienfein, M. Trubetskov, H. Carstens, F. Lücking, V. Pervak, F. Krausz, and I. Pupeza, “Enhancement cavities for zero-offset-frequency pulse trains”, *Optics Letters* **40**, 2165 (2015).
- [126] K. Dupraz, K. Cassou, A. Martens, and F. Zomer, “The ABCD matrix for parabolic reflectors and its application to astigmatism free four-mirror cavities”, *Optics Communications* **353**, 178–183 (2015).
- [127] W. P. Putnam, D. N. Schimpf, G. Abram, and F. X. Kärtner, “Bessel-Gauss beam enhancement cavities for high-intensity applications”, *Optics Express* **20**, 24429–24443 (2012).
- [128] D. N. Schimpf, W. P. Putnam, Grogan, Michael. D. W., S. Ramachandran, and F. X. Kärtner, “Radially polarized Bessel-Gauss beams: decentered Gaussian beam analysis and experimental verification”, *Optics Express* **21**, 18469 (2013).
- [129] M. Lax, W. H. Louisell, and W. B. McKnight, “From Maxwell to paraxial wave optics”, *Physical Review A* **11**, 1365–1370 (1975).
- [130] F. Zomer, V. Soskov, and A. Variola, “On the nonparaxial modes of two-dimensional nearly concentric resonators”, *Applied Optics* **46**, 6859–6866 (2007).
- [131] H. Laabs and A. T. Friberg, “Nonparaxial eigenmodes of stable resonators”, *IEEE Journal of Quantum Electronics* **35**, 198–207 (1999).
- [132] P. Russbueltdt, T. Mans, J. Weitenberg, H. D. Hoffmann, and R. Poprawe, “Compact diode-pumped 1.1 kW Yb:YAG Innoslab femtosecond amplifier”, *Optics Letters* **35**, 4169–4171 (2010).
- [133] J.-P. Negel, A. Voss, M. A. Ahmed, D. Bauer, D. Sutter, A. Killi, and T. Graf, “1.1 kW average output power from a thin-disk multipass amplifier for ultrashort laser pulses”, *Optics Letters* **38**, 5442 (2013).
- [134] J. Y. Vinet, P. Hello, C. N. Man, and A. Brillet, “A high accuracy method for the simulation of non-ideal optical cavities”, *Journal de Physique* **2**, 1287–1303 (1992).
- [135] J. Y. Vinet and P. Hello, “Matrix Simulation of Optical Cavities”, *Journal of Modern Optics* **40**, 1981–1993 (1993).
- [136] J. D. Schmidt, *Numerical simulation of optical wave propagation with examples in MATLAB*, Vol. 199, Press monograph (SPIE, Bellingham, Wash., 2010).
- [137] K.-X. Sun and R. L. Byer, “All-reflective Michelson, Sagnac, and Fabry–Perot interferometers based on grating beam splitters”, *Optics Letters* **23**, 567 (1998).

- [138] T. Clausnitzer, E.-B. Kley, A. Tünnermann, A. Bunkowski, O. Burmeister, K. Danzmann, R. Schnabel, S. Gliech, and A. Duparré, “Ultra low-loss low-efficiency diffraction gratings”, *Optics Express* **13**, 4370 (2005).
- [139] K. D. Moll, R. J. Jones, and J. Ye, “Output coupling methods for cavity-based high-harmonic generation”, *Optics Express* **14**, 8189–8197 (2006).
- [140] O. Pronin, V. Pervak, E. Fill, J. Rauschenberger, F. Krausz, and A. Apolonski, “Ultrabroadband efficient intracavity XUV output coupler”, *Optics express* **19**, 10232–10240 (2011).
- [141] I. Pupeza, E. E. Fill, and F. Krausz, “Low-loss VIS/IR-XUV beam splitter for high-power applications”, *Optics express* **19**, 12108–12118 (2011).
- [142] T. J. Hammond, A. K. Mills, and D. J. Jones, “Near-threshold harmonics from a femtosecond enhancement cavity-based EUV source: effects of multiple quantum pathways on spatial profile and yield”, *Optics Express* **19**, 24871–24883 (2011).
- [143] D. C. Yost, T. R. Schibli, J. Ye, J. L. Tate, J. Hostetter, M. B. Gaarde, and K. J. Schafer, “Vacuum-ultraviolet frequency combs from below-threshold harmonics”, *Nature Physics* **5**, 815–820 (2009).
- [144] C. Benko, T. K. Allison, A. Cingöz, L. Hua, F. Labaye, D. C. Yost, and J. Ye, “Extreme ultraviolet radiation with coherence time greater than 1 s”, *Nature Photonics* **8**, 530–536 (2014).
- [145] A. Ozawa and Y. Kobayashi, “Vuv frequency-comb spectroscopy of atomic xenon”, *Physical Review A* **87**, 022507 (2013).
- [146] A. Ozawa, Z. Zhao, M. Kuwata-Gonokami, and Y. Kobayashi, “High average power coherent vuv generation at 10 MHz repetition frequency by intracavity high harmonic generation”, *Optics express* **23**, 15107–15118 (2015).
- [147] A. Paul, R. A. Bartels, R. Tobey, H. Green, S. Weiman, I. P. Christov, M. M. Murnane, H. C. Kapteyn, and S. Backus, “Quasi-phase-matched generation of coherent extreme-ultraviolet light”, *Nature* **421**, 51–54 (2003).
- [148] B. L. Henke, E. M. Gullikson, and J. C. Davis, “X-Ray Interactions: Photoabsorption, Scattering, Transmission, and Reflection at $E = 50\text{--}30,000$ eV, $Z = 1\text{--}92$ ”, *Atomic Data and Nuclear Data Tables* **54**, 181–342 (1993).
- [149] J. Limpert, F. Stutzki, F. Jansen, H.-J. Otto, T. Eidam, C. Jauregui, and A. Tünnermann, “Yb-doped large-pitch fibres: Effective single-mode operation based on higher-order mode delocalisation”, *Light: Science & Applications* **1**, e8 (2012).
- [150] F. Stutzki, F. Jansen, H.-J. Otto, C. Jauregui, J. Limpert, and A. Tünnermann, “Designing advanced very-large-mode-area fibers for power scaling of fiber-laser systems”, *Optica* **1**, 233 (2014).

- [151] S. Holzberger, “Enhancement cavities for attosecond physics”, PhD thesis (Ludwig-Maximilians-Universität, München, 2015).
- [152] J. Peatross and D. D. Meyerhofer, “Intensity-dependent atomic-phase effects in high-order harmonic generation”, *Physical Review A* **52**, 3976–3987 (1995).
- [153] J. Peatross and D. D. Meyerhofer, “Angular distribution of high-order harmonics emitted from rare gases at low density”, *Physical Review A* **51**, R906–R909 (1995).
- [154] E. Takahashi, V. Tosa, Y. Nabekawa, and K. Midorikawa, “Experimental and theoretical analyses of a correlation between pump-pulse propagation and harmonic yield in a long-interaction medium”, *Physical Review A* **68**, 023808 (2003).
- [155] E. D. Palik, ed., *Handbook of optical constants of solids* (Acad. Press, San Diego, Calif., 1998).
- [156] S. Hädrich, A. Klenke, J. Rothhardt, M. Krebs, A. Hoffmann, O. Pronin, V. Pervak, J. Limpert, and A. Tünnermann, “High photon flux table-top coherent extreme-ultraviolet source”, *Nature Photonics* **8**, 779–783 (2014).
- [157] T. L. S. Collaboration et al., “Advanced LIGO”, *Classical and Quantum Gravity* **32**, 074001 (2015).
- [158] E. Ettl, M. Dierolf, K. Achterhold, C. Jud, B. Günther, E. Braig, B. Gleich, and F. Pfeiffer, “The Munich compact light source: initial performance measures”, *Journal of synchrotron radiation* **23** (2016).
- [159] R. J. Loewen, J. Riffkin, and R. D. Ruth, “X-RAY TRANSMISSIVE OPTICAL MIRROR APPARATUS”, US 7,443,956 B2 (2008).
- [160] S. Hädrich, M. Krebs, A. Hoffmann, A. Klenke, J. Rothhardt, J. Limpert, and A. Tünnermann, “Exploring new avenues in high repetition rate table-top coherent extreme ultraviolet sources”, *Light: Science & Applications* **4**, e320 (2015).
- [161] A. Vernaleken, P. Rußbüldt, T. Sartorius, J. Schulte, and J. Weitenberg, “Verfahren und Anordnung zur spektralen Verbreiterung von Laserpulsen für die nicht-lineare Pulskompression”, 10 2014 007 159.6 (15.05.2014).
- [162] F. Emaury, C. J. Saraceno, B. Debord, D. Ghosh, A. Diebold, F. Gèrôme, T. Südmeyer, F. Benabid, and U. Keller, “Efficient spectral broadening in the 100-W average power regime using gas-filled kagome HC-PCF and pulse compression”, *Optics Letters* **39**, 6843 (2014).
- [163] X. Feng, S. Gilbertson, H. Mashiko, H. Wang, S. D. Khan, M. Chini, Y. Wu, K. Zhao, and Z. Chang, “Generation of Isolated Attosecond Pulses with 20 to 28 Femtosecond Lasers”, *Physical Review Letters* **103** (2009).

-
- [164] P. Tzallas, E. Skantzakis, C. Kalpouzos, E. P. Benis, G. D. Tsakiris, and D. Charalambidis, “Generation of intense continuum extreme-ultraviolet radiation by many-cycle laser fields”, *Nature Physics* **3**, 846–850 (2007).
- [165] M. Gebhardt, C. Gaida, S. Hädrich, F. Stutzki, C. Jauregui, J. Limpert, and A. Tünnermann, “Nonlinear compression of an ultrashort-pulse thulium-based fiber laser to sub-70 fs in Kagome photonic crystal fiber”, *Optics Letters* **40**, 2770 (2015).
- [166] F. Jansen, F. Stutzki, C. Jauregui, J. Limpert, and A. Tünnermann, “High-power very large mode-area thulium-doped fiber laser”, *Optics Letters* **37**, 4546 (2012).

Appendix: Data archiving

The raw data and data analysis are in the data archive of the Laboratory for Attosecond Physics at the Max Planck Institute of Quantum Optics.

Each figure is generated by a Python script, in which all data manipulation on the raw data is performed. Drawing are supplied as SVG files. The naming scheme is `chX_NAME.py`.